Topics in Current Chemistry (2022) 380: 44
https://doi.org/10.1007/s41061-022-00397-3

REVIEW

# Covalent and Non-covalent Functionalized Nanomaterials for Environmental Restoration

**Shizhong Zhang[1] · Sumeet Malik[1,2] · Nisar Ali[1] · Adnan Khan[2] · Muhammad Bilal[3] · Kashif Rasool[4]**

Received: 2 January 2022 / Accepted: 7 June 2022 / Published online: 11 August 2022


## Abstract

Nanotechnology has emerged as an extraordinary and rapidly developing discipline of science. It has remolded the fate of the whole world by providing diverse horizons in different fields. Nanomaterials are appealing because of their incredibly small size and large surface area. Apart from the naturally occurring nanomaterials, synthetic nanomaterials are being prepared on large scales with different sizes and properties. Such nanomaterials are being utilized as an innovative and green approach in multiple fields. To expand the applications and enhance the properties of the nanomaterials, their functionalization and engineering are being performed on a massive scale. The functionalization helps to add to the existing useful properties of the nanomaterials, hence broadening the scope of their utilization. A large class of covalent and non-covalent functionalized nanomaterials (FNMs) including carbons, metal oxides, quantum dots, and composites of these materials with other organic or inorganic materials are being synthesized and used for environmental remediation applications including wastewater treatment. This review summarizes recent advances in the synthesis, reporting techniques, and applications of FNMs in adsorptive and photocatalytic removal of pollutants from wastewater. Future prospects are also examined, along with suggestions for attaining massive benefits in the areas of FNMs.

**Keywords** Contaminants · Photocatalysis · Functionalized nanomaterials · Quantum dots · Carbon nanomaterials · Graphene nanomaterials

✉ Shizhong Zhang
shiz@hyit.edu.cn

✉ Nisar Ali
nisarali@hyit.edu.cn

✉ Kashif Rasool
krasool@hbku.edu.qa

Extended author information available on the last page of the article

## 1 Introduction

Water, which covers 70% of the earth's surface, is a basic necessity for the life of every individual on earth. Nevertheless, extreme ecological contamination jeopardizes human well-being [1, 2]. Environmental contamination has become a major issue in industrialized and developing nations as a consequence of industrialization [3]. Remediation of water, air, and soil contamination is of great concern, especially for developing nations [4]. The fundamental contaminants in water (including surface water, groundwater, and tap water) include heavy metal ions, inorganic compounds (nitrates, chlorides, phosphates, etc.), dyes (synthetic as well as natural), surfactants, pharmaceuticals, pesticides, and numerous other complex compounds [5, 6]. The major sources of heavy metals include industrial effluents, agricultural operations, mining, and metallurgical processes. A prime source of lead release is automobile discharge [7]. Other metals such as copper, zinc, and arsenic [8] are obtained from the smelting process. Burning of fossil fuels is the main source of mercury, tin, and selenium, while the use of pesticides is a source of arsenic production [9].

A crucial category of emerging contaminants is the dyes whose production is also directly related to the industrial processes. The major sectors employing dyes include the textile industries for the coloring of fabrics, staining of biological and biochemical substances, food industries using dyes for enhancing the texture of their food products, cosmetics, leather goods, paint, and pigments [10, 11]. Another breakthrough in the industrial sector is the pharmaceutical industry production of an enormous stock of medicines for various conditions [12]. However, in contrast to the health benefits obtained through the production of such medicines, the disposal of various antibiotics into the environment is putting the lives of humans at risk. Additionally, expired medicines are also disposed of, which is causing contamination and ill effects [13]. The same logic applies to the use of pesticides and surfactants, which, once used to the degree of demand, are left unchecked in the environment, causing toxic effects. The different types of pesticides, herbicides, and insecticides sprayed on crops for better yields typically do not completely vanish, thus making their way to the food chain and causing detrimental health issues [14–16]. These pollutants have recently been categorized as emerging contaminants that can cause devastating ecological effects directly influencing human health [17]. Humans are the primary targets for such contaminants, directly by water consumption or indirectly through the food chain. The environmental deterioration caused by such toxic contaminants ultimately causes health-related issues for individuals. These contaminants are known to be carcinogenic and mutagenic substances in most cases [18].

Heavy metal pollutants are very harmful. For example, cadmium, which is a human carcinogen, causes destructive effects on the lungs, possible kidney diseases, and bone fragility [19, 20]. Chromium in the form of chromium(III) is an essential nutrient, while chromium (VI) is highly toxic. The common health-related issues associated with chromium include asthma, cough, shortness of breath, or wheezing [21]. Lead has proved to be the cause of various ailments

including damage to brain and kidney cells ultimately leading to death [22]. Another harmful metal is mercury which may permanently damage critical body organs. This causes malfunctioning of the brain, resulting in irritability, behavioral changes, tremors, and reduced vision or hearing [23, 24].

Dyes are another form of toxic contaminants causing harmful effects due to their excessive usage. The toxicity of the dye is associated with the azo group present in its structure, making it a complex system. The azo group is defined as possessing a central nitrogen–nitrogen double bond and is hence electron-deficient [25]. The presence of such azoic dyes in wastewater is highly visible, affecting the transparency of water and causing aesthetic disadvantages. The more important aspect of the presence of such compounds in wastewater is their harmful effects on human health, causing several disorders including allergies, cramps, kidney failure, liver damage, and genetic mutations [26, 27]. Pharmaceuticals come under the category of biologically active compounds that have been developed for disease control in living organisms [28].

Apart from the beneficial effects of these pharmaceutical compounds, their biological activity may also affect non-target organisms in adverse ways, thereby harming the ecosystem function and associated ecosystem services. Also, unsupervised disposal of unused or expired pharmaceuticals into the environment may have serious health effects. The most common health-related issues caused by pharmaceutical contaminants include hormonal disruptions, infertility, and colorectal tumors [29–32].

Other contaminants include phosphates and nitrates, which also have serious health and environmental impacts. Although nitrate itself is nontoxic, its conversion into nitrite causes a condition called methemoglobinemia by interfering with the ability of hemoglobin to take up $O_2$, which causes cancers of the digestive tract [33–35]. The environmental effects of phosphates and nitrates in wastewater contribute to the phenomenon of eutrophication, leading to harmful algal blooms [36–38]. These issues demand the development of safety measures against these harmful contaminants. Thus, the need for contaminant removal has become critical. Researchers have been focusing on developing such strategies for the removal of toxic contaminants with minimal labor and cost while achieving effective results.

Different techniques applied to abolish pollutants in water bodies include ion-exchange [39], reverse osmosis [40], chemical precipitation [41], membrane filtration [42], coagulation and flocculation [43], irradiation [44], electrochemical treatment techniques [45], and advanced oxidation processes [46, 47]. These strategies are being exploited extensively in the context of toxic contaminant removal against wastewater bodies, but their activity is limited for one reason or another. The applications of these strategies may be affected by numerous factors, for example, handling productivity, operational strategy, vitality necessities, and monetary advantage [48–54]. The quest for the development of such a technique offering better removal of contaminants has turned the attention of researchers towards sorptive and photocatalytic techniques. Both sorption [55] and photocatalytic techniques [56–58] have enabled the complete removal of contaminants, and many studies in the literature confirm the contaminant removal efficiency of these techniques (Scheme 1).

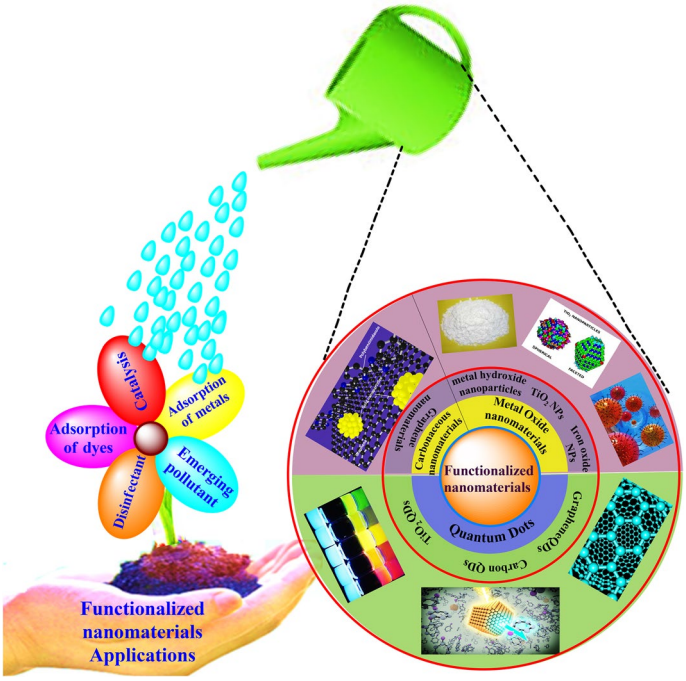


**Scheme 1** Possible applications of covalent/non-covalent functionalized nanomaterials

The classical materials which have been used to date for the sorption and photocatalysis of contaminants are now being replaced by nanomaterials (NMs) due to their innovative and efficient approach. The review presented herein compiles the most recent and innovative utilization of functionalized nanomaterials (FNMs) in environmental remediation, highlighting the importance of FNMs in the present era.

## 2 Functionalized Nanomaterials, an Innovative Approach Towards Environment Remediation

Recent advancements in nanotechnology have provided good alternatives for upgrading wastewater treatment processes. The robustness of nanoscience has taken over the globe due to its remarkable features relying mainly upon the particle size and surface-to-volume ratios [59]. NMs, which feature nanoscale dimensions (less than 100 nm), have garnered considerable attention because of their extraordinary magnetic, synergist, and electronic properties [60, 61]. Because of these unique properties, many efforts have focused on the potential use of NMs for environmental remediation [62]. In this way, NMs have revolutionized the environmental remediation and sensing fields, offering better efficiency in wastewater contamination. Figure 1 outlines some of the well-known FNMs.

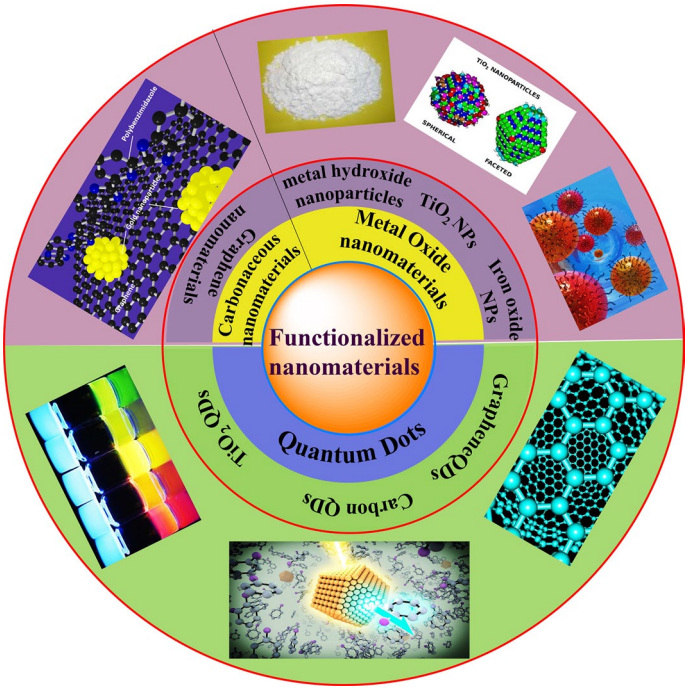


**Fig. 1** Covalent/non-covalent functionalized nanomaterials

NMs of different shapes/morphology—for example, nanoparticles [63], nanotubes [64], nanowires [65], and nanofibers [66]—provide a choice for environmental restoration mainly through the removal of toxic contaminants [67]. NMs play a huge role in contaminant removal due to the high surface area (surface-to-volume ratio) and related high reactivity [68, 69]. As NMs additionally offer extraordinary dependability, effectiveness, and size-dependent optical features, their utility in multiple fields, including sensing, [70], drug delivery frameworks [71], catalysis [72], gas/energy storage [73], and sorption [74–77], is huge (Fig. 2). As a result, NMs have proved to be an important aspect of environmental remediation strategies.

Many NMs have been utilized in the context of contaminant removal from wastewater bodies. In some instances, the activity of the NMs may be inhibited due to various factors including their insolubility in physiological buffers, instability, and low efficiency, recovery, and recyclability [78, 79]. These issues can be resolved through functionalization of NM van der Waals forces, π–π stacking, charge transfer, and/or hydrophobic interactions of the NMs with functionalizing agents [80]. Important advantages associated with the functionalization of NMs include corrosion control, molecular electronic junctions, and complexing layers for the removal of contaminants [81]. Hence, FNMs have proved to be an excellent choice for contaminant removal based on their properties. The most common limitation of NMs is their strong van der Waals forces; they tend to aggregate, thereby reducing the surface availability for better functioning.

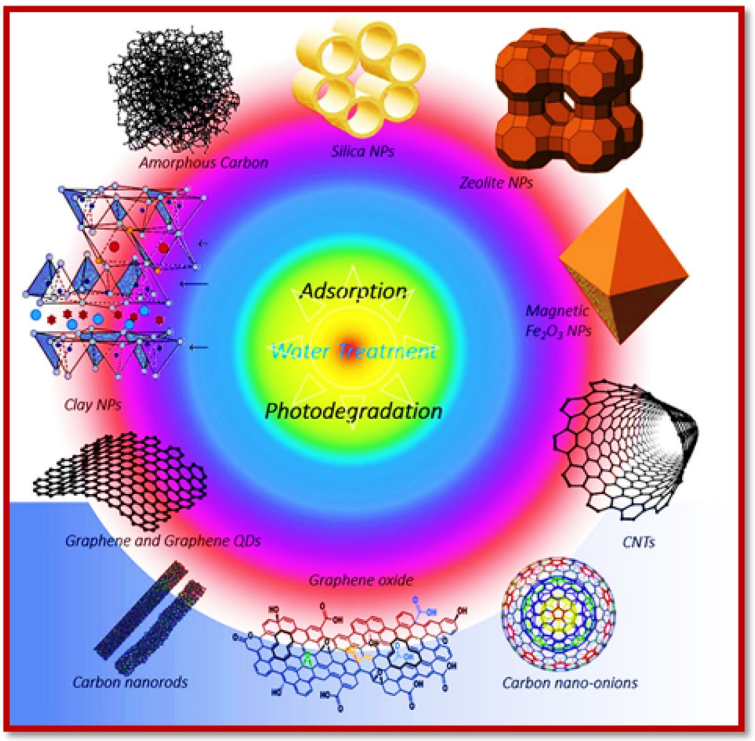


**Fig. 2** Illustration of photodegradation and adsorption process for wastewater treatment. Reproduced with permission [74] Copyright 2020, Elsevier

Also, the recovery of inorganic NMs is a difficult task that limits the usage and recyclability of the sorbents or photocatalysts [82]. Stability and high porosity are important factors that need to be considered to improve efficiency. To meet the stated standards and achieve better dispersion of NMs, they are often further functionalized to improve their activity. Fabrication or functionalization offers additional sites for the removal of contaminants, thereby enhancing their efficiency. Functionalization of NMs improves their coupling ability towards the analyte, hence enhancing their activity as sorbents or photocatalysts. Such advancement is ideal for the removal of contamination at an ultra-efficient and robust level [83, 84]. Furthermore, functionalized fluorescent NMs tend to have utility for various applications because of their permeability, huge surface area, high stacking limit, and explicit association against toxins such as lead (Pb), cadmium (Cd), copper (Cu), and mercury (Hg) [85]. Also, functionalization of NMs may significantly strengthen them in aqueous solutions by wrapping them superficially with stabilizing agents, for example, biomolecules, surfactants (cationic/anionic), or natural particles [86, 87].

Functionalized magnetic NMs, comprising both natural and inorganic components, have recently been recognized as highly promising agents for different

applications, specifically for serving as sorbents or photocatalysts for the removal of contaminants from wastewater bodies. Due to their superparamagnetic properties, huge explicit surface area, and specific sorption limit, this exceptional class of NMs displays a phenomenal capacity for separating and enhancing various analytes of interest [88].

Previously, smaller molecules were used for the functionalization of the NMs, which have now been replaced by large polymeric and biopolymeric molecules [89]. The most commonly utilized techniques for polymer and biopolymer functionalization of NMs include the "grafting-to" and "grafting-from" approaches [90] (Fig. 3). The grafting-from approach allows high-molecular-weight chains of the polymers to be grafted onto the surface of the NMs, minimizing the chances of steric hindrance and resulting in higher-molecular-weight polymer-functionalized NMs. The whole process is completed in three steps: first, the suitable functional group approaches the material, then a covalent interaction is created with the initiator element, and finally the grafting of the polymer onto the surface of the NMs occurs through any of the available techniques.

The techniques used for polymerization onto the NM surface through grafting-from polymerization include atom transfer radical polymerization (ATRP) [91, 92], reversible addition-fragmentation chain-transfer polymerization (RAFT) [93, 94], plasma and UV/$O_3$ (UVO)-induced grafting [95, 96], distillation–precipitation–polymerization (DPP) [97, 98], and surface-initiated polymerization (SIP) [99, 100] (Fig. 4). The second concept is the grafting-to approach, which works contrary to the grafting-from approach. According to this, the polymer chains are manufactured first before their linkage to the functional groups of the NMs through amidation, esterification, click chemistry, etc. The grafting-from approach is more frequently used than the grafting onto approach. The most commonly used techniques based on the grafting-to notion include molecular bottle-brush modification [101], Piers–Rubinsztajn (PR) reaction [102], atom transfer radical addition (ATRA) [103], and radical addition. The common feature in these techniques is that they

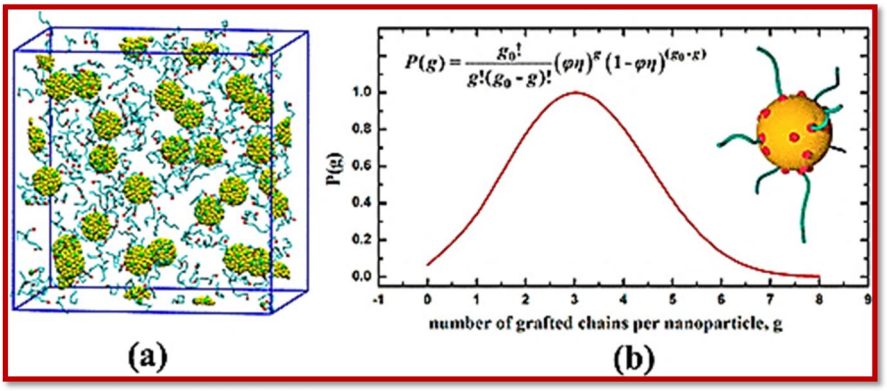


**Fig. 3** Illustration of the grafting-to reaction. Reproduced with permission [90] Copyright 2018, American Chemical Society

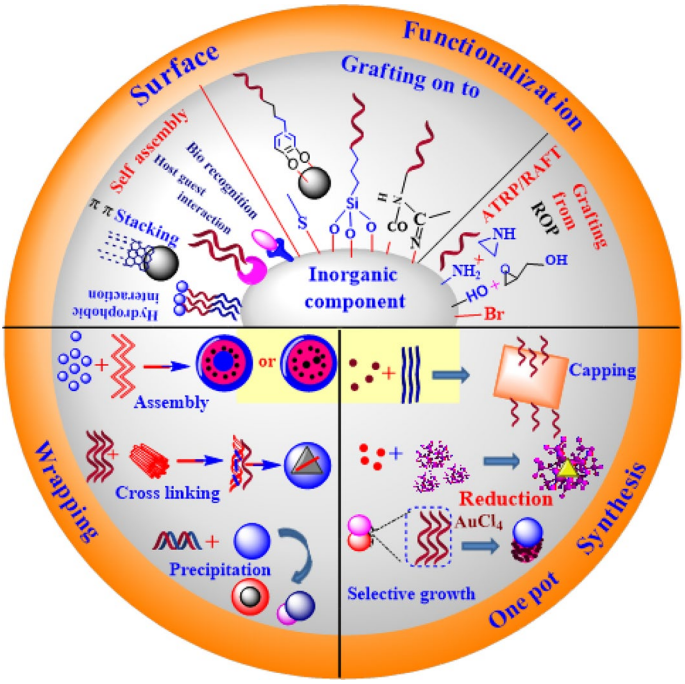


**Fig. 4** Different techniques used for the synthesis and functionalization of nanomaterials

incorporate the polymeric chains with the NMs, introducing additional functionalities inside the NMs, eventually increasing their activity, stability, and efficiency for environmental restoration.

## 3 Trends in the Techniques for the Removal of Contaminants

The functioning of FNMs involves certain pathways depending upon their applications. The NMs that are specifically used for environmental remediation purposes also follow a certain route to remove contaminants. A variety of procedures have been reported to date that make use of the FNMs, but two of these procedures have been highly exploited due to their greater simplicity and efficiency. These methods involve the sorption [104] or photocatalytic [105, 106] pathway for the removal of contaminants. This review will cover the importance of FNMs in environmental restoration with regard to the sorptive and photocatalytic mechanisms.

### 3.1 Sorptive Removal of Contaminants

Sorption is preferred over other methods of contaminant removal based on its comparatively straightforward operation, cost-effectiveness, and energy-efficiency. [107]. The constituency of the sorbent material is the prime factor for

determining the capacity of the sorption process. Sorption as a common practice for the removal of contaminants, has been widely exploited due to its useful features, particularly its cost-effectiveness, coherence, and feasibility [108]. Because of its one-step process, it can be considered as a simple and facile strategy. The lower costs of the sorption process have made it an appealing choice in underdeveloped and developing countries. Sorption has emerged as a versatile technique for the removal of contaminants and is being widely studied by researchers [109]. Sorption has become a successful one-unit operation for the treatment of industrial waste in recent years (Fig. 5). Although sorption is a commonly utilized technique for the removal of contaminants, its novelty depends on the type of materials used as sorbent. A variety of materials have been introduced that can be used as sorbents at multiple scales [110]. These materials include naturally occurring substances as well as synthetic materials [111].

These materials include low-cost recycled materials such as fruit extracts [112], coconut shells [113], scrap tires [114], fly ash [115–117], sawdust [118], peat moss [119], rice husk [120], red mud [121, 122], minerals [123], blast furnace slag [124] and sludge [125], black liquor lignin [126], waste slurry [127], chitin [128], chitosan [129], and alginate [130]. The synthetic materials used as sorbents include activated carbon [131], zeolites [132], metal oxides/hydroxides [133], metal sulfides [134], and metal selenides [135]. Figure 6 shows some biochar and mineral-derived NMs for effective wastewater treatment.

FNMs have recently proved to be a productive choice for the removal of contaminants. The use of FNMs as sorbents offers more novelty, high efficiency, and simplicity, which increases the interest of researchers in this discipline. A variety of reports are available that use FNMs as sorbents for the removal of contaminants, including thiol-functionalized magnetite nanoparticles [136], carboxyl- and amine-functionalized nanoparticles [137], polyrhodanine-functionalized aluminum oxide [138], $TiO_2$ fabricated on mesoporous MCM-4 [139], silica-functionalized magnetic nanoparticles [140], and polymer-functionalized magnetic nanoparticles [141].


**Fig. 5** Explanation of the sorption process on a fixed bed for effective removal of pharmaceutical contaminants. Reproduced with permission [109], Copyright 2018, Elsevier

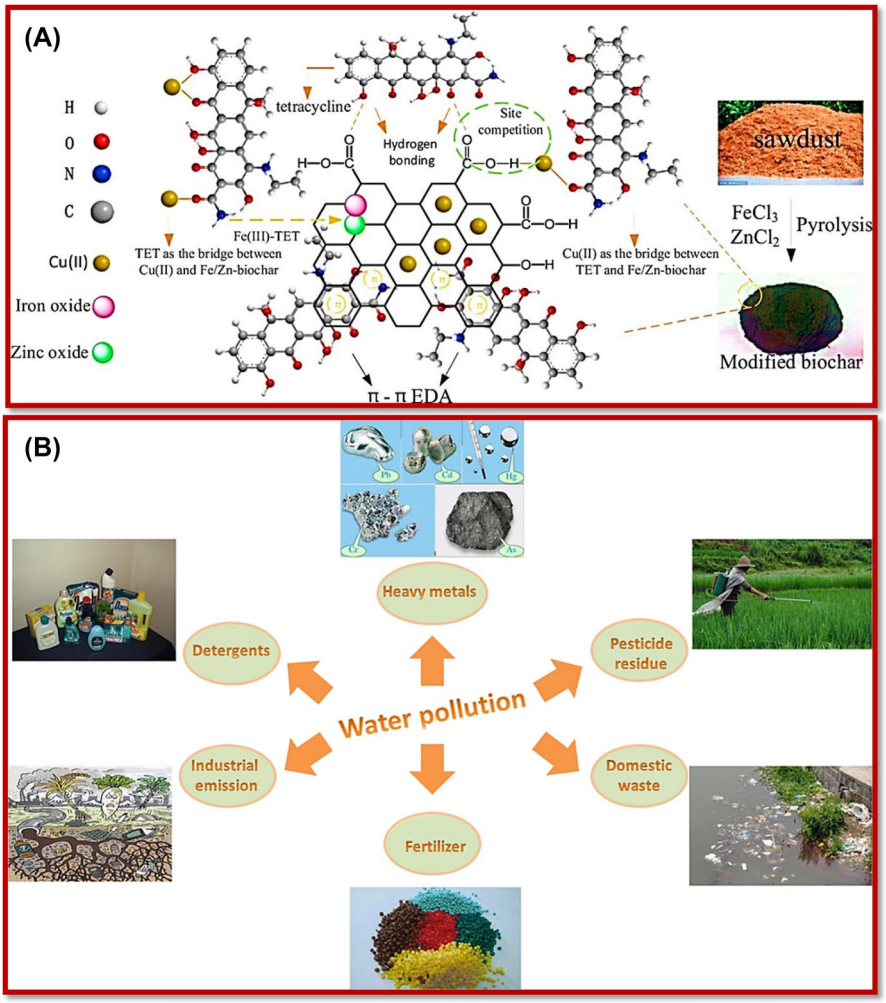


**Fig. 6** **a** Sawdust-derived biochar and its applications for the removal of copper and tetracycline [118], and **b** explanation of mineral materials for removal of water pollutants released from different sectors. Reproduced with permission [123], Copyright 2017, International Water Association

### 3.2 Photocatalytic Removal of Contaminants

Another strategy for the removal of contaminants using FNMs is photocatalysis [142]. A photocatalyst works on the principle of absorbing energy and producing a photon by activation and acceleration of the chemical reaction without undergoing denaturation itself. The photocatalytic phenomenon has been frequently employed by researchers for its useful properties including its efficiency, advanced equipment, and highly efficacious follow-up [143]. The photocatalytic process normally requires an energy source for its initiation, mainly sunlight irradiation. As sunlight

is a natural and abundant source of energy, it reduces the energy-related costs for the process. In some instances, UV light is used instead of sunlight as an energy source depending upon the range of the contaminants being studied.

The notion of photocatalysis is to utilize a semiconductor material with a dually functional surface that can act as both cathode and anode performing the activity of a photochemical cell, applicable in various domains including photodegradation [144], photocatalytic $CO_2$ reduction [49, 50, 145], photocatalytic synthesis [146], photocatalytic gas-phase oxidation [147], and photocatalytic removal of contaminants [148]. Each of these fields utilizes the concept of photocatalysis at its best. The idea of photocatalysis in the field of contaminant removal eventually leading to the restoration of the environment is growing by leaps and bounds, offering a much broader horizon for its usage [149]. In the case of photocatalysis, the prime factor for choosing the photocatalytic material (photocatalyst) is its semiconductor nature. A semiconductor photocatalyst possesses necessary properties including excellent energy position and bandgap, lower probability of electron–hole recombination, and non-toxicity. The most commonly used materials for photocatalytic purposes include metal oxides [150–152], metal sulfides [153, 154], $Fe_2O_3$ [155], $SnO_2$ [156], $WO_3$ [157], metal selenides [158], CuO [159], and $Nb_2O_5$ [160].

The advantages of the properties of FNMs have been used in the fabrication of photocatalysts [161]. Several FNMs are available which have been used as potent photocatalysts for the removal of contaminants including azole-functionalized $TiO_2$ [162, 163], Ag-modified metal oxide [164], carboxyl-functionalized metal sulfides [165, 166], and sodium-functionalized quantum dots [167, 168].

## 4 Functionalized Carbon Nanomaterials Robustness in Contaminant Removal

When considering a variety of NMs, carbon-based NMs cannot be overlooked, for they are considered as next-generation materials in multifarious fields [169]. Among the fields utilizing carbon NMs biosensors, drug delivery, biomedical applications, superconductors, and electrically conductive materials are worth mentioning. Because of the useful properties of carbon NMs, for instance, high electrical conductivity and well-defined thermal and mechanical properties, they are used extensively in wastewater treatment [170]. They have proved to be excellent sorbents and photocatalysts on account of their higher surface-to-volume ratio, uniform pore distribution, and highly porous structure. However, despite the very useful properties associated with carbon NMs, their application is sometimes constrained by certain limitations. Carbon NMs have the tendency to agglomerate when they come in contact with the solvent system, which is attributed to their weak van der Waals forces and lower solubility. During synthesis of carbon NMs, some impurities are also formed which may hinder the activity of carbon-based sorbent or photocatalysts. Hence, functionalization of carbon NMs is performed to strengthen their properties and enhance their activity. The functionalized carbon NMs are available in many forms, including carbon nanotubes (CNTs), graphene and its derivatives, and fullerenes. [171].

### 4.1 Carbon Nanotubes (CNTs)

Carbon nanotubes (CNTs) are the most commonly used form of carbon NMs, and can be pictured as graphene sheets rolled up as tubular cylinders having nanoscale diameters. CNTs are further categorized as single-walled CNTs (SWCNTs), and multi-walled CNTs (MWCNTs). The SWCNTs consist of a single layer of graphene sheet rolled to form a single cylinder, while the MWCNTs consist of multiple graphene sheets arranged as concentric cylindrical sheets [172]. Various methods are available for the synthesis of CNTs including laser ablation, discharge, and chemical vapor deposition. Because of their unique physicochemical properties and structural features, CNTs have been utilized extensively as sorbents and photocatalysts for the removal of various contaminants [173]. The activity of the CNTs can be further enhanced by functionalization with other groups, enhancing their properties such as porosity, hydrophilicity, solubility, and mechanical strength. Alkahlawy et al. [174] performed the photocatalytic degradation of Congo red (CR) dye utilizing MWCNTs modified with zinc oxide and copper oxide nanoparticles. The Zn/CNT photocatalyst possessed excellent activity towards the degradation of CR dye, with degradation efficiency of 97.7% in 70 min under visible light irradiation. The studies showed that the photocatalytic efficiency of Zn/CNTs is directly related to the high dislocation density ($\delta$) value of 55.4. This value represents the number of vacancies and defects present in the crystal lattice. The lattice deficiency is the result of the route of synthesis. These intrinsic point defects present in the lattice as atomic impurities, vacancies, and interstices can be detected in doping materials. These defects may function as holes when exposed to active centers, which confirms the dependence of photocatalytic efficiency on the chemical structure rather than texture. The study of the mechanism of photocatalytic activity showed that in a surface defect state, holes/electrons can be trapped, preventing recombination and increasing the oxidation–reduction rate. Structural analysis showed that a number of surface defects were found in the ZnO/CNT sample [175]. These defects mainly consisted of bandgap acceptor states which trap the holes, preventing recombination. Hence, the increased photocatalytic efficiency of the prepared photocatalyst was attributable to the large number of acceptor states caused by the ZnO defects. In addition to the expansion of the light absorption edge of visible light, the acceptor states also cause a delay in the recombination of electron–hole pairs. Hence, the highly defined photocatalytic efficiency can be attributed to the presence of a large number of defects and acceptor states. The ZnO defects act as electron acceptors or hole donors, promoting the position of carrier charges and thus prolonging the separation via trapping at energy levels closer to the conduction band (CB) or valence band (VB), respectively [176]. The photogenerated electrons ($e_{CB}^-$) may also interact with the electron acceptors, such as oxygen sorbed on the surface of the nanocomposite or dissolved in water, forming radical anions ($O_2^-$ superoxide). The photogenerated holes will also react to form hydroxyl radicals. As result, the highly reactive species produced, $OH^{\cdot}$, $HO_2^{\cdot}$, and $O_2^{\cdot}$, will eventually cause the degradation of CR dye. Li et al. [177] explored the sorption ability of functionalized MWCNTs (f-MWCNTs) using crystal violet (CV) and rhodamine B (RB) dye. The sorption of each dye was performed individually and then in a binary system. Individually, the sorption

capacity of f-MWCNT for the CR was in the range of 0.57–0.86 mmol/g, while the sorption capacity of RB was 0.75–0.88 mmol/g. The study of individual sorption capacity was related to the physical interaction forces between the f-MWCNT and the dye molecules irrespective of the size, thus resulting in almost equal sorption capacity for both. The mechanistic studies focused on the sorption of both dyes due to the interaction with hydrogen, thus forming associations with COOH or C–H groups of the sorbent molecule [178]. But in the case of a binary system, the sorption capacity of CV was 0.90–1.64 mmol/g, while the sorption capacity for RB was 0.51–0.84 mmol/g. The results clearly showed increased (almost double) sorption of the CV dye, while the sorption of RB was decreased. This trend in sorption capacity in a binary system for both dyes was explained based on synergistic and antagonistic sorption mechanisms. The sorption models applied to the sorption of both dyes in a binary system indicated that the sorption of CV was enhanced in the presence of RB dye, while the opposite was the case for RB dye in the presence of CV dye. The sorption energy also directly affected the sorption process, which seemed to increase in the binary system, hence causing an increase in CV sorption Fig. 7 shows the adsorption of methylene blue (MB) dye on vitamin C-MWCNT nanocomposites.

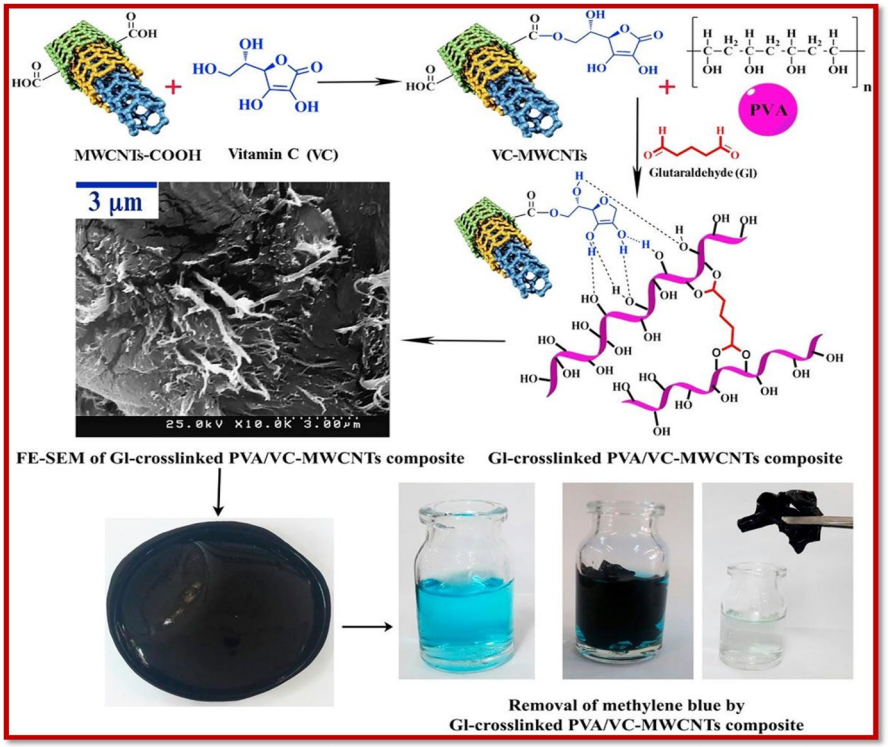


**Fig. 7** Preparation of vitamin C-MWCNT nanocomposites and their digital pictures and their application for MB dye adsorption. Reproduced with permission [178], Copyright 2019, Elsevier

Shao et al. [179] performed decontamination of polychlorinated biphenyls (PCBs) in aqueous solutions on the surface of MWCNTs grafted with β-cyclodextrin (β-CD) through a plasma technique to enhance the chemical functionality. The maximum sorption capacity achieved by MWCNT-g-CD for 4,4′-DCB (4,4′-dichlorobiphenyl) and 2,3,3′-TCB (2,3,3′-trichlorobiphenyl) was 261 mg/g and 235 mg/g, respectively. A comparison of the sorption capacity of the MWCNTs and MWCNT-g-CD was also performed to evaluate 4,4′-DCB (4,4′-dichlorobiphenyl) and 2,3,3′-TCB (2,3,3′-trichlorobiphenyl) sorption efficiency, and a greater percentage was sorbed by the grafted MWCNT-g-CD than the non-FNMs. This higher sorption capacity possessed by the MWCNT-g-CD depends on the van der Waals and hydrophobic interactions of the sorbates with the surface of the MWCNT-g-CD. The sorption process is a surface phenomenon and is related to the surface sites available for the sorbate molecules [180]. The interstitial surface and grooves of the sorbent molecule may not be available for the sorption process. The plasma grafting of MWCNTs with β-cyclodextrin provided complex formation with the 4,4′-DCB and 2,3,3′-TCB, which enabled the entrance of the sorbate molecules inside the inclusions of the MWCNT-g-CD, thus enhancing the sorption process.

The functionalized CNTs used for the sorption and photocatalysis of contaminants are shown in Table 1.

### 4.2 Graphene and Its Derivatives

As an important topic in any in-depth discussion of carbon-based NMs, graphene is considered to be the simplest form of carbon and is also the thinnest material known. Graphene is unquestionably an extraordinary material that has been used extensively in various fields [239]. The structural assay of graphene shows that it consists of a two-dimensional single-layer sheet of carbon atoms that are arranged into an $sp^2$-bonded honeycomb-like lattice structure. The properties associated with graphene, including thermal stability, larger surface area, mechanical strength, electrical conductivity, and flexibility, make it a highly promising candidates for use in wastewater treatment processes [240, 241]. The specific properties of high surface area, delocalized π-electron system, and abundantly present active sites indicates excellent sorption capacity inhibited by the graphene-based NMs. Not only has pristine graphene been used massively in the removal of contaminants, but the derivatives of graphene have also been utilized [242]. Many reports are available on the utilization of graphene oxide, reduced graphene oxide, graphene platelets, and graphene-based composites as potent sorbents as well as photocatalysts. The properties of graphene NMs can be further enhanced by performing the functionalization procedure through groups such as thiol moieties or carboxylic groups [243].

Zamani and Salem [244] studied the photocatalytic behavior of graphene oxide sheets coupled with carbon nanotubes. In the first step, functionalization of carbon nanotubes was performed using acid reflux conditions, and they were then coupled with graphene oxide and decorated with anatase using the sol–gel method [245]. The obtained nanocomposite showed 96.5% efficiency for the degradation of MB dye. The hybrid nanocomposite facilitated the degradation of the contaminants

**Table 1** Carbonaceous nanomaterials in wastewater remediation

| Nanomaterial | Contaminant | Mechanism | Sorption/catalytic capacity | Studied conditions | | | Cycles | References |
|---|---|---|---|---|---|---|---|---|
| | | | | pH | Time | Temp °C | | |
| (MWCNT) | $Co^{2+}$ | Sorption | 78.94 mg/g | 10 | 38.6 | | | [181] |
| γ-alumina | | | 75.78 mg/g | 10 | 35.5 | | | |
| (MWCNT) | Cr(III) | Sorption | 8.4 mg/g | | 30 | 20 | | [182] |
| Magnetic tubular carbon nanofibers (MTCFs) | $Cu^{2+}$ | Sorption | 375.93 mg/g | 6 | 10 | 25 | 6 | [183] |
| Lanthanum hydroxide-oxidized multi-walled carbon nanotubes ($La(OH)_3$-OxM-WCNTs) | p-Nitrophenol | Electrochemical determination | 95.62–110.75% | 7 | | | | [184] |
| Sulfur-coated magnetic multi-walled carbon nanotubes (S-M-MWCNTs) | Hg(II) | Sorption | >90% | 4–8 | 180 | | 8 | [185] |
| Carbon nanotubes grafted with polyethylene glycol (CNT/PEG) | Phenol | Sorption | 21.23 mg/g | 6 | 30 | 25 | | [186] |
| Magnetic multi-walled carbon nanotubes modified with polyaluminum chloride (M-PAC-MWCNTs) | Humic acid | Sorption | 98.57% | 7 | 30 | 25 | | [187] |
| Linear β-cyclodextrin-functionalized multi-walled carbon nanotubes (MWCNTs-CDP) | U(VI) | Sorption | 89.54 mg/g | 6 | 180 | 70 | | [188] |
| Amine-modified magnetic, multi-walled carbon nanotubes | Bisphenol-A | Sorption | 43.48 mg/g | 12 | 45 | 30 | 5 | [189] |

**Table 1** (continued)

| Nanomaterial | Contaminant | Mechanism | Sorption/catalytic capacity | Studied conditions | | | Cycles | References |
|---|---|---|---|---|---|---|---|---|
| | | | | pH | Time | Temp °C | | |
| Fungal mycelium coupled with carbon nanotubes (FM-CNTs) | $Cu^{2+}$ | Sorption | 342.22 mg/g | 5 | | | | [190] |
| Barium chromate and multi-walled carbon nanotubes composite MWCNT/$BaCrO_4$) | Evans blue | Photocatalytic degradation | | 8 | | | 4 | [191] |
| Oxidized multi-walled carbon nanotubes (MWCNTs) | Se(VI) | Sorption | 1.865 mg/g | 7 | | 30 | | [192] |
| Multi-walled carbon nanotubes (MWCNTs) | Cu(II) | Sorption | $3.19\times10^{-5}$ mol/g | 5 | | 30 | | [193] |
| Activated carbon | | | $2.31\times10^{-4}$ mol/g | | | | | |
| Graphene oxide | | | $1.18\times10^{-3}$mol/g | | | | | |
| Multi-walled carbon nanotubes (MWCNTs) | Direct blue 53 | Sorption | 409.4 mg/g | 2 | 240 | 50 | 5 | [194] |
| Powdered activated carbon (PAC) | | | 135.2 mg/g | | | | | |
| Functionalized multi-walled carbon nanotubes (f-MWCNTs) | Direct Congo red | Sorption | 148 mg/g | 3 | 120 | | | [195] |
| | Reactive green HE4BD | | 152 mg/g | 5 | | | | |
| | Golden yellow MR | | 141 mg/g | 7 | | | | |
| Multi-walled carbon nanotubes (MWCNTs) | Humic acid | Sorption | 31.37 mg/g | 4 | 180 | | | [196] |
| Nitrogen-functionalized multi-walled carbon nanotubes (MWCNT-ttpy) | $Pb^{2+}$ | Sorption | 36.23 mg/g | 4.5 | 1440 | 20 | | [197] |
| | $Zn^{2+}$ | | 32.60 mg/g | 5.5 | | | | |

**Table 1** (continued)

| Nanomaterial | Contaminant | Mechanism | Sorption/catalytic capacity | Studied conditions | | | Cycles | References |
|---|---|---|---|---|---|---|---|---|
| | | | | pH | Time | Temp °C | | |
| Multi-walled carbon nanotubes/iron oxide composites (MIO–CNTs) | As(V) | Sorption | 47.41 mg/g | 8 | | 25 | | [198] |
| | As(III) | | 24.05 mg/g | | | | | |
| Multi-walled carbon nanotube/graphene oxide composite combined with polyaniline and doped with para toluene sulfonic acid (*p*-TSA-Pani@GO-CNT) | Cr(IV) | Sorption | 142.8 mg/g | 2 | | 30 | | [199] |
| | Congo red | | 66.66 mg/g | 5 | | | | |
| Nitric acid-modified carbon nanotubes (MCNT-$HNO_3$) | Cd(II) | Sorption | 26.88 mg/g | 5.6 | 300 | | | [200] |
| Zero-valent iron nanoparticles immobilized on multi-walled carbon nanotubes (nZVI/MWCNTs) | Direct red 23 | Sorption | 100% | 4 | 10 | 40 | | [201] |
| Magnetic oxidized multi-walled carbon nanotubes | Rhodamine B | Sorption | 33.42 mg/g | 6 | 120 | 25 | 5 | [202] |
| Single-walled carbon nanotubes (SWCNTs) | Reactive blue 4 | Sorption | 567.7 mg/g | 2 | 240 | 25 | | [203] |
| Multi-walled carbon nanotubes (MWCNTs) | | | 502.5 mg/g | | | | | |
| B-cyclodextrin grafted multi-walled carbon nanotube/iron oxide (CD/MWCNT/iron oxide) | Zn(II) | Sorption | 44.43 mg/g | 6.5 | 360 | 70 | 6 | [204] |
| Multi-walled carbon nanotubes (MWCNTs) | Triclosan | Sorption | 166.8 mg/g | 3 | | 15 | | [205] |

**Table 1** (continued)

| Nanomaterial | Contaminant | Mechanism | Sorption/catalytic capacity | Studied conditions | | | Cycles | References |
|---|---|---|---|---|---|---|---|---|
| | | | | pH | Time | Temp °C | | |
| Modified magnetic multi-walled carbon nanotubes (MMWCNTs) | $Pb^{2+}$ | Sorption | 67.25 mg/g | 5 | | 25 | | [206] |
| | $Zn^{2+}$ | | 3.75 mg/g | | | | | |
| Magnesium oxide anchored carbon nanotubes | Sulfadiazine | Photocatalytic degradation | 45 mg/L | 11 | 180 | | 6 | [207] |
| Magnetic carbon nanotube (M-CNT) | Direct red 23 | Photocatalytic degradation | 100% | | 60 | 25 | | [208] |
| | Direct red 31 | | | | | | | |
| | Direct Red 81 | | | | | | | |
| Magnetic multi-walled carbon nanotubes/cerium dioxide nanocomposite (MMWCNTs-$CeO_2$) | Methylene blue | Photocatalytic degradation | 97.5% | | | | 5 | [209] |
| Palladium nanocubes supported multi-walled carbon nanotubes (MWCNTs/Pd) | Methyl orange | Photocatalytic degradation | 99% | | 8 | | | [210] |
| Multi-walled carbon nanotube (MWCNT) | Acid red 14 | Photocatalytic degradation | Up to 100% | 3 | 60 | 25 | | [211] |
| | Acid red 18 | | | | | | | |
| Single-walled carbon nanotubes (SWCNTs) | Basic red 46 | Sorption | 38.35 mg/g | 9 | 80 | 25 | | [212] |
| Carboxylate-functionalized SWCNTs (SWCNT-COOH) | | | 49.45 mg/g | | | | | |
| Graphene | | | 30.52 mg/g | | 90 | | | |
| Graphene oxide | | | 55.57 mg/g | | | | | |
| Multi-walled carbon nanotubes | Alizarin red S | Sorption | 161.2 mg/g | 1 | 30 | 30 | | [213] |
| | Morin | | 26.2 mg/g | | | | | |

**Table 1** (continued)

| Nanomaterial | Contaminant | Mechanism | Sorption/catalytic capacity | Studied conditions | | | Cycles | References |
|---|---|---|---|---|---|---|---|---|
| | | | | pH | Time | Temp °C | | |
| Acid-oxidized multi-walled carbon nanotubes (CNTs) | Mn(VII) | Sorption | 100% | | 240 | | | [214] |
| | Cr(VI) | | | | 180 | | | |
| | Azo dyes (toluidine blue, methylene blue, methyl green and bromopyrogallol red) | | | | 5 | | | |
| Multi-walled carbon nanotubes (MWCNTs) | Eriochrome cyanine R | Sorption | 95.2 mg/g | 2 | 10 | 25 | | [215] |
| Activated carbon (AC) | | | 40.6 mg/g | 3 | 41 | | | |
| Multi-walled carbon nanotubes (MWCNTs) | Arsenazo III | Sorption | 30.58 mg/g | 1 | 15 | 25 | | [216] |
| Activated carbon (AC) | Arsenazo III | | 10.2 mg/g | 1 | 50 | | | |
| | Methyl red | | 46.29 mg/g | 7 | 15 | | | |
| Multi-walled carbon nanotubes (MWCNTs) | Reactive red M-2BE | Sorption | 335.7 mg/g | 2 | | 25 | 4 | [217] |
| Powdered activated carbon (PAC) | | | 260.7 mg/g | | | | | |
| Single-walled carbon nanotubes (SWCNTs) | Reactive blue 29 | Sorption | 66.3% | 5 | 240 | | | [218] |
| Alkali-activated carbon nanotubes CNTs-A | Methyl orange | Sorption | 149 mg/g | 2 | | | | [219] |
| | Methylene blue | | 399 mg/g | | | | | |
| Single-walled carbon nanotubes (SWCNTs) | Reactive red 120 | Sorption | 426.49 mg/g | 5 | 180 | 25 | | [220] |

**Table 1** (continued)

| Nanomaterial | Contaminant | Mechanism | Sorption/catalytic capacity | Studied conditions | | | Cycles | References |
|---|---|---|---|---|---|---|---|---|
| | | | | pH | Time | Temp °C | | |
| Acidified ammonium persulfate-treated single-walled carbon nanotubes (t-SWNTs) | Bisphenol A | Sorption | 8 mg/g | 7.5 | | | | [221] |
| | 17β-Estradiol | | 27.4 mg/g | | | | | |
| Carbon nanotubes (CNTs) | Cephalexin | Sorption | Up to 97.6% | 5 | | | | [222] |
| Multi-walled carbon nanotubes (MWCNTs) | Tetracycline | Sorption | 269.54 mg/g | 4.8 | 20 | 20 | | [223] |
| Multi-walled carbon nanotubes (MWCNTs) | Atenolol, caffeine, diclofenac and isoproturon | Sorption | | 3–9 | | | | [224] |
| Activated carbon (AC) | | | | | | | | |
| Carbon nanofibers (CNFs) | | | | | | | | |
| Single-walled carbon nanotubes (SWCNTs) | Ethidium bromide | Sorption | 36.10% | | 3 | 25 | | [225] |
| Carboxylate-functionalized single-walled carbon nanotubes (SWCNTs-COOH) | | | 38.42% | | 6 | | | |
| MWCNT-stabilized Pd/Fe nanocomposites | 2,4-Dichlorophenol | Sorption | Up to 95% | 4 | 120 | 30 | 3 | [226] |
| Cyclodextrin-phosphorylated MWCNT polymer | Co | Sorption | 67.7% | | | | | [227] |
| | 4-Chlorophenol | | 87% | | | | | |
| KOH-activated carbon nanotubes (CNTs-KOH) | Toluene | Sorption | 87.12 mg/g | 6 | | 20 | | [228] |
| | Ethylbenzene | | 322.05 mg/g | | | | | |
| | m-xylene | | 247.83 mg/g | | | | | |

**Table 1** (continued)

| Nanomaterial | Contaminant | Mechanism | Sorption/catalytic capacity | Studied conditions | | | Cycles | References |
|---|---|---|---|---|---|---|---|---|
| | | | | pH | Time | Temp °C | | |
| Ammonia-functionalized micron-sized activated carbon fibers (ACF) | Phenol | Sorption | 200 mg/g | | | 38 | | [229] |
| | $Pb^{2+}$ | | More | | | | | |
| Carbon nanofibers/activated carbon multiscale web (ACF/CNF) | $Pb^{2+}$ | | Less | | | | | |
| | Phenol | | 150 mg/g | | | | | |
| Carbon nanofibers | Ciprofloxacin | Sorption | 0.68 ± 0.04 mmol/g | 2–6 | | | | [230] |
| | Bisphenol | | 4.82 ± 0.22 mmol/g | | | | | |
| | 2-chlorophenol | | 6.18 ± 1.64 mmol/g | | | | | |
| Carbon nanotubes (CNTs) | $Cd^{2+}$ | Sorption | 2.02 mg/g | 7 | 120 | | | [231] |
| Carbon nanofibers (CNFs) | | | 1.22 mg/g | | | | | |
| Activated carbon (AC) | | | 1.98 mg/g | | | | | |
| Fly ash (FA) | | | 1.58 mf/g | | | | | |
| Multi-walled carbon nanotubes (MWCNTs) | Tetracycline | Sorption | 253.38 mg/g | 5–7 | 120 | 20 | | [232] |
| Carbon nanotubes (SWCNTs) | Amoxicillin | Sorption | 99.1% | | 45 | 50 | | [233] |
| Multi-walled carbon nanotubes (MWCNTs) | Diuron | Sorption | 29.75 mg/g | 7 | | 25 | | [234] |

**Table 1** (continued)

| Nanomaterial | Contaminant | Mechanism | Sorption/catalytic capacity | Studied conditions | | | Cycles | References |
|---|---|---|---|---|---|---|---|---|
| | | | | pH | Time | Temp °C | | |
| Multi-walled carbon nanotubes (MWCNTs) | Perflourooctane sulfonate | Sorption | 0.71 mmol/g | | | | | [235] |
| | Perfluorooctanoic acid | | 0.32 mmol/g | | | | | |
| | Perfluorooctanesulfonamide | | 1.37 mmol/g | | | | | |
| | 2,4-Dichlorophenoxyacetic acid | | 0.79 mmol/g | | | | | |
| | 4-*n*-Nonylphenol (4-nanoparticle) | | 0.83 mmol/g | | | | | |
| Multi-walled carbon nanotubes (MWCNTs) | Amoxicillin | Sorption | 22.9 mg/g | 4.6 | 120 | | | [236] |
| Activated carbon with different oxy-acids pf phosphorus | Trimethoprim | Sorption | 1.1478 | 10 | | | | [237] |
| AC-$H_3PO_4$ | | | | | | | | |
| AC-$H_4P_2O_7$ | | | 1.1896 | | | | | |
| AC-$HPO_3$ | | | 0.4098 | | | | | |
| AC-$H_3PO_3$ | | | 0.4084 | | | | | |
| Carbon nanofibers decorated with iron nanoparticles, porous carbon microbeads | Cr(VI) | Sorption | 41 mg/g | 2 | 1200 | | 5 | [238] |

under solar irradiation by providing numerous active sites for the photoreactions. The hybrid nanocomposite had reduced bandgap energy of 2.2 eV, facilitating electron/hole pair separation. A detailed analysis of the photocatalytic degradation of the MB dye shows that the connection of graphene oxide with anatase nanoparticles further improves the photocatalytic efficiency by prolonging the electron recombination. It is observed that the high graphene oxide loading may cause agglomeration which affects the electron transfer [246]. Hence, the incorporation of CNTs creates spaces between the sheets of GO, facilitating a connection between carbon-based materials and anatase particles. This improved connection between the carbon-based materials and $TiO_2$ then reduces the bandgap and enhances the photocatalytic activity. When the nanocomposite is exposed to solar light irradiation, the $es^-$ are excited from the VB to the CB of $TiO_2$. When a satisfactory connection is formed between anatase and the CNTs or GO, the $es^-$ can be easily transferred to both parts, causing electron–hole pair separation, generating highly active radicals for the degradation of dyes [247]. The MB degradation occurs through the following equations:

$$\text{Nanocomposite} + h\vartheta \rightarrow e^- + h^+ + \text{Nanocomposite}$$

$$h^+ + H_2O \rightarrow 2OH^{\bullet}$$

$$h^+ + OH^- \rightarrow OH^{\bullet}$$

$$MB + h^+ \rightarrow CO_2 + H_2O$$

$$MB + OH^{\bullet} \rightarrow CO_2 + H_2O$$

Wang et al. [248] exploited the efficiency of a novel biosorbent based on graphene oxide modified with persimmon tannin (PT-GO) fabricated with glutaraldehyde cross-linking, for the removal of MB dye. The PT provides a large number of active sites due to the presence of phenolic hydroxyl groups, while GO has abundant hydrophilic groups and also provides a large specific surface area. The modification of GO with PT therefore enhances its sorption capacity by providing stability and additional functionality. The highest sorption capacity obtained was 256.58 mg/g at optimal conditions of pH 8 and temperature of 323 K. The sorbent is rich in phenolic hydroxyl groups due to the presence of persimmon tannin and numerous hydrophilic groups associated with the graphene oxide portion of the sorbent. The mechanistic pathway for the sorption was attributed to electrostatic interactions, redox reactions, and π–π interactions. The analysis of the sorption process shows that the phenolic-hydroxyl groups of the biosorbent adhere to the cationic MB dye through electrostatic interactions. The second step involves the sorption process through a redox reaction between the sorbent and the dye, while a π–π interaction is created between the benzene rings of the dye and the biosorbent.

Firdaus et al. [249] functionalized graphene nano-platelets (GNPs) with oxygen-containing functional groups (acid oxidation). The functionalization of GNPs was performed using a 1:1 mixture of $H_2SO_4$ and $HNO_3$. The

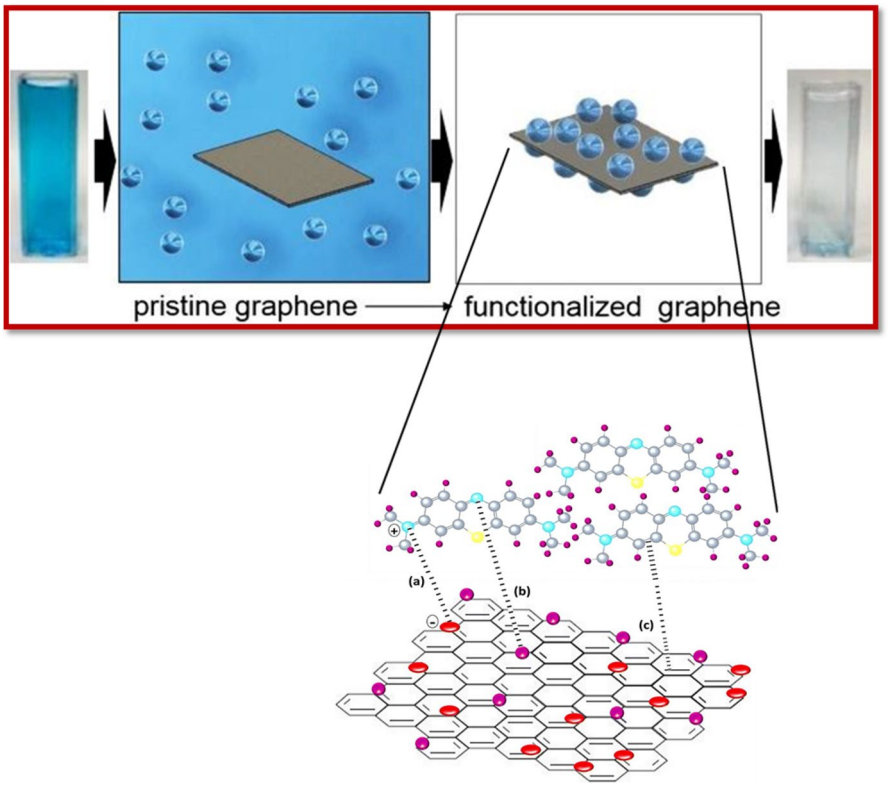


**Fig. 8** Schematic presentation of the MB adsorption on the f-GNP1 surface. Reproduced with permission [249], Copyright 2019, Springer Nature

functionalized GNPs showed higher sorption capacity (225 mg/g) for MB dye from an aqueous solution (Fig. 8). The higher sorption capacity of the functionalized GNPs was attributed to the enhanced surface area, pore size, and pore volume of the material due to the functionalization of the GNPs. Also, the functionalized GNPs showed stable dispersion in aqueous solution and better hydrophilicity. These properties induced by functionalization enhanced the sorptive capacity of the material towards contaminants.

Karimi-Maleh et al. [250] also studied the preparation of a magnetic nanocomposite sorbent based on reduced graphene oxide (rGO–$Fe_3O_4$) and used it for the removal of phenazopyridine, an azo dye having pharmaceutical attributes, and exhibited sorption capacity of 14.06 mg/g at the optimized conditions. The sorption of the contaminant over the surface of the sorbent was attributed to the presence of hydronium ions ($H_3O^+$) in the spaces between the graphene layers in the acidic conditions, leading to better sorption chances. The aromatic ring of the prepared sorbent and the amino group of the sorbate tend to interact, hence leading to better sorption capacity (Table 2).

**Table 2** Graphene-based nanomaterial in wastewater remediation

| Nanomaterial | Contaminant | Mechanism | Sorption/catalytic capacity | Conditions studied | | | Cycles | References |
|---|---|---|---|---|---|---|---|---|
| | | | | pH | Time | Temp °C | | |
| Graphene oxide | Metformin | Sorption | 122.61 mg/g | 6.2 | 180 | 20 | 6 | [251] |
| Reduced graphene oxide nanosheets doped with Cu | Methylene blue | Photocatalytic degradation | 91% | | 80 | | | [252] |
| Nickel(II) hydroxide ($Ni(OH)_2$)-decorated graphene oxide (GO) and modified titania ($TiO_2$) nanocomposite ($Ni(OH)_2/GO/TiO_2$) | 2-Chlorophenol | Photocatalytic degradation | 80% | 6 | 240 | | | [253] |
| Iron oxide/graphene oxide nanohybrid | 2,4-Dichlorophenol | Sorption | 96.5% | | | | | [254] |
| Reduced graphene oxide-CuO/ZnO (rGO-CuO/ZnO) | 4-Nitroaniline | Catalytic degradation | 98% | | 10 | | 4 | [255] |
| Poly(2-hydroxyethyl methacrylate) grafted graphene oxide | Cd | Sorption | 89% | 7 | 30 | 25 | | [256] |
| Polyaniline-functionalized magnetic graphene oxide composites (PANI-g-MGOs) | Cd(II) | Sorption | $7.63 \times 10^{-4}$ | 7 | | 25 | | [257] |
| | Phenol | | $2.87 \times 10^{-3}$ | | | | | |
| Surface-tailored graphene oxide paper | Methylene blue | Sorption | 311 mg/g | | | | | [258] |
| | Methyl orange | | 340 mg/g | | | | | |
| Silver nanoparticles immobilized on graphene oxide nanosheets | Methylene blue | Sorption | 633 mg/g | 9 | 90 | 27 | 4 | [259] |
| Magnetic graphene oxide ($Fe_3O_4/SiO_2$-GO) | Cd(II) | Sorption | 128.2 mg/g | 5 | 40 | 25 | 12 | [260] |
| | Pb(II) | | 385.1 mg/g | | | | | |
| Silver incorporated reduced graphene oxide sheets (Ag@rGO) | Methylene blue | Photocatalytic degradation | 100% | | 120 | | | [261] |
| Magnetic graphene oxide composite ($CoFe_2O_4$/GO) | Methylene blue | Sorption | 355.9 mg/g | | 400 | | 4 | [262] |
| | Rhodamine B | | 284.9 mg/g | | | | | |
| | Methyl orange | | 53 mg/g | | | | | |

**Table 2** (continued)

| Nanomaterial | Contaminant | Mechanism | Sorption/catalytic capacity | Conditions studied | | | Cycles | References |
|---|---|---|---|---|---|---|---|---|
| | | | | pH | Time | Temp °C | | |
| Magnetic graphene oxide-titanate composites (MGO@TNs) | Pb(II) | Sorption | 322.7 mg/g | 5 | 180 | | 6 | [263] |
| Magnetic porous reduced graphene oxide (MPrGO) | Triclosan | Sorption | 1105.8 mg/g | 3 | | | 5 | [264] |
| Yttrium-immobilized-graphene oxide-alginate hydrogel (Y-GO-SA) | As(V) | Sorption | 273.39 mg/g | 5 | | 20 | 4 | [265] |
| | Tetracycline | | 477.9 mg/g | | | | | |
| Graphene oxide | Trichloromethane | Photocatalytic degradation | 99.6% | | 5 | | | [266] |
| Graphene oxide/aminated lignin aerogels (GALA) | Malachite green | Sorption | 113.5 mg/g | 8 | 600 | 25 | | [267] |
| Polyethersulfone-functionalized GO (PES-fGO) | $Fe^{2+}$ | Sorption | 97.1% | | | | | [268] |
| | $Zn^{2+}$ | | 95.3% | | | | | |
| | $Cd^{2+}$ | | 92.7% | | | | | |
| | $Cr^{6+}$ | | 99.9% | | | | | |
| Amine-graphene oxide composite (pssN-GO) | Cr(VI) | Sorption | 260.74 mg/g | 3 | | | | [269] |
| Graphene oxide with lanthanum substituted manganese ferrites (LMFx%@GO) | Perfluorooctanoic acid | Sorption | 1.61 mg/g | 3 | 1440 | 25 | | [270] |
| Graphene-based hydrogel ($Fe_3O_4$/RGO/PAM hydrogel) | Rhodamine B | Photocatalytic degradation | 90% | 4.5 | 60 | | 10 | [271] |
| Graphene oxide wrapped magnetite nano-clusters ($Fe_3O_4$@GO) | Methylene blue | Sorption | 131.10 mg/g | 8 | 400 | 30 | | [272] |
| | Rhodamine B | | 34.5 mg/g | | | | | |
| | Methyl orange | | 39.95 g/g | | | | | |

**Table 2** (continued)

| Nanomaterial | Contaminant | Mechanism | Sorption/ catalytic capacity | Conditions studied | | | Cycles | References |
|---|---|---|---|---|---|---|---|---|
| | | | | pH | Time | Temp °C | | |
| Reduced graphene oxide | Methylene blue | Sorption | 2.6 g/g | | | | | [273] |
| | Congo red | | 7.6 g/g | | | | | |
| | Lemon yellow | | 3.2 g/g | | | | | |
| | $Cd^{2+}$ | | 8.4 g/g | | | | | |
| | $Pb^{2+}$ | | 17.9 g/g | | | | | |
| Graphene-based monolith using magnesium ascorbylphosphate (MAP/GBM) | Bisphenol A | Sorption | 324 mg/g | 7 | 2880 | 25 | 5 | [274] |
| Biochar supported reduced graphene oxide (RGO-BC) | $Pb^{2+}$ | Sorption | 26.10 mg/g | | 1440 | | 4 | [275] |
| | Atrazine | | 67.55 mg/g | | | | | |
| Sodium bisulfate reduced graphene oxide aerogels (S-rGO) | Tetrabromobisphenol A | Sorption | 128.37 mg/g | 7 | | 25 | 5 | [276] |
| Biochar-graphene nanosheets composites | Dimethyl phthalate | Sorption | 30.78 mg/g | | 2880 | | | [277] |
| | Diethyl Phthalate | | 23.86 mg/g | | | | | |
| | Dibutyl phthalate | | 21.98 mg/g | | | | | |
| Graphene oxide nanosheets | 17β-Estradiol (E2) | Sorption | 149.4 mg/g | 7 | 480 | 25 | 5 | [278] |
| Graphene oxide metal–organic framework nanocomposite (GO-MOF) | Methylene blue | Sorption | 97% | | 15 | | 4 | [279] |
| Cadmium sulfide reduced graphene oxide (CdS-RGO) | Rhodamine B | Sorption | 97.2% | | | | 4 | [280] |
| | Acid chrome blue K | | 65.7% | | | | | |
| Nickel ferrite-reduced graphene oxide (NFRGO) | Pb(II) | Sorption | 99% | | | | | [281] |

**Table 2** (continued)

| Nanomaterial | Contaminant | Mechanism | Sorption/ catalytic capacity | Conditions studied | | | Cycles | References |
|---|---|---|---|---|---|---|---|---|
| | | | | pH | Time | Temp °C | | |
| Graphene oxide/silver nanocomposite (GO-Ag) | Malachite green | Sorption | 143 mg/g | | 25 | 30 | 4 | [282] |
| | Ethyl violet | | 72 mg/g | | | | | |
| Graphene oxide-polydopamine-(β-cyclodextrin) (GPC) | Pb(II) | Sorption | 101.6 mg/g | 6 | 160 | | 5 | [283] |
| | Methylene blue | | 99.2% | | | | | |
| Silver/reduced graphene oxide nanocomposite (Ag/rGO) | Methyl orange | Photocatalytic degradation | 90% | 5.5 | 45 | | 3 | [284] |
| Graphene oxide/gold nanocomposite (GO-Ag) | Malachite green | Sorption | 1000 mg/g | | | 25 | 4 | [285] |
| | Ethyl violet | | 13.3 mg/g | | | | | |
| Silica-magnetic nanoparticle-decorated graphene oxide (GO-MNPs-$SiO_2$) | Naproxen | Sorption | 31 mg/g | 5 | 60 | | | [286] |
| Magnetic chitosan-graphene oxide composite ($^{m}$Ç-GO) | Acid red 17 | Sorption | 79% | 6 | 60 | 25 | 5 | [287] |
| | Bromophenol blue | | 97% | 2 | | | | |
| Reduced graphene oxide | Pb(II) | Sorption | 96.6% | 4.5 | 120 | 30 | 5 | [288] |
| Graphene oxide nanoflakes | Phenolic compound | Sorption | 19-30 mg/g | | 300 | | | [289] |
| Magnetic chitosan/graphene oxide biosorbent | $Cu^{2+}$ | Sorption | 217.4 mg/g | 8 | 70 | | 5 | [290] |
| Graphene oxide sheets decorated with polyaniline nanofibers (GO-PANI) | Zn(II) | Sorption | 297.62 mg/g | 7 | 20 | 25 | 3 | [291] |
| Graphene oxide (GO) | $Cu^{2+}$ | Sorption | 97% | 6 | 60 | 25 | 5 | [292] |
| Functionalized graphene oxide (GO-COOH) | | | 99.4% | | | | | |
| Cobalt oxide nanoparticles incorporated reduced graphene oxide A-rGO/$Co_3O_4$ | Rhodamine B | Sorption | 102.9 mg/g | 12 | 300 | 20 | | [293] |

**Table 2** (continued)

| Nanomaterial | Contaminant | Mechanism | Sorption/catalytic capacity | Conditions studied | | | Cycles | References |
|---|---|---|---|---|---|---|---|---|
| | | | | pH | Time | Temp °C | | |
| Palladium supported reduced graphene oxide (Pd NPs/RGO) | 4-Nitrophenol | Catalytic reduction | 97% | | 1 | | 8 | [294] |
| | Rhodamine B | | | | | | | |
| | Methylene blue | | | | | | | |
| Graphene oxide/cellulose hydrogel | Methylene blue | Sorption | 100% | 7 | 15 | 25 | 3 | [295] |
| | Rhodamine B | | 90% | | | | | |
| GO/polyethylenimine (PEI) hydrogels | Methylene blue | Sorption | 323.9 mg/g | | 250 | 25 | | [296] |
| | Rhodamine B | | 114.4 mg/g | | | | | |
| Polyacrylic acid-functionalized magnetic nanoparticles/graphene oxide composite | Methylene blue | Sorption | 291 mg/g | 7 | 1440 | | 5 | [297] |
| Poly(amidoamine)-functionalized graphene oxide (PAMAM-GO) | Se(IV) | Sorption | 60.9 mg/g | 6 | | | | [298] |
| | Se(VI) | | 77.9 mg/g | | | | | |
| Graphene oxide nanosorbents | Pb(II) | Sorption | 100% | 8 | | | | [299] |
| | Cr(VI) | | | | | | | |
| | Ni(II) | | | | | | | |
| P25/silver orthophosphate/graphene oxide (P25/$Ag_3PO_4$/GO) ternary composite | Rhodamine B | Photocatalytic degradation | 95% | | 60 | | 5 | [300] |
| Graphene oxide/magnesium oxide composite | Methylene blue | Sorption | 833 mg/g | 11 | 20 | | | [301] |
| Polysulfone-graphene oxide-based porous membranes | Ofloxacin, benzophenone-3, rhodamine B, diclofenac and Triton X-100 | Sorption | 90% | | 1440 | | 3 | [302] |

**Table 2** (continued)

| Nanomaterial | Contaminant | Mechanism | Sorption/ catalytic capacity | Conditions studied | | | Cycles | References |
|---|---|---|---|---|---|---|---|---|
| | | | | pH | Time | Temp °C | | |
| Graphene oxide | Levofloxacin | Sorption | 256.6 mg/g | | | | | [303] |
| | $Pb^{2+}$ | | 227.2 mg/g | | | | | |
| Poly(vinyl alcohol)/poly(acrylic acid)/carboxylate graphene oxide nanosheets (PVA/PAA/GO-COOH) | Methylene blue | Sorption | 25.91 mg/g | | 300 | | 10 | [304] |
| | Rhodamine B | | 6.75 mg/g | | | | | |
| | Congo red | | 9.62 mg/g | | | | | |
| Reduced graphene oxide | Methylene blue | Sorption | 746 mg/g | | 20 | | | [305] |
| 4-Aminodiphenylamine-modified graphene oxide | Toluene, ethylbenzene, and p-,o-xylene | Sorption | 1.5–3.7 mg/g | 4 | 5 | 23 | 7 | [306] |
| Dithiocarbamate-functionalized graphene oxide (GO-DTC) | Basic blue 41 | Sorption | 128.5 mg/g | 4.5 | 60 | 25 | 3 | [307]] |
| | Basic red 46 | | 111 mg/g | | | | | |
| Magnetic chitosan-coated graphene oxide ($Fe_3O_4$©-GO) | Methyl violet | Sorption | 11.5 mg/g | 10 | 60 | 25 | 4 | [308] |
| | Alizarin yellow R | | 6.7 mg/g | 6 | | | | |
| $Ag_3PO_4$/graphene-oxide ($Ag_3PO_4$/GO) composite | Methyl orange | Photocatalytic degradation | 86.7% | | 30 | | | [309] |
| | Rhodamine B | | 100% | | | | | |
| Polydopamine-kaoline with reduced graphene oxide (PDA-rGO-kaoline) | Methylene blue | Sorption | 39.66 mg/g | 7 | | 27 | 5 | [310] |

### 4.3 Fullerenes

Another important form of carbon-based NMs is fullerenes. The fullerenes are composed entirely of carbon atoms, considered as allotropes of carbon. Compared with graphite and diamond, fullerenes are found to be spherical molecules [311, 312]. They show solubility in various organic solvents. The structural elucidation of fullerenes shows that they consist of a carbon cage with a fused ring system mainly comprising hexagons and pentagons. The most generally accessible members of the fullerenes are the $C_{60}$ and $C_{70}$. The most important property of the fullerenes is their high symmetry [313]. Wu et al. [314] performed photocatalytic degradation of RB dye using fullerene-cored star-shaped polyporphyrin-incorporated $TiO_2$. The ZnCPP-fullerol@$TiO_2$ photocatalyst was prepared by immobilizing fullerene-cored star-shaped polyporphyrin nanospheres, obtained from the esterification of carboxyl porphyrin with fullerols, of the $TiO_2$ surface through excess hydroxyl groups of fullerols. The results showed that 94.7% efficiency was obtained for the degradation of RB dye. The good efficiency of the prepared catalyst is attributed to the presence of fullerol, which is a derivative of fullerene and is extensively hydroxylated. The properties of fullerol including its high specific surface area, unique electronic properties, and conjugated aromatic system are the reasons for its use as a charge carrier and photocatalyst. The polyhydroxy groups present on the surface of the fullerene provide high-density active sites. Also, multiple functional groups can be introduced on the surface of fullerenes by the esterification reaction of the hydroxy groups. This synthetic procedure of a molecular-level heterojunction NM accelerates the electron transfer between porphyrin molecules, promoting charge separation. The combined properties of heterogeneous and homogeneous catalysts will enhance photocatalytic degradation efficiency. Elessawy et al. [315] prepared functionalized magnetic fullerene nanocomposites (FMFN) through the catalytic thermal decomposition method. The prepared FMFN was used as a sorbent for the removal of the ciprofloxacin contaminant. FMFN had a high surface area of 336.84 $m^2/g$ typical of mesoporous and microporous volumes. The saturation magnetization property of FMFN was 7.002 emu/g, confirming its high superparamagnetism. These properties obtained through the functionalization provided a better sorption efficiency (Fig. 9). The highest sorption capacity obtained for the removal of ciprofloxacin was found to be 65 mg/L, which is in complete agreement with the magnificent sorptive ability of FMFN.

Mahdavian [316] analyzed the removal efficiency of heavy metals (nickel and cadmium) by filtration of modified nano-fullerene ($C_{60}$) with tetrahydrofuran. The heavy metal ion sorption was optimized and the results showed that about 91% efficiency was obtained for the removal of ions. A sorption efficiency of 1261 mg/g was obtained for cadmium removal, while sorption capacity of 3704 mg/g was obtained for nickel removal (Table 3).

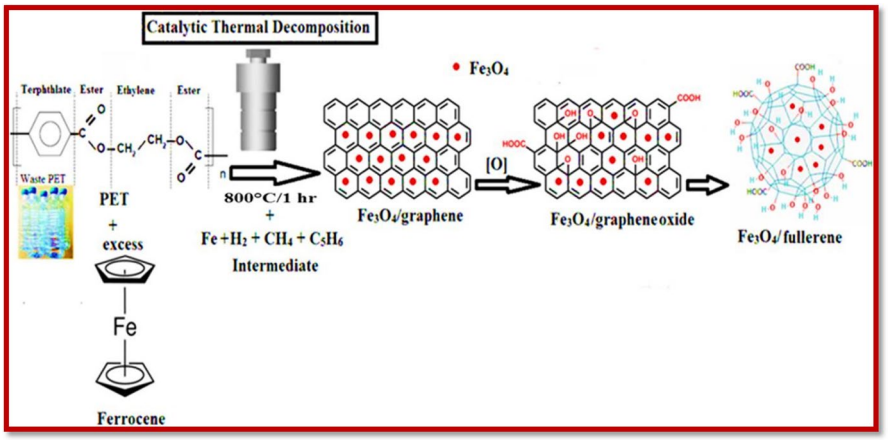


**Fig. 9** One-step polyethylene terephthalate catalytic dissociation for the synthesis of functionalized magnetic fullerene nanocomposites (FMFN) and different kinds of interactions for the sorption of ciprofloxacin. Reproduced with permission [315], Copyright 2020, Elsevier

## 5 Functionalized Metal Oxide Nanomaterials as Potential Sorbents for Contaminant Removal

Metal oxides have remained in the spotlight for researchers working in areas such as chemistry, physics, and polymer sciences. Metal oxides can inhibit the nano-sized structural geometry exhibiting metallic, semiconductor, or insulating characteristics. These metal-based nanoparticles are exceptionally mobile in permeable media because of their small size and high reactivity due to the very high surface-to-volume ratio [330–332]. The high surface area to mass significantly enhances the sorption limits of nanosorbent materials. Because of their facile synthesis, high efficiency, and simplicity of characterization, nanoparticles have been increasingly explored in recent years [333]. Metal nanoparticles have magnificent electrical and optical properties, reactivity, and solid mechanical quality, and thus offer an incredible opportunity to create NM-based sensors and devices for observing environmental contamination in air, water, and soil [334]. These include iron [335], aluminum [336], titanium [337], and zinc [338].

### 5.1 Single Metal Oxide Nanomaterials

The most frequently utilized form of metal oxide nanoparticles comprises a single kind of metal in its oxide form. Some of the single metal oxides that can serve as potent agents for environmental remediation purposes are discussed in detail below.

#### 5.1.1 Iron Oxide Nanoparticles

Among the various metal oxides, iron oxide nanoparticles are widely used in pollutant remediation process [339]. Iron oxide-based NMs are further divided into three

**Table 3** Fullerene-based nanomaterial in wastewater remediation

| Nanomaterial | Contaminant | Mechanism | Sorption/catalytic capacity (%) | Studied conditions | | | Cycles | References |
|---|---|---|---|---|---|---|---|---|
| | | | | pH | Time (min) | Temp °C | | |
| $C_{60}$-modified ZnAlTi layered double oxide (ZnAlTi-LDO) | Bisphenol A | Photocatalytic degradation | 85 | 7 | 60 | 28 | | [317] |
| Fullerene ($C_{60}$)/CdS nanocomposite | Rhodamine B | Photocatalytic degradation | 97 | | 40 | | 3 | [318] |
| [$PdCl_2$, $H_2PtC_{l6}{\cdot}nH_2O$ & $Y(NO_3)_3$] Doped $TiO_2$ | Methylene blue | Photocatalytic degradation | | | | | | [319] |
| $C_{60}$ | 17 CB congeners | Sorption | | | | | | [320] |
| Polyhydroxy fullerene (PHF) coated $TiO_2$ | Procion red MX-5B | Photocatalytic degradation | 66–74 | | 360 | | | [321] |
| Hydroxylated fullerene (fullerenol) | Diethyl phthalate (DEP) | Degradation | 100 | 3.5 | 60 | | | [322] |
| Hydroxylated fullerene | Chloramphenicol (CAP) | Degradation | 90 | 3 | 60 | | | [323] |
| Fullerenol (polyhydroxyfullerene, PHF) | Acid red 18 | Photocatalytic degradation | 86.7 | < 8 | 60 | | 4 | [324] |
| [60]Fullerene-functionalized magnetic nanoparticles ($Fe_3O_4$@$SiO_2$@$C_{60}$) | Polycyclic aromatic hydrocarbons (PAHs) | Sorption | 92.4–106.9 | 3–12 | 2–10 | | 10 | [325] |
| Titania nanotubes (TiNTs) functionalized with fullerenes ($C_{60}$) | Isopropanol | Photocatalytic degradation | 100 | | 660 | | | [326] |
| Nanocomposites of $TiO_2$ and single fullerene ($C_{60}$) molecule | Methyl orange | Photocatalytic degradation | | | 30 | | | [327] |
| Rutile-$C_{60}$ composites | Methylene blue | Photocatalytic degradation | 100% | | 240 | | | [328] |
| Fullerene modified $C_3N_4$ ($C_{60}$/$C_3N_4$) composites | Rhodamine B | Photocatalytic degradation | 97% | | 60 | | 5 | [329] |

forms: magnetite ($Fe_3O_4$), maghemite ($Fe_2O_3$), and hematite ($Fe_2O_3$) nanoparticles. These nanoparticles possess unique features such as high saturation magnetization, vast surface area, and a large number of active sites for the sorption of metals. Also, the magnetic properties facilitate the isolation of the magnetic nanoparticles from an aqueous medium [340, 341].

### 5.1.2 Magnetite ($Fe_3O_4$) Nanoparticles

Iron oxide/magnetite nanoparticles possess an opposite spinel structure, with oxygen having a cubic cluster, with half of Fe(III) cations having tetrahedral sites and others having octahedral sites [342]. The magnetite is ferrimagnetic in nature and possesses superexchange oxygen-mediated coupling, thus allowing the iron particles to have inverse magnetic moment directions. In magnetite, the Fe(III) quantity is similar in all cross-sectional sites; hence their magnetic moment cancels each other. As a result, the net polarization is attributed to Fe(II) cations [343]. The features of these magnetic NMs change drastically from mass to nanometer size. As the size decreases, the attractive material changes from a multi-domain structure to a solitary area structure, with novel magnetic properties. These magnetic nanoparticles show amphoteric surface action, simple scattering capacity, and a high surface-to-volume ratio, affording high metal ion sorption capacity [344]. Magnetite nanoparticles are further stabilized by various organic/inorganic supports and then used in the sorption and photocatalytic degradation of environmental contaminants [345] (Fig. 10).

Song et al. [346] exploited an iron oxide-activated persulfate system for the simultaneous removal of Cr(VI) and triclosan (TCS). The operation was based on the utilization the sulfate radicals ($SO_4^{\cdot -}$) as efficient substances for the degradation of triclosan along with the removal of Cr(VI). At optimized conditions, the removal

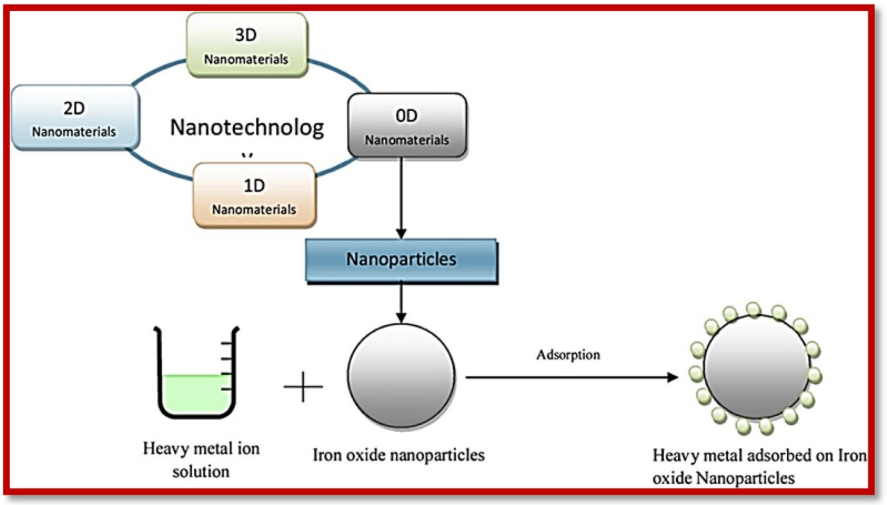


**Fig. 10** Illustration of 2D magnetic iron oxide nanoparticles for heavy metal removal. Reproduced with permission [345], Copyright 2019, Elsevier

efficiency obtained for Cr(VI) removal was 99.5%, while 87.5% degradation of TCS was achieved. The possible mechanism was that Fe(II) from iron oxide activation of persulfate produces $SO_4^{\cdot-}$ radicals that react with water, producing OH˙. This hydroxyl radical will cause the degradation of triclosan. At the same time, Cr(VI) is sorbed on the surface of iron oxide, causing the reduction reaction of both Cr(VI) and Fe(II), resulting in the oxidation of iron to Fe(III) and reduction of chromium to Cr(III) [347]. The final forms of both Fe(III) and Cr(III) will co-precipitate on the iron oxide surface, forming Cr–Fe (oxy) hydroxide. This indicates the successful removal of both contaminants.

D'Cruz et al. [348] prepared iron oxide nanoparticles coated with activated carbon (AC-$Fe_3O_4$composite) as a potential sorbent for the removal of an antipsychotic drug, promazine, from wastewater. The results revealed complete removal of promazine, wit sorption capacity of 101.1 mg/g, within a period of 6 min. This fastest and highest removal efficiency (99.9%) was attributed to the electrostatic interactive forces created between the sorbent and the sorbate. This mechanism was determined by optimizing the pH and creating a range of isoelectric points for the nanocomposite and promazine. The studies revealed that below pH 9.3, the sorbent is positively charged, hence promoting attractive forces for the negatively charged promazine particles, exhibiting better sorption ability.

Magnaccaet al. [349] examined the efficiency of $Fe_3O_4$ nanoparticles (NPs) coated with soluble bio-based products (SBO) as prospective sorbents for the removal of pollutants in wastewater. The biosorbent was prepared following the co-precipitation method [350], and the prepared particles had a diameter of 10 nm. CV dye was used as a target to check the sorption efficiency of the prepared SBO-coated nanoparticles. The results showed greater efficiency, as the useful properties of both nanoparticles and a bio-based product were incorporated. NPs with different amounts of SBO were tested, and NP/0.5 demonstrated the highest sorption capacity of 85%. This was attributed to the fact that higher negative charges on the surface of NP/0.5 exhibited greater attraction towards the cationic CV dye, leading to better sorption at neutral pH.

Giri et al. [351] prepared magnetic nanoparticles from waste iron ore tailings by co-precipitation of its aqueous acidic solution along with ferrous iron under an inert atmosphere. The prepared magnetic nanoparticles (MNPs) were utilized for the sorption of MB and Congo red (CR) dyes to evaluate the removal efficiency of the prepared MNPs. The MNPs showed greater sorption capacity of 70.4 mg/g and 172.4 mg/g for MB and CR, and hence proved to be an excellent sorbent. The fast rate of sorption was ascribed to the absence of any internal diffusion, with the sorption occurring only on the surface of the MNPs. The sorption ability had a considerable influence on the pH of the medium, which followed different trends for the two dyes. The increase in pH results in a negative charge on the surface of the NPs, leading to enhanced sorption of the cationic dye (MB) and decreased sorption of anionic dye (CR). In contrast, increased sorption was observed at low pH for anionic dye due to the development of a positive charge at lower pH.

### 5.1.3 Maghemite (γ-$Fe_2O_3$) Nanoparticles

There are many reports of organic polymer-supported maghemite nanoparticles. Nanosized iron oxide particles are widely used in different industrial processes including the manufacture of semiconductors, recording materials, catalysts, and gas sensor materials [252]. Afkhami and Moosavi [352] prepared maghemite nanoparticles by a co-precipitation method and assessed the efficiency of the prepared nanoparticles for the removal of CR dye. The highest sorption capacity was 208.33 mg/g (pH ~ 5.9). The mechanism of greater sorption efficiency of the dye was explained based on the pH of zero-point charge, $pH_{zpc}$, where below $pH_{zpc}$, the surface of the sorbent is positively charged, making it available for the sorption of anionic dye. Additionally, CR and metal oxides develop a coordination effect, leading to sorption.

Behera et al. [353] studied the removal of hexavalent chromium based on sodium dodecyl sulfate (SDS)-modified maghemite nanoparticles. The highest removal efficiency of 95.8% was obtained for chromium at a pH of 2.6. The study of the sorption of chromium at lower pH showed that, at lower pH, chromium exists in various oxyanion forms including $H_2CrO_4$, $HCrO_4^-$, $CrO_4^{2-}$, and $Cr_2O_7^{2-}$. At lower pH values, the $H^+$ could be sorbed to $SO_4^-$ ions of the SDS and form complexes with $Cr_2O_7^{2-}$ and $HCrO_4^-$ through electrostatic interactions, indicating the removal of hexavalent chromium ions. Minisy et al. [354] prepared poly(*p*-phenylenediamine)/maghemite (PPDA/γ-$Fe_2O_3$) composites by oxidative polymerization. The prepared sorbent exhibited excellent sorption capacity towards Reactive Black 5, an anionic dye. The highest sorption capacity obtained was 223 mg/g at the optimized working conditions. The positively charged PPDA-doped maghemite tends to attract the anionic Reactive Black 5 dye, promoting efficient sorption. The sorption mechanism tends to follow the electrostatic interaction along with the π-π stacking of the aromatic rings.

### 5.1.4 Hematite (α-$Fe_2O_3$) Nanoparticles

Hematite nanoparticles can also be used as sorbents for the removal of various environmental pollutants because of their properties such as stability at ambient conditions and environmentally friendly n-type functional material and semiconductor [355]. Kefeniet al. [356] studied the synthesis of hematite nanoparticles and utilized them as sorbents for the removal of various metal ions from acid mine drainage (AMD) confirming the efficiency of these nanoparticles for wastewater remediation. The highest efficiency of up to 80% was achieved for the removal of various metal ions. The possible pathway for the removal of metal ions in the sorption and the formation of various metal oxides on the surface of the hematite resulted in its removal. Saadet al. [357] reported a novel hematite@chitosan core/organic shell nanocomposite (HCS) to remove Pb(II), Cu(II), and Cd(II) ions from industrial wastewater. Both hematite nanoparticles and chitosan have unique sorption properties. Hematite nanoparticles have a high surface area and high saturation magnetization, while chitosan is a naturally occurring polysaccharide and has excellent properties for the

sorption of metal ions by ion exchange as well as by coordination linkage mainly due to the presence of the $–NH_2$ group in the chitosan matrix [358]. The highest sorption capacity obtained for Pb(II), Cu(II), and Cd(II) was 476.1 mg/g, 117.6 mg/g, and 135.1 mg/g, respectively.

### 5.1.5 Titanium dioxide ($TiO_2$) Nanoparticles

Titanium dioxide ($TiO_2$) and zinc oxide (ZnO) are widely used for photocatalytic activity. Titanium dioxide is a photocatalyst that has been used in solar cells, paints, and coatings. $TiO_2$ in the anatase phase has been of particular interest due to its high oxidization power for organic contaminants, chemical stability, and low cost [359]. It is commercially used as a photocatalyst [360]. Supporting elements such as sand, glass, or zeolite enhance the separation efficiency of nanocrystalline $TiO_2$. Magnetic separation provides a very convenient approach for removing and recycling magnetic particles such as magnetite, ferrite, and barium ferrite by applying external magnetic fields. The incorporation of magnetic components into $TiO_2$ nanoparticle-based catalysts may therefore enhance the separation and recovery of nanosized $TiO_2$ [361]. Photocatalysis appears to be a very efficient pretreatment process for wastewater streams containing organic matter.

Malakootian et al. [362] analyzed the photocatalytic degradation efficiency of $TiO_2$ immobilized on the surface of a glass plate for ciprofloxacin. The benefit of using glass as a supporting agent for $TiO_2$ is to enhance the life span as well as the reusability of the catalyst. The degradation of ciprofloxacin begins with the production of $e^-/h^+$ pairs when an illumination source is provided (Fig. 11). These pairs of $e^-/h^+$ cause the generation of hydroxyl radicals or other radicals by reaction with $H_2O$. These produced radicals act as oxidizing agents for the degradation of ciprofloxacin. Another possibility for the degradation of ciprofloxacin is the direct reaction of the produced holes with the ciprofloxacin. Additionally, the $e^-$ tends to reduce ciprofloxacin or produce superoxide radicals ($O_2^{-\bullet}$) that can mineralize the contaminants [363].

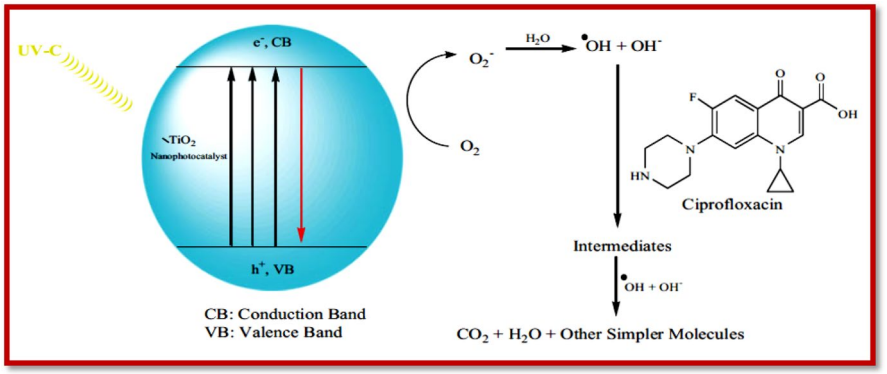


**Fig. 11** A schematic explanation of UV irradiation for ciprofloxacin degradation on $TiO_2$ immobilized on the surface of a glass plate. Reproduced with permission [362] Copyright 2020, Informa UK Limited

### 5.2 Binary Metal Oxide Nanomaterials

One process that has drawn attention is the consumption of more than one metal in a combinational form to utilize the useful properties associated with each one of them promoting better results. Two or more metals incorporated as one compound are widely used for wastewater decontamination purposes due to the increased surface area, parallel redox reactions/ion-exchange reactions, and reduced agglomeration probability, eventually enhancing the sorption rate as well as the degradation rate as sorbents or photocatalysts, respectively [364]. Binary metal oxides generally represented as $M_1/M_2O$ are a continuation of this approach.

Mohanta et al. [365] studied the preparation of iron-zirconium binary oxide (IZO) as an efficient sorbent through the co-precipitation method. The prepared material had a surface area of 200.307 $m^2/g$, which is sufficient for maximum sorption. The prepared sorbent was utilized for the removal of CR, an anionic dye, and showed greater efficiency, with sorption capacity of 171 mg/g. The removal of the dye was attributed to the electrostatic interactions and hydrogen bonding between the sorbate and sorbent molecules. Once the pH of the solution is decreased, the surface of the sorbent becomes positively charged and the $H^+$ concentration in the solution is quite high. This enables the convenient removal of the anionic dye, CR in this case.

Du et al. [366] performed phosphate ion removal by preparing a bimetallic nanocomposite, incorporating a binary metal oxide (La-Zr) into the porous structure of a polymeric anion exchanger (D201). The obtained La-Zr-D201 offers specific sorption of the phosphate ions through a ligand exchange strategy. The highest sorption capacity obtained by the prepared ion-exchanger was noted as 61.31 mg/g, while phosphate treatment capacity of 1350 BV was also obtained.

### 5.3 Ternary Metal Oxide Nanomaterials

Ternary metal oxide nanoparticles comprising three metals are also trending for the removal of the contaminants. Ghasemipour et al. [367] prepared ternary nanocomposites for the photocatalytic degradation of aniline by doping ZnO onto $MoS_2$, followed by grafting on reduced graphene oxide and carbon nanotubes. The coupling of the transition metal sulfide inhibits the recombination of the charges, hence enhancing the photocatalytic activity. The incorporation of rGO and CNTs further enhances the catalytic activity. The results showed that at the optimized conditions, the photocatalytic activity of rGO10%/ZnO20%/$MoS_2$ and CNT10%/ZnO20%/$MoS_2$ was 84% and 76%, respectively. The difference in the photocatalytic efficiency between the catalysts was attributed to the sorption efficiency of the prepared photocatalyst, which is greater for the rGO-modified photocatalyst than the modified CNTs due to their larger $S_{BET}$ values.

Eniola et al. [368] also prepared binary and ternary metal hydroxides and utilized them for the removal of an antibiotic, oxytetracycline. The binary and ternary hydroxides were made using copper, aluminum, and manganese metals as binary CuAl-hydroxide, MnAl-hydroxide, and ternary CuMnAl-hydroxide. The sorption capacity of the prepared sorbents was in the decreasing order of

CuMnAl-hydroxide > CuAl-hydroxide > MnAl-hydroxide. The mechanism for the sorption of the antibiotic drug was attributed to the electrostatic interaction, hydrogen bonding, and anion exchange. FTIR studies were performed to confirm the sorption of OTC onto the surface of metal hydroxides and predicting the mechanism of sorption. The results showed a decrease in the band intensities and a change in position of the bands of the metal hydroxide after sorption as compared with before sorption material, predicting the electrostatic interaction between the OTC and MH. The OH band sharpness was considerably reduced indicating the presence of hydrogen bonding after sorption, while peaks of exchangeable ions such as $SO_4^{2-}$ disappeared, indicating the anion exchange between the sorbent and the sorbate, confirming the sorption efficiency of the prepared materials. The highest sorption capacity possessed by the ternary hydroxide was found to be 250.07 mg/g.

### 5.4 Other Metal Oxide Nanoparticles

Apart from iron and titanium oxides, several other metal oxides have been exploited to date for the removal of various contaminants [369, 370]. These metal oxides exhibited greater contaminant removal properties based on the small size and higher surface-to-volume ratios. These metal oxides include ZnO [371], CuO [372], $Al_2O_3$ [373], $CeO_2$ [374], $SiO_2$ [375] PbO [376], and $SnO_2$ [377], to name a few.

Debnath and Mondal [378] followed a green approach for the synthesis of zinc oxide nanoparticles using leaf extracts of *Hibiscus rosa-sinensis* with the aim of reducing the cost and complexity associated with the commercial methods of nanoparticles preparation. ZnO has been frequently utilized as a potent photocatalyst based on its wide bandgap of 3.37 eV; hence, it could be used in UV [379]. At present, its sorptive properties have also been explored against various contaminants. Here, the prepared ZnO nanoparticles were used for the removal of CR dye. Removal efficiency of 95.5% was exhibited by the prepared ZnO nanoparticles for the removal of CR dye in 20 min contact time at a pH of 4. The possible mechanism of the sorption was explained based on electrostatic interaction forces between the ZnO and the azo group of the dye. The amine group of dye molecules may exhibit some attraction towards the ZnO nanoparticles, leading to efficient removal of the dye.

Rafique et al. [380] investigated the green synthesis of copper oxide nanoparticles by utilizing leaf extract of *Citrofortunella microcarpa* (Calamondin) for the efficient removal of RB. CuO exhibits a bandgap of 1.35 and 3.5 eV and has proved to be efficient semiconductors suitable for performing the photocatalytic degradation of wastewater contaminants [381]. The prepared CuO nanoparticles exhibited excellent efficiency, with photocatalytic degradation of RB dye up to 98% at the optimized conditions. The mechanism for the removal of dye through photocatalytic degradation is shown in Eqs. (1–8):

$$\mathrm{CuO} + h\vartheta \rightarrow \mathrm{e}^{-}(\mathrm{CBCuO}) + h^{+}(\mathrm{VBCuO}) \tag{1}$$

$$2\mathrm{CuO} + \mathrm{H_2O} + \mathrm{e}^{-} \rightarrow 2\mathrm{Cu} + 2\mathrm{OH}^{-} \tag{2}$$

$$2CuO + 2OH^- \rightarrow 2CuO + H_2O + 2e^- \quad (3)$$

$$e^-(CBCuO) + h^+(VBCuO) \rightarrow \text{recombination} \quad (4)$$

$$e^- + O_2 \rightarrow O_2^- + H_2O \rightarrow OH_2\text{.} + OH^- \quad (5)$$

$$h^+ + OH^- \rightarrow OH^{\cdot} \quad (6)$$

$$OH^{\cdot} + \text{RhB dye} \rightarrow \text{degradation products} \quad (7)$$

$$h^+ + \text{dye} \rightarrow \text{dyeoxidation} \rightarrow \text{degradation} \quad (8)$$

The radicals produced in the above reactions are mainly responsible for the degradation of the dye.

Zhang et al. [382] studied the preparation of γ-$Al_2O_3$ nanoparticles through a hydrothermal process for the successful removal of anionic CR dye. The highest sorption capacity exhibited by the prepared sorbent for the removal of the CR dye was 465.82 mg/g. A comparison was made to evaluate the sorption capacity of the γ-$Al_2O_3$ nanoparticles by evaluating the sorption of other cationic dyes such as MB and malachite green. The results indicated that the sorbent demonstrated poor sorption capacity for the cationic dyes as compared to the CR. This was explained based on the presence of sulfonate groups on the surface of the CR dye in the form of $SO_3^-$, which gave rise to electrostatic interactions with the surface of the sorbent dye, leading to efficient removal. Another factor involved in the removal of the dye is the presence of an amino group that promotes the hydrogen bonding with the hydroxyl group, leading to their strong interaction. Additionally, the azo bonds present on the surface of the CR dye leads to the development of a hydrogen bond with the hydroxyl group. Hence, the sorption of dye is attributed to both the electrostatic and hydrogen bonding forces between the dye and the sorbent particles.

Liu et al. [383] also synthesized cerium oxide nanoparticles laminated with lignin for the efficient removal of phosphate. The prepared L-$NH_2$@Ce exhibited a surface area of 89.8 $m^2$/g and a pore volume of 0.23 $cm^3$/g. The sorption capacity exhibited by the prepared sorbent was 27.86 mg/g. The exceptionally high sorption capacity was attained at mildly acidic conditions with pH 5. This might be because, in alkaline conditions, there is competition between $OH^-$ and $PO_4^{3-}$ ions for attaching to the surface of the sorbent, leading to reduced sorption of phosphate. Li et al. [384] fabricated an anion exchange resin D201, with nanosized hydrous zirconium oxide (HZrO) for successful removal of vanadium(V). Favorable sorption capacity of 118.1 mg/g was achieved for the removal of V(V), confirming the excellent capability of the prepared HZrO@D201HZrO@D201 sorbent. The removal of the contaminant was attributed to the nonspecific ion exchange and electrostatic interactions between the resin and the V(V). The resin incorporated in the prepared sorbent is a macroporous anionic resin that can attract negatively charged ions, while the zirconium lamination exhibits a positive

charge, which also promotes the negative charge attraction through electrostatic interaction at high pH, thus promoting the sorption of V(V) (Table 4).

## 6 Functionalized Metal Selenide Nanomaterials

Metal selenides belong to a class of semiconductor nanostructures called chalcogenides. Over the past decade, metal selenide nanostructures have taken nanotechnology to the next level [452]. The remarkable features of metal selenide nanoparticles include their surface-to-volume ratios, optical and field emission properties, and photocatalytic activity. Based on these properties, metal selenides are being exploited in various fields including field-effect transistors [453], light-emitting diodes (LED) [454], solar cells [455], and wastewater remediation [456]. The commonly utilized metal selenides include ZnSe [457], CdSe [458], SnSe [459], PbSe [460], $FeSe_2$ [461], CuSe [462], and CdTe [463].

Ghaedi et al. [464] explored the preparation of cadmium selenide nanoparticles loaded on activated carbon (CdSe-NP-AC), utilized for the successful removal of muroxide (MO) from aqueous solution. Sorption capacity of 333 mg/g was achieved at the optimized experimental conditions. Sharifpour et al. [465] studied the preparation of starch-capped zinc selenide nanoparticles loaded on an activated carbon (ST-Zn-Se-NPs-AC) composite, which was used for the removal of basic fuchsin (BF) dye. The prepared composite demonstrated high removal efficiency, with sorption capacity of 222.72 mg/g at the optimized operating conditions.

### 6.1 Binary Metal Selenide Nanomaterials

The binary metal selenides incorporate two metals in the form of selenides, providing a composite suitable for water remediation applications. Ali et al. [466] studied the photocatalytic performance of prepared chitosan-bismuth cobalt selenide hybrid microspheres for the removal of CR dye. The prepared selenide tri-composite had a narrow bandgap of 2.48 eV, while the average size of the microspheres was found to be 734 µm.

The prepared BCSN-CM photocatalyst showed an excellent removal percentage of 85% for the CR dye at the optimized conditions and was successfully reused for up to five successive cycles. The idea of utilizing chitosan as a capping agent for the metal selenides nanoparticles was to avoid the leaching of the catalyst. The mechanism of the degradation of the CR dye was based on the redox reactions taking place on the surface of the catalyst, and most of the degradation was associated with the production of $^{\cdot}OH$ and $O_2^{\cdot-}$ radicals according to the typical photocatalytic mechanism. Altaf et al. [467] explored binary transition metal selenide ($V_3Se_4$), ($Nb_2Se_3$, $Nb_2Se_9$), and ($TaSe_3$, $Ta_2Se_3$) preparation through the hydrothermal method. The prepared catalyst was used for the photocatalytic degradation of MB. The prepared photocatalyst had wider bandgap

**Table 4** Metal oxide nanomaterial in wastewater remediation

| Nanomaterial | Contaminant | Mechanism | Sorption/catalytic capacity | Conditions studied | | | Cycles | References |
|---|---|---|---|---|---|---|---|---|
| | | | | pH | Time | Temp °C | | |
| Magnetic nanoparticles composite with silestone and biochar (MNPs/EDB/SS) | Cd | Sorption | 117.38 mg/g | 8 | 120 | 25 | | [385] |
| Magnetic nanoparticles activated with biochar (QBC/MNPs) | Cr(VI) | Sorption | 77.35 mg/g | 4 | 180 | | 5 | [386] |
| Magnetic nanoparticles | Cd(II) | Sorption | 42.3 mg/g | 6 | | | | [387] |
| | Pb(II) | | 42.5 mg/g | | | | | |
| | Zn(II) | | 42.9 mg/g | | | | | |
| Magnetic nanoparticles coated with surfactants (MNPs-CPC) | Sb(V) | Sorption | 113.63 mg/g | 4.3 | | 25 | | [388] |
| Magnetite-functionalized boron nitride nanosheets (BNNS-$Fe_3O_4$) | As(III) | Sorption | 30.3 mg/g | 8 | 500 | | 5 | [389] |
| Iron oxide incorporated with mesoporous biochar | Ofloxacin | Sorption | 19.74 mg/g | 6 | 300 | 25 | 5 | [390] |
| Monolayers of *N*-(2-aminoethyl)-3-aminopropyltrimethoxysilane onto magnetic nanoparticles (MSM) | Cr(VI) | Sorption | 8 mg/g | 4 | 120 | | 5 | [391] |
| Magnetite | | | | | | | | |
| M1 | Pb & Cd | Sorption | 408.14 and 228.05 mg/g | 6 | 1440 | 56 | 6 | [392] |
| M2 | | | 331.40 and 170.86 mg/g | | | | | |
| M3 | | | 178.47 and 83.49 mg/g | | | | | |
| Magnesium-doped magnetic nanoparticles | As(V) | Sorption | 33.71 mg/g | 8–11 | | 25 | 5 | [393] |

**Table 4** (continued)

| Nanomaterial | Contaminant | Mechanism | Sorption/catalytic capacity | Conditions studied | | | Cycles | References |
|---|---|---|---|---|---|---|---|---|
| | | | | pH | Time | Temp °C | | |
| Magnetic nanoparticles embedded Gum-ghatti-graft-poly(4-acryloylmorpholine) hydrogel (Ggh-*g*-PAcM/$Fe_3O_4$) | Methylene blue | Sorption | 116.8 mg/g | 7 | 45 | 30 | 1 | [394] |
| | Rhodamine B | | 137.8 mg/g | | | | | |
| | Cu(II) | | 249.9 mg/g | | | | | |
| | H(II) | | 235.1 mg/g | | | | | |
| Three-dimensional (3D) magnetic bacterial cellulose nanofiber/graphene oxide polymer aerogel (MBCNF/GOPA) | Malachite green | Sorption | 270 mg/g | 12 | 25 | 25 | 8 | [395] |
| Chitosan coated magnetic nanoparticles | Copper | Sorption | 1.03 mg/g | 6 | 90 | | 5 | [396] |
| | Chromium | | 0.20 mg/g | | | | | |
| | Arsenic | | 0.04 mg/g | | | | | |
| | Phenol | | 0.56 mg/g | | | | | |
| Tin magnetic nanocomposites (Sn-CCMN) | Alizarin yellow | Sorption | 92% | 7 | 120 | 25 | 4 | [397] |
| ZnO-magnetic/ZSM-5 | Disperse blue 56 | Sorption | 6.23 mg/g | 3 | 15 | | 5 | [398] |
| $NiFe_2O_4$-COF-chitosan-terephthaladehyde nanocomposites film (NCCT) | Tetracycline | Sorption | 388.52 mg/g | 8 | | | 6 | [399] |
| | Cefotaxime | | 309.26 mg/g | 4 | | | | |
| Magnetic magnetite nanoparticles | Boron | Sorption | 4.57 mmol/g | 5 | 300 | 45 | 3 | [400] |
| Biochar-modified iron oxide nanoparticles (MBC) | Caffeine | Sorption | 75.1 ± 1.8 mg/g | 8 | 5 | 35 | 5 | [401] |
| | Ibuprofen | | 39.9 ± 1.2 mg/g | | | | | |
| | Acetylsalicylic acid | | 149.9 ± 4.5 mg/g | | | | | |
| $SnFe_2O_4/ZnFe_2O_4$ Heterojunctions | Tetracycline | Photocatalytic degradation | 93.2% | | 120 | | 4 | [402] |

**Table 4** (continued)

| Nanomaterial | Contaminant | Mechanism | Sorption/catalytic capacity | Conditions studied | | | Cycles | References |
|---|---|---|---|---|---|---|---|---|
| | | | | pH | Time | Temp °C | | |
| g-$C_3N_4$/NiO/ZnO/$Fe_3O_4$ nanohybrid | Esomeprazole | Photocatalytic degradation | 95% | 6 | 70 | | 5 | [403] |
| N-doped $TiO_2$/$SiO_2$-based nanomagnetic photocatalyst (N-$TiO_2$@$SiO_2$@$Fe_3O_4$) | Paraquat (PQ; 1,1′-dimethyl-4,4′-bipyridinium dichloride) | Photocatalytic degradation | 85% | 6 | 180 | | 8 | [404] |
| $TiO_2$-loaded magnetic MOFs composite ($TiO_2$/mag-MIL-101(Cr)) | Bisphenol F | Photocatalytic degradation | 90% | | 60 | | 5 | [405] |
| | Acid red 1 | | | | | | | |
| Magnetic $Fe_3O_4$/$ZnWO_4$/$CeVO_4$ nanoparticles | Methyl violet | Photocatalytic degradation | 90% | | | | | [406] |
| | Methylene blue | | 70% | | | | | |
| $TiO_2$@$ZnFe_2O_4$/Pd nanocomposite | Diclofenac | Photocatalytic degradation | 86.1% | 4 | 120 | | 5 | [407] |
| Carboxymethyl-β-cyclodextrin-modified $Fe_3O_4$@$TiO_2$ (CMCD-$Fe_3O_4$@$TiO_2$) | Polychlorinated biphenyl | Photocatalytic degradation | 83% | | 16 | 25 | 5 | [408] |
| $ZnFe_2O_4$@$TiO_2$/Cu nanocomposite | Naproxen | Photocatalytic degradation | 80.73% | 4 | 120 | | 5 | [409] |
| $Fe_3O_4$ magnetic nanoparticles (MNP) | Nitrobenzene | Photocatalytic degradation | 73.13% | 2 | 120 | 25 | | [410] |
| Lanthanum substituted spinel ferrite ($La_xMnFe_{2-x}O_4$) nanoparticles | Crystal violet dye | Photocatalytic degradation | 95% | | 90 | | | [411] |
| $Fe_3O_4$/$TiO_2$/CuO nanoparticle | Methylene blue | Photocatalytic degradation | 99% | 7 | 22 | | 4 | [412] |
| $TiO_2$ magnetic nanoparticles (T-MNPs) | Ceftazide | Photocatalytic ozonation | 75.5% | 11 | 15 | | 6 | [413] |
| Core/shell nanocomposite of phosphomolybdic acid immobilized on magnetic alumina ($Fe_3O_4$@$Al_2O_3$-PMo) | Cibacron brilliant yellow | Photocatalytic degradation | 90% | 7.2 | 240 | | 5 | [414] |

**Table 4** (continued)

| Nanomaterial | Contaminant | Mechanism | Sorption/catalytic capacity | Conditions studied | | | Cycles | References |
|---|---|---|---|---|---|---|---|---|
| | | | | pH | Time | Temp °C | | |
| Surface-modified hematite NPs ($\alpha$-$Fe_2O_3$ $NP_s$) | $Pb^{2+}$ | Sorption | 111 mg/g | 6.5 | 120 | 25 | | [415] |
| Hematite iron oxide NPs $\alpha$-$Fe_2O_3$ | Malachite green | Sorption | 86.13% | | 45 | | | [416] |
| Hematite ($\alpha$-$Fe_2O_3$) nanoparticles | $Cr^{6+}$ | Sorption | | | 30 | | | [417] |
| Polyacrylonitrile (PAN) with embedded hematite ($\alpha$-$Fe_2O_3$) NPs | As(V) | Sorption | 5 mg/g | 6 | | | | [418] |
| | Cu(II) | | 19 mg/g | | | | | |
| PAN/$Fe_2O_3$@$Fe_2O_3$ nanofibers | Cr(VI) | | 3.9 mg/g | | | | | |
| Disc-like hematite ($\alpha$-$Fe_2O_3$) NPs | $Ni^{2+}$ | Sorption | 62.5 mg/g | 6 | | | | [419] |
| | $Cd^{2+}$ | | 200 mg/g | | | | | |
| Hematite ($\alpha$-$Fe_2O_3$) NPs | $Cu^{2+}$ | Sorption | 105 ± 7 mg/g | 6–9.5 | 300 | | | [420] |
| | $Ni^{2+}$ | | 104 ± 7 mg/g | | | | | |
| | $Co^{2+}$ | | 80 ± 6 mg/g | | | | | |
| | $Cd^{2+}$ | | 96 ± 7 mg/g | | | | | |
| | $Pb^{2+}$ | | 100 ± 0.6 mg/g | | | | | |
| Hematite ($\alpha$-$Fe_2O_3$) NPs | Rose Bengal dye | Sorption | 1810 mg/g | 5 | | 30 | | [421] |
| Nano-$\alpha$-$Fe_2O_3$ NPs | Co-60 | Sorption | 142.86 mg/g | 6.5 | 120 | 25 | | [422] |
| Hematite ($\alpha$-$Fe_2O_3$) NPs | Crystal violet | Sorption | 100% | | 30 | | | [423] |
| | Methylene blue | | | | 40 | | | |
| Hematite/lignosulfonate composite (HLS) | Cd(II) | Sorption | 39.03–53.65 mg/g | | 200 | | | [424] |
| Mesoporous maghemite NPs $\gamma$-$Fe_2O_3$ | Methylene blue | Sorption | 36 mg/g | 10 | | | | [425] |

**Table 4** (continued)

| Nanomaterial | Contaminant | Mechanism | Sorption/catalytic capacity | Conditions studied | | | Cycles | References |
|---|---|---|---|---|---|---|---|---|
| | | | | pH | Time | Temp °C | | |
| Maghemite nanoparticles coated *Bacillus subtilis* | $Cd^{2+}$ | Sorption | 32.6 mg/g | 4 | 60 | 30 | | [426] |
| Starch-functionalized maghemite nanoparticles ($\gamma$-$Fe_2O_3$@starch) | As(III) | Sorption | 8.60 mg/g | 2–9 | | | | [427] |
| Montmorillonite-based magnetic nanoparticles (Mt@MH) | Pb(II) | Sorption | 38.15 mg/g | 6.5 | 480 | 25 | 5 | [428] |
| | As(V) | | 19.10 mg/g | 3.5 | | | | |
| Novel nanoadsorbents based on core–shell bimagnetic nanoparticles ($CoFe_2O_4$@$\gamma$-$Fe_2O_3$) | Cr(VI) | Sorption | 15.6 mg/g | 2.5 | 20 | 25 | 3 | [429] |
| Chitosan coated iron oxide nanoparticles | Cr(VI) | Sorption | 162.54 mg/g | 3.7 | 21.84 | | 7 | [430] |
| Al-doped nano-$TiO_2$ | Methylene blue | Photocatalytic degradation | 85% | | 30 | | | [431] |
| $TiO_2$ | CN | Photocatalytic degradation | 80% | 10 | | | | [432] |
| | Cr(VI) | | | 2.3 | | | | |
| $TiO_2$-coated glass sheet | Methylene blue | Photocatalytic degradation | 93% | 11 | 60 | | 20 | [433] |
| $TiO_2$ deposited on polyethylene terephthalate (PET-$TiO_2$) | Carbendazim (CBZ) | Photocatalytic degradation | 80% | | | | | [434] |
| | Caffeine (CAF) | | | | | | | |
| g-$C_3N_4$ nanosheets implanted $TiO_2$ nanotube (TCNs) | Tetracycline | Photocatalytic degradation | 100% | | 120 | | | [435] |
| Zinc oxide NPs (ZnO NPs) | Methylene blue | Photocatalytic degradation | 100% | 7 | 60 | 25 | | [436] |
| | Rhodamine B | | | | 50 | | | |
| Zinc oxide NPs (ZnO NPs) | Dibenzothiophene (DBT) | Photocatalytic degradation | 97% | 7 | 180 | | 5 | [437] |
| Zinc oxide NPs (ZnO NPs) | Rhodamine B | Photocatalytic degradation | 98% | | 200 | | | [438] |

**Table 4** (continued)

| Nanomaterial | Contaminant | Mechanism | Sorption/catalytic capacity | Conditions studied | | | Cycles | References |
|---|---|---|---|---|---|---|---|---|
| | | | | pH | Time | Temp °C | | |
| Cobalt oxide NPs (CoNPs) | Direct yellow-142 | Catalytic reduction | 93.37% | | 60 | | | [439] |
| | Methyl orange | | 96.24% | | | | | |
| Magnetic cobalt oxide nanoparticles (CONP) | Malachite green | Sorption | 238.10 mg/g | 7 | 120 | | 4 | [440] |
| Cobalt ferrite composite nanoparticles ($CoFe_2O_4$) | Acid black 1 | Photocatalytic degradation | 80% | | 120 | | | [441] |
| | Reactive red 4 | | 61% | | 105 | | | |
| Copper-doped $ZrO_2$ NPs | Methyl orange | Photocatalytic degradation | 98% | | 100 | | | [442] |
| Copper oxide NPs (CuO NPs) | Nile blue | Photocatalytic degradation | 93% | | 120 | | | [443] |
| | Reactive yellow 160 | | 81% | | | | | |
| Nickel oxide nanoparticles (NiO NPs) | Ciprofloxacin | Sorption | 99.8% | 3 | 100 | 25 | | [444] |
| Zinc oxide nanoparticles impregnated Pea peels (ZnONPs-IPPs) | Chlorpyrifos | Sorption | 47.846 mg/g | 2 | 60 | 30–50 | | [445] |
| Zinc oxide NPs | Methylene blue | Photocatalytic degradation | 80% | | 120 | | | [446] |
| Chitosan-zinc sulfide nanoparticles (CS-ZnS-NPs) | Acid brown 98 | Photocatalytic degradation | 92.6% | 6 | 165 | 33 | 4 | [447] |
| | Acid black 234 | | 96.7% | 7 | 100 | | | |
| $CoCrFeO_4$ oxide chitosan-composite beads ($CoCrFeO_4$-CB) | Acid black | Photocatalytic degradation | 100% | | 120 | 35 | 5 | [448] |
| | Acid brown | | 93% | | | | | |
| | Congo red | | 85% | | | | | |
| $SnO_2$ NPs | Methylene blue | Photocatalytic degradation | 64.42% | | 120 | | | [449] |
| Sodium iron disulfide ($NaFeS_2$) | Methylene blue | Photocatalytic degradation | 97% | | 105 | | | [450] |
| | Indigo carmine | | 99% | | 45 | | | |
| Binary titanium oxides ($Sm_2Ti_2O_7$) | Rhodamine B dye | Photocatalytic degradation | 94% | | 80 | | | [451] |

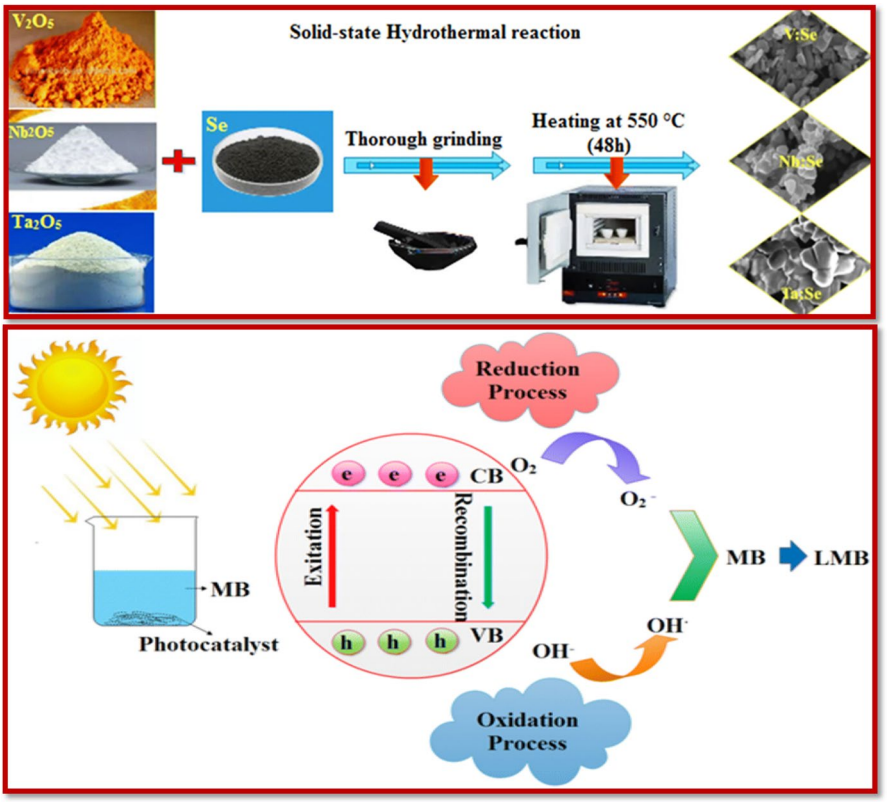


**Fig. 12** Schematic illustration of the metal selenide and their photocatalytic activity. Reproduced with permission [467], Copyright 2020, Springer Nature

energy of 3.87, 3.82, and 3.95 eV, respectively, for each semiconductor photocatalyst. Degradation efficiency of up to 90% was obtained. Figure 12 explains both the synthesis and photocatalytic activity of binary transition metal selenides ($V_3Se_4$), ($Nb_2Se_3$, $Nb_2Se_9$), and ($TaSe_3$, $Ta_2Se_3$).

### 6.2 Ternary Metal Selenides

Attention has recently been focused on the incorporation of multiple metals for the design of ternary metal selenides. The idea of designing ternary metal selenides provided the opportunity to incorporate different metals for achieving better and refined results. Nisar et al. [468] prepared ternary metal selenide/chitosan microspheres and utilized them for evacuating Alizarin Red S dye. The prepared TMS-CMs were morphologically found to have an average diameter of 33 nm. The prepared photocatalyst had a bandgap of 1.8 eV and presented excellent photocatalytic degradation with efficiency of up to 95.4%. The reaction followed a first-order kinetics model (Table 5).

## 7 Functionalized Metal Sulfides Nanomaterials

Another diverse class of NMs consists of metal sulfides, which exist in nature in the form of minerals. They are cheap, abundant, and easily available entities, and hence are widely used by researchers in the various fields. Functionalization of the metal sulfides further enhances their ability, making them suitable for use in the field of environmental remediation [487].

### 7.1 Single Metal Sulfide Nanoparticles

The majority of metal sulfides have been used to date based on their useful properties. Some of the commonly utilized ones include $FeS_2$ [488], CoS [489], CuS [490], $Ag_2S$ [491], ZnS [492], and $Bi_2S_3$ [493].Wang et al. [494] prepared tin sulfide using $Sn^{2+}$ as a tin source, an oxidizer ($H_2O_2$), a sulfur source (L-cysteine) to form $SnS_2$ nanosheets with a 10 nm thickness. The prepared nanosheets were used for the sorptive removal of RB dye and showed excellent efficiency with a sorption capacity of 200 mg/g. The greater sorption rate was achieved for the removal of RB dye through electrostatic interactions formed between the cationic dye and the negatively charged surface of the sorbent. The decreased sorption with time was attributed to the covering of the active sites by the dye molecules resulting in repulsion instead of attraction leading to decreased sorption.

Mishra et al. [495] developed ferrous sulfide (FeS) and carboxyl-functionalized ferroferric oxide (CFFO) nanoparticles, which were introduced into the polyvinylidene fluoride (PVDF) matrix (individually/mixed in an optimal ratio) following the phase inversion technique. The morphological evidence showed that both FeS and CFFO nanoparticles had a surface area of 7.22 and 89.2$m^2$/g respectively, while the pore volume was recorded to be 0.382 and 0.031$cm^3$/g. The prepared FeS/CFFO/PVDF membrane was then utilized for the removal of heavy metal ions particularly Pb, Cd, Cr, and As the obtained removal efficiency for the said metal ions was 88% for Cr(VI), 99% for $Cd^{2+}$, 99% for $Pb^{2+}$ and 95% for As(Fig. 13).

Sun et al. [496] prepared nanoscale FeS-$Fe_3O_4$ nanocomposites using chitosan as a stabilizer (CTO-MFeS). The as-synthesized nanocomposite had a size of 20 nm, while the specific surface area was recorded to be 21.3$m^2$/g. The CTO-MFeS were used for the removal of $Hg^{2+}$ ions based on the sorption as well as the precipitation phenomena. The highest sorption capacity obtained for the removal of mercury ions was noted to be $72.34 \pm 3.18$ mg/g.

### 7.2 Binary Metal Sulfide Nanomaterials

Binary metal sulfides are also trending based on the idea of fusing the properties of both the metals being used, enhancing the activity of the tailored material. Yu et al. [497] prepared strontium titanate/binary metal sulfide ($SrTiO_3$/$SnCoS_4$) heterostructure through a two-step hydrothermal method. The efficiency of the

**Table 5** Metal selenide-based nanomaterial in wastewater remediation

| Nanomaterial | Contaminant | Mechanism | Sorption/catalytic capacity | Conditions studied | | | Cycles | References |
|---|---|---|---|---|---|---|---|---|
| | | | | pH | Time | Temp °C | | |
| Iron-bismuth selenide chitosan microspheres | Crystal violet | Photocatalytic degradation | 98.95% | 8 | 150 | | 4 | [469] |
| Selenium-functionalized metal–organic framework MIL-101 Se/MIL-101 | Mercury | Sorption | 148.19 mg/g | | 90 | | | [470] |
| Copper selenide-functionalized polyurethane sponge $Cu_2Se$/PUS | Mercury | Sorption | 25.90 mg/g | | | | | [471] |
| CdSe (cadmium selenide)-decorated graphene composites coupled with $TiO_2$ (titanium oxide) | Methyl orange Rhodamine B | Photocatalytic degradation | 85% | | 180 | | 4 | Ghosh et al. [472] |
| Selenized magnetic nanoparticles ($Fe_3O_{4-x}Se_y$) | Mercury | Sorption | 98.1% | | 120 | 100 | 10 | [473] |
| Nanosized copper selenide | Mercury | Sorption | 210.8 mg/g | | 90 | 50 | | [474] |
| CuSe/ZIF-8 | Mercury | Sorption | 309.8 mg/g | | 240 | 50 | | [475] |
| Selenide-coated copper ($Cu_2Se$-Cu) | Mercury | Sorption | 100% | | 120 | 60 | | [476] |
| Molybdenum selenide nanosheets | Mercury | Sorption | 1000 mg/g | | | | | [477] |
| Amorphous molybdenum selenide intercalating magnetite [$MoSe_x$(inter)$Fe_3O_4$] | Mercury | Sorption | 100% | | 240 | | 10 | [478] |
| Marcasite-type metal selenides ($MSe_2$) | Mercury | Sorption | | | | | | [479] |
| Zinc selenide sulphide composite $ZnSe_{0.7}S_{0.3}$ | Mercury | Sorption | 99% | | 120 | 150 | | [480] |
| Selenide-functionalized mineral sulfide *x*Se-FeS | Mercury | Sorption | 87% | | 120 | 90 | 4 | [481] |

**Table 5** (continued)

| Nanomaterial | Contaminant | Mechanism | Sorption/ catalytic capacity | Conditions studied | | | Cycles | References |
|---|---|---|---|---|---|---|---|---|
| | | | | pH | Time | Temp °C | | |
| C fibers@$MoSe_2$ nanoplate core–shell composite | Methylene blue | Photocatalytic degradation | | | 80 | | | [482] |
| | Rhodamine B | | | | | | | |
| | *p*-Chlorophenol (4-CP) | | | | | | | |
| | Potassium dichromate | | | | | | | |
| Amorphous $MoSe_x$ | Rhodamine B | Photocatalytic degradation | 96.7% | | 120 | | | [483] |
| | Methylene blue | | 98.9% | | | | | |
| $MoSe_2/TiO_2$ nanofibers | Rhodamine B | Photocatalytic degradation | | | | | 3 | [484] |
| | Tetracycline hydrochloride | | | | | | | |
| | $K_2Cr_2O_7$ | | | | | | | |
| Copper selenide | 2-Chlorophenol | Photocatalytic degradation | 100% | | | | | [485] |
| CuSe nanoparticles | Methylene blue | Photocatalytic degradation | 76% | | 720 | 90 | | [486] |
| | Rhodamine B | | 87% | | | | | |

prepared nanocomposite was checked by performing the photocatalytic degradation of methyl orange dye under visible light. The results showed 95% degradation confirming the potential of the photocatalyst for environmental remediation purposes.

Kalpana and Selvaraj [498] developed novel ZnS/SnS/A-FA nanorods by providing pristine reactants(fly ash as supporting material, zinc nitrate hexahydrate, stannous chloride dihydrate, and sodium sulfide) at ambient temperature. According to the Brunauer–Emmett–Teller (BET) analysis, the ZnS/SnS/A-FA nanorods have a specific surface area of 93.73 $m^2$/g. The prepared ZnS/SnS/A-FA nanorods were used for the photocatalytic degradation of CR dye. The results obtained confirmed the removal efficiency of about 90% by the prepared nanorods (Table 6).

## 8 Functionalized Zero-Valent Metal Nanomaterials

The oxidation state of the metal in the nanoparticles is a key factor for predicting the efficiency of the material. Apart from the oxides and hydroxides of the metals, lower-oxidation-state metal nanoparticles in their pristine state have also been proved to be efficient scavengers of wastewater contaminants. Such metals are generally found in their zero-valent states and are represented as zero-valent nanometals (ZVNMs). Nanoscale elemental metals have been massively utilized for their unique properties. One such example is zero-valent iron nanoparticles. The zero-valent iron nanoparticles tend to be more powerful reducing agents and have been exploited for the removal of various contaminants to date [523].

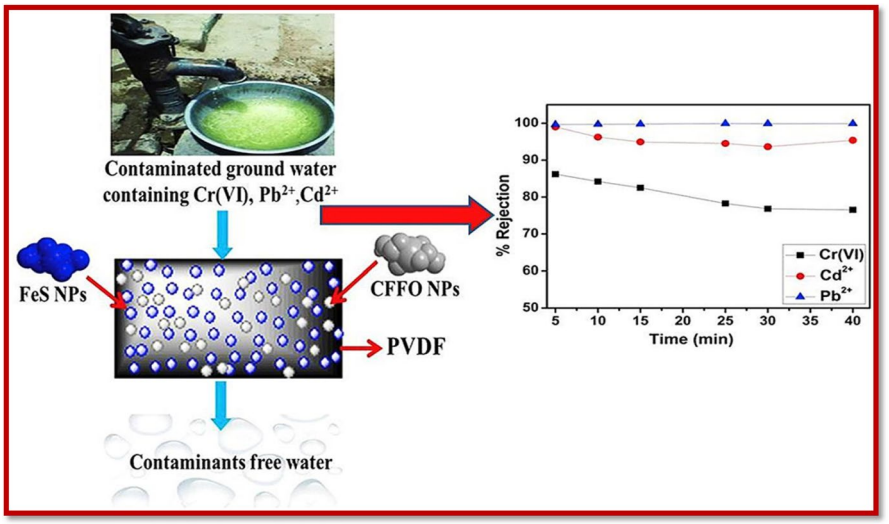


**Fig. 13** Schematic explanation of the removal of toxic heavy metal from wastewater through PVDF-based nanocomposite membranes. Reproduced with permission [495], Copyright 2020, Elsevier

### 8.1 Transition Metal/d-Block Nanomaterials

Among the NMs, transition metal nanoparticles have emerged as a promising choice based on their superlative properties. The availability of literature on the utilization of transition metal nanoparticles confirms their efficiency as catalysts. Shi et al. [524] prepared bentonite-supported zero-valent iron nanoparticles by the liquid-phase reduction method. The prepared material was used for the efficient removal of Cr(VI) with sorption efficiency of 90%. Increased sorption of chromium was observed at pH 2, which was explained based on the fact that nZVI corrosion is enhanced at lower pH, diminishing the precipitation of Cr(III) and Fe(III) hydroxides on the iron surface and thus accelerating the sorption process.

Ali and Khan [525] focused on exploiting multiple zero-valent metals including Ni, Cu, and Ag MNPs, loaded onto the surface of sodium polyacrylate (water ball) for catalytic degradation of contaminants. The idea of preparation was to first sorb the metal particles on polymer support and then convert them into their zero-valent state by a reducing agent. The water ball is considered a superabsorbent; i.e., it has the capacity for absorbing material greater than its weight. The prepared substance was used for the removal of 4-nitrophenol (4-NP), 4-aminophenol (4-AP), methyl orange (MO), CR, and MB dyes. The 4-NP was reduced with the addition of $NaBH_4$ along with the addition of the catalyst. A redshift in the peak from 318 to 400 nm of 4-nitrophenol was observed with the addition of $NaBH_4$. This was attributed to the conjugation when the OH proton of phenol forms the phenolate anion by the activity of $NaBH_4$ and the negative charge needs a more electronegative atom to reside on. This is the reason the negative charge is delocalized on the oxygen atom more than the lone pair of electrons of OH and the wavelength shift towards a longer side. The same is the case for 4-AP, which is also reduced by the addition of both $NaBH_4$ and the catalyst. The removal of anionic dyes up to 98% was observed by the addition of the catalysts. The results showed that the catalyst is the necessary counterpart of $NaBH_4$ for better removal of the contaminants, leading to environmental remediation.

Devi et al. [526] studied the efficiency of plasmonic metal nanoparticles including Ag and Au nanoparticles for the photocatalytic degradation of harmful dyes malachite green (MG) and MB (Fig. 14). The noble metal nanoparticles were prepared using a green approach with extracts of *Hydrocotyle asiatica* as a reducing and stabilizing agent. Firstly, the degradation of MB was performed in the dark using the catalyst followed by solar irradiation in the presence of the catalyst. The results showed that 57% degradation was obtained with no light, and no prominent shift in the wavelength was observed. However, the solar irradiation enhanced the degradation rate to 94%, with a blueshift in wavelength from 617 to 570 nm. No additional peaks were observed, which confirmed that no leuco forms of the dye were formed [527]. In the case of MG, a different behavior was observed due to the different nature of the dye. It is known that MG exists in multiple forms at different pH including chromatic $MG^+$ at pH 3–5, protonated $MGH^+$ at pH 2, and a colorless carbinol base at pH above 8, all forms having different lambda max. By considering the effect of pH, the reaction was carried out at different pH and the results indicated a shift of wavelength from 617 to 570 nm with the removal of the dye under solar

**Table 6** Metal sulfide-based nanomaterial in wastewater remediation

| Nanomaterial | Contaminant | Mechanism | Sorption/ catalytic capacity | Conditions studied | | | Cycles | References |
|---|---|---|---|---|---|---|---|---|
| | | | | pH | Time | Temp °C | | |
| $CuS/K_2S_2O_8$ | Orange II | Photocatalytic degradation | 98.88% | | 120 | | 3 | [499] |
| Copper sulfide | Orange carbon | Photocatalytic degradation | 99.8% | | 60 | | | [500] |
| $SnO_2/Cu_xS/TiO_2$ | Phenol | Photocatalytic degradation | 100% | 9 | 360 | | | [501] |
| $Cu_xS/TiO_2$ composites | Methyl orange | Photocatalytic degradation | 99% | | 300 | | | [502] |
| | Methylene blue | | 99% | | 180 | | | |
| $CuS\text{-}TiO_2$ composites | Methylene blue | Photocatalytic degradation | 94% | | 180 | | 4 | [503] |
| CuO-CuS core–shell nanowires | Methylene blue | Photocatalytic degradation | 89% | | 240 | | | [504] |
| ZnO/CuS heterostructures | Methylene blue | Photocatalytic degradation | 87% | 7 | 30 | | | [505] |
| CuS-CdS | Methylene blue | Photocatalytic degradation | 99.97% | | 10 | | 5 | [506] |
| Copper sulfide nanocrystals/graphene nanocomposites (CuS/GR) | Methylene blue | Photocatalytic degradation | 94% | | 80 | | | [507] |
| $g\text{-}C_3N_4/CuS$ nanocomposites | Rhodamine B | Photocatalytic degradation | 99.6% | | 60 | | 3 | [508] |
| | Methylene blue | | 99% | | 120 | | | |
| CuS-rGO nanocomposite | Congo red | Photocatalytic degradation | 98.76% | 5 | 90 | | 5 | [509] |
| $Cu_2O@Cu_7S_4$ core–shell micro/nanocrystals | Methyl orange | Photocatalytic degradation | | | | | | [510] |
| Ultrafine CuS nanocrystalline/Fe-doped $TiO_2$ nanotubes hybrids | Malachite green | Photocatalytic degradation | 100% | 5 | | | | [511] |
| Graphene/CuS/ZnO hybrid nanocomposites | Methyl orange | Photocatalytic degradation | 99% | | 30 | | | [512] |
| $CuS/MoS_2$ | Methylene blue | Photocatalytic degradation | 100% | | 60 | | | [513] |
| CuS/ZnS core/shell nanocrystals (NCs) | Rhodamine B | Photocatalytic degradation | 100% | | 30 | | 5 | [514] |
| $CuS(5)CdS(5)/TiO_2$ | Acid orange 7 | Photocatalytic degradation | 100% | 10 | 100 | | | [515] |
| $CuS/g\text{-}C_3N_4$ composites | Methylene blue | Photocatalytic degradation | | | 90 | | 5 | [516] |
| Molybdenum sulphide ($MoS_2$) nano-petals | Rhodamine B | Photocatalytic degradation | 96% | | 25 | | 5 | [517] |
| Sodium dodecyl sulfate intercalated molybdenum disulfide (SDS-$MoS_2$) | Cr(VI) | Sorption | 63.92 mg/g | 5 | 732 | | | [518] |

**Table 6** (continued)

| Nanomaterial | Contaminant | Mechanism | Sorption/ catalytic capacity | Conditions studied | | | Cycles | References |
|---|---|---|---|---|---|---|---|---|
| | | | | pH | Time | Temp °C | | |
| Molybdenum disulfide/reduced graphene oxide ($MoS_2$/rGO) composites | Pb(II) | Sorption | 384.16 mg/g | 5 | 400 | 25 | | [519] |
| Fe(II)-promoted activation of peroxymonosulfate by molybdenum disulfide | Acetaminophen (ACT) | Photocatalytic degradation | 94.5% | 3 | 180 | | | [520] |
| Biochar modified with molybdenum disulfide $MoS_2$@biochar | Pb(II) | Sorption | 189 mg/g | 5 | 180 | 25 | 7 | [521] |
| PVP/$MoS_2$ | Cr(VI) | Sorption | 142.24 mg/g | 5 | 1440 | 25 | | [522] |

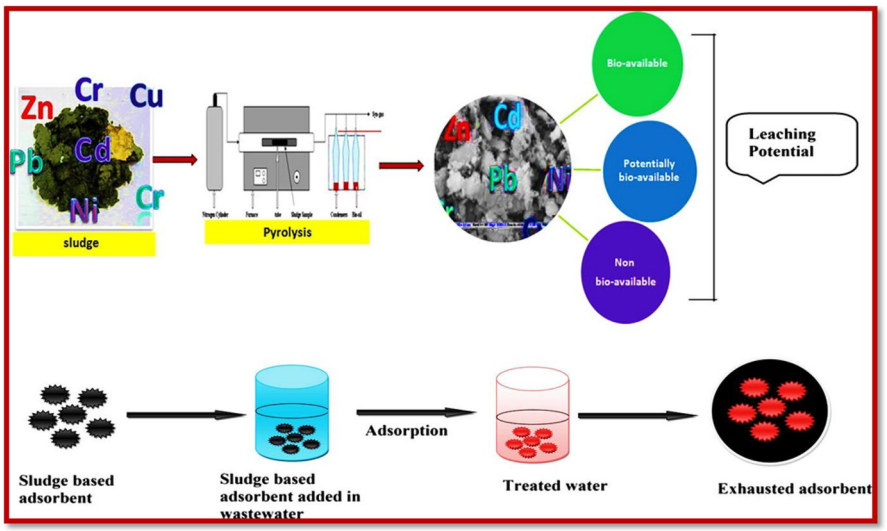


**Fig. 14** The synthesis and application of sludge-based new adsorbents for the decontamination of wastewater. Reproduced with permission [526], Copyright 2016, Springer Nature

irradiation [528]. The mechanism of the degradation process was explained based on hot electron production on the surface of the Ag nanoparticles by the intraband transition of electrons [529]. The green synthesis of Ag nanoparticles leads to the production of negatively charged surface nanoparticles with zeta potential −34.9 mV. Thus, the cationic dyes can sorb onto its surface through electrostatic interaction, while the electrons may degrade the dyes into simpler products. The blueshift in the lambda max is rendered to the *N*-demethylated intermediates formed during the degradation of dyes. The auxochromic groups are removed, decreasing the intensity of the peaks. It was concluded that the whole mechanism of degradation of dyes follows the demethylation pathway [530].

Shojaei et al. [531] exploited the sorption capacity of zero-valent iron nanoparticles for the removal of Direct Red 81. The results were analyzed by applying the statistical analysis and the effect of various factors on the removal of the dye was considered. It was found that the highest removal was achieved at weakly acidic pH, because, in the weakly acidic range, the zero-valent iron performs well. Lin et al. [532] prepared Fe nanoparticles by a green in situ synthesis method. The prepared iron nanoparticles were utilized for the concurrent removal of $Pb^{2+}$ and rifampicin and the results showed that removal efficiency of the prepared nanoparticles was obtained to be 100% and 91.6% for $Pb^{2+}$ and rifampicin, respectively. The Fe nanoparticles were prepared to utilize the *Euphorbia cochinchinensis* leaf extract. The polyphenols and caffeine present in the leaf extracts assisted as a reducing agent as well as a capping agent for the prepared Fe nanoparticles thus inhibiting the agglomeration probability. Two possible strategies were build-up for explaining the

simultaneous removal of $Pb^{2+}$ and rifampicin. $Pb^{2+}$ ions tend to sorb onto the surface of the Fe nanoparticles based solely on the sorption activity of the Fe nanoparticles, while the rifampicin interacted positively with the functional groups present on the surface of the nanoparticles.

### 8.2 Normal/p-Block, s-Block Nanomaterials

In addition to the great variety of transition metal-based ZVNMs, those of s- and p-block elements in particular have also been utilized for their applicability as ZVNMs for the removal of contaminants from wastewater bodies. The greater utilization of ZVNMs is because they offer more advantages than the limitations of their use [533]. Lin and Lin [534] designed zero-valent aluminum (ZVAl) nanoparticles via washing of the Al with acids. The finally obtained ZVAl was used for the removal of bromate ions from the water. The removal was partially based on the reduction of bromate to bromide and partial sorption of the bromated ions on the surface of the ZVAl. The results showed complete removal of bromated from 78.1 µmol/L solutions at the optimized operating conditions.

Fu et al. [535] prepared a bimetallic material based on aluminum and iron as (Fe/Al) bimetallic particles for the removal of Cr(VI). The morphological studies showed that in the bimetallic particles, iron was deposited onto the surface of the aluminum. The removal efficiency for Cr(VI) was noted as 93.5%, and it was attributed to the high surface area of the bimetallic nanoparticles. Pouretedal et al. [536] prepared zero-valent tin nanoparticles using a reducing agent and utilized them for the photocatalytic degradation of MB dye. The obtained zero-valent tin (ZVT) nanoparticles presented the highest degradation of > 95% of MB at the optimized conditions of operation. The zero-valent Sn is a strong reducing agent in basic solutions with $E_o = -0.91$ and $-0.93$ V. Furthermore, the most important factor influencing $k_{app}$ is the surface area of the zero-valent metal, which acts as a strong reducing agent in the basic solutions, thereby reducing the MB dye (Table 7).

## 9 Functionalized Metal Hydroxide Nanomaterials

Metal hydroxides can be categorized as strong bases composed of hydroxide ions and the respective metal ions. The metal hydroxides have recently captured the attention of researchers for their exceptionally attractive properties including high conductivity, thermal and mechanical stability, and flammability [560]. Advanced innovation in this respect is the layered double hydroxides, which offer more refined properties including negligible toxicity, high anionic exchange capacity, and pH-dependent solubility, making them a good choice for environmental restoration purposes [561, 562].

Nie et al. [563] designed a photocatalyst by the combination of $Ca(OH)_2$ and peroxymonosulfate (PMS). The prepared $Ca(OH)_2$/PMS catalyst was used for the

**Table 7** Zero-valent metal-based nanomaterial in wastewater remediation

| Nanomaterial | Contaminant | Mechanism | Sorption/ catalytic capacity | Conditions studied | | | Cycles | References |
|---|---|---|---|---|---|---|---|---|
| | | | | pH | Time | Temp °C | | |
| Zero-valent iron/$Fe_3O_4$/Fe(II) system (hZVI) | Molybdate | Sorption | 97% | | 2880 | | | [537] |
| Sulfidated nanoscale zero-valent iron (S-nZVI) | Molybdate | Sorption | 98.2% | 7 | 60 | 25 | | [538] |
| Zero-valent iron combined with petroleum coke (CZVI) | Organic compound | Sorption | 90.9% | 8.5 | 3360 | | | [539] |
| Zero-valent iron ($Fe^0$) supported by activated carbon (NZVI/AC) | Molybdenum (Mo) | Sorption | 90% | 4.5 | 540 | 25 | | [540] |
| Nanoscale zero-valent iron (NZVI) particles | Metronidazole (MNZ) | Sorption | 99% | 5 | 5 | | | [541] |
| Iron-nickel | Tributyl phosphate | Degradation | 100% | | 100 | | | [542] |
| Zero-valent iron nanoparticles (nZVI) | Microcontaminants | Degradation | | | | | | [543] |
| Nanoscale zero-valent iron (nZVI) supported on layered double hydroxide (LDH) composite (LDH@nZVI) | U(VI) | Sorption | 176 mg/g | 5 | 300 | 25 | 6 | [544] |
| Zero-valent iron (ZVI) | Heavy metals | Sorption | Up to 99% | | | | | [545] |
| Nanoscale zero-valent iron nanoparticles (nZVI) | Plutonium | | 77% | 6 | 240 | | | [546] |
| | Uranium | | 99% | | | | | |
| Zero-valent iron nanoparticle (nZVI) | Citric acid | Degradation | Upto 90% | | 120 | | | [547] |
| | Tartaric acid | | | | | | | |
| | Oxalic acid | | | | | | | |
| Nanoscale zero-valent iron composite (AT-nZVI) | Cr(VI) | Sorption | 90.6% | | 840 | | | [548] |
| Nanosized zero-valent iron (nZVI) | $Co^{2+}$ | Sorption | 172 mg/g | | 1440 | | 8 | [549] |
| Nanoscale zero-valent iron (SBC-nZVI) | Cr(VI) | Sorption | 100% | 3 | 180 | | | [550] |

**Table 7** (continued)

| Nanomaterial | Contaminant | Mechanism | Sorption/ catalytic capacity | Conditions studied | | | Cycles | References |
|---|---|---|---|---|---|---|---|---|
| | | | | pH | Time | Temp °C | | |
| ZVI-based Fenton oxidation processes (ZVI-ZVI/$H_2O_2$) | 2,4-dinitroanisole (DNAN) | Degradation | 81.3 ± 3.6% | 7.2 | 360 | | | [551] |
| | 2,4-dinitrophenol (DNP) | | 80.6 ± 1.8% | | | | | |
| | 2,4-dinitrochlorobenzene (DNCB) | | 90.9 ± 3.5% | | | | | |
| Nanoscale zero-valent copper (nZVC) | Azo dyes | Photocatalytic degradation | Up to 90% | | 240 | | | [552] |
| Zero-valent copper (ZVC) | Diethyl phthalate (DEP) | Degradation | 120 | 2.5 | | | | [553] |
| Zero-valent copper-catalyzed peroxymonosulfate system | Naproxen | Degradation | Up to 100% | 3–7 | 10 | 25 | | [554] |
| | Bisphenol S | | | | | | | |
| | Ibuprofen | | | | | | | |
| Ozone assisted with Cu(0) | Aniline | Degradation | 98% | | 24 | | | [555] |
| Zero-valent copper nanoparticles (nZVC) | Reactive blue 4 | Photocatalytic degradation | 90% | | 15 | 25 | | [556] |
| Zero-valent copper (ZVC)/$O_2$/STPP system | p-nitrophenol (PNP) | Photocatalytic degradation | 100% | 8.1 | 120 | | | [557] |
| Zero-valent aluminum (ZVAl)–acid system | Bisphenol A (BPA) | Photocatalytic degradation | 75% | 1.5 | 720 | | | [558] |
| Zero-valent aluminum | Cr(VI) | Photocatalytic degradation | 80% | | | 45 | 5 | [559] |

photocatalytic degradation of bisphenol A and phosphate ions simultaneously. The proposed pathway given for the removal of BPA and P showed that superoxide radical ($O_2^{-}$) and singlet oxygen ($^1O_2$) rather than sulfate ($SO_4^{\bullet -}$) or hydroxyl ($HO^{\bullet}$) were the predominant ROS responsible for the degradation of contaminants. The results showed 89.5% BPA and 98.9% P degradation.

Lee et al. [564] developed rice husk (RH)-derived biochar functionalized with Mg/Al-calcined layered double hydroxides (RHB/MgAl-CLDHs) via the co-pyrolysis of MgAl-LDH preloaded RH. The designed RHB/MgAl-CLDHs were used as a sorbent for the successful removal of phosphate from an aqueous solution. The results showed phosphate removal efficiency of up to 97.6% by the prepared sorbent. The obtained results were achieved with the pseudo-second-order model and Sips model, respectively, revealing chemisorption. Koilraj et al. [565] attempted to prepare arginine/lysine-functionalized MgAl LDHs through a one-pot synthesis strategy. The prepared material was used as a sorbent for the removal of $Co^{2+}$ ions. The results presented the highest sorption capacity of 1.159 and 1.170 mmol/g for the LDHs functionalized with lysine and arginine, respectively. The $Co^{2+}$ ions sorption was justified based on the fact that the amino functionalization of the layered double hydroxides tends to form a chelation complex, thereby enhancing the ability for take-up of $Co^{2+}$ ions. The fact that $Co^{2+}$ ions form diamine-like coordination increases its sorption capacity compared with other metal ions. Sadeghalvad et al. [566] tailored a sorbent by loading metal double hydroxides onto the surface of waste rock of iron ore mine (metasomatic rocks) for the removal of sulfate ions. The mechanistic studies confirmed the monolayered chemisorption with the combination of the film-mass transfer and internal diffusion. The maximum sorption capacity obtained was 41.43 and 53.07 mg/g for Mg–Al and Ni–Al metasomatic, respectively (Table 8).

## 10 Functionalized Silsesquioxane-Based (Silica-Based) Nanomaterials as Sorbents for Contaminant Removal

Other NMs worth mentioning are silica-based NMs (SNMs), also termed silsesquioxane-based NMs with respect to the siloxane rings incorporated in the framework of the NMs. SNMs are obtained by applying high temperature to the silica, accumulating the siloxane rings in the multiple-structured NMs [590]. These NMs are used in various fields due to their extraordinary properties including cytotoxicity, high porosity, high mechanical strength, cost-effectiveness, and biocompatibility [591]. The fabrication of SNMs with additional functionalities resulting in one-, two-, and three-dimensional structures governs its mechanical strength, enhancing the activity of the FSNMs.

Araghi and Entezari [592] designed amino-functionalized silica magnetite nanoparticles (A-S-MNPs) by the coating of sono-synthesized magnetite nanoparticles (MNPs) in a basic medium by $SiO_2$. The obtained silica MNPs were then further modified with 3-aminpropyltriethoxysilane (APTES). The estimated particle size of the prepared nanocomposite was 25 nm. The prepared material was then used for the sorptive removal of Reactive Black 5 (RB5) and sodium dodecylbenzenesulfonate (SDBS). The results showed sorption efficiency of 83.33 and 62.5 mg/g for

**Table 8** Metal hydroxide-based nanomaterial in wastewater remediation

| Nanomaterial | Contaminant | Mechanism | Sorption/catalytic capacity | Conditions studied | | | Cycles | References |
|---|---|---|---|---|---|---|---|---|
| | | | | pH | Time | Temp °C | | |
| Mg/Fe layered double hydroxide loaded with Magnetic($Fe_3O_4$) carbon spheres (MCs@Mg/Fe-LDHs) | Pb(II) | Sorption | 3.66 mmol/g | 7 | 3000 | 25 | 3 | [567] |
| | Cu(II) | | 5.33 mmol/g | | | | | |
| Ferric hydroxide/graphene oxide | Arsenate | Sorption | 95% | 4 | | | | [568] |
| Aluminum hydroxide–coated nanoscale zero-valent iron (NZVI@$Al(OH)_3$) | 4-nitrophenol (4-NP) | Sorption | 96.3% | 8.3 | 10 | 24 | | [569] |
| Surfactant-coated aluminum hydroxide [surfactant-$Al(OH)_3$] | Sodium dodecyl sulfate (SDS) | Degradation | Up to 99% | 7 | | 25 | | [570] |
| | Sodium bis(2-ethylhexyl)sulfosuccinate (AOT) | | | | | | | |
| | Sodium oleate | | | | | | | |
| Aluminum hydroxides | Herbicide 2-(2,4-dichlorophenoxy) propanoic acid (2,4-DP) | Sorption | 93% | 7 | 240 | 30 | | [571] |
| Chitosan/$Al(OH)_3$·(CS/$Al(OH)_3$) | Fluoride | Sorption | Up to 80% | 4 | 90 | | | [572] |
| Aluminum hydroxide | Fluoride | Sorption | 95% | | | | | [573] |
| Calcite sludge-aluminum hydroxide(CAl) | Bisphenol A | Sorption | 83.53 mg/g | 3 | | | 5 | [574] |
| | Ibuprofen | | 34.96 mg/g | | | | | |
| Aluminum hydroxide gel-coated nanoscale zero-valent iron (AHG@NZVI) | Tetracycline (TC) | Sorption | 98.1% | 6.5 | 70 | 25 | | [575] |
| Calcium hydroxide | Polychlorinated biphenyls (PCBs) | Sorption | 94% | | | 600 | | [576] |
| Calcium hydroxide | Hydrogen chloride | | | | | | | [577] |
| Calcium hydroxide nanorods (CHN) | Fluoride | Sorption | 450 ± 10 mg/g | 6.5 | 45 | | | [578] |
| Calcium hydroxide-coated dairy manure-derived biochar (Ca-BC) | Phosphate | Sorption | 95% | 8.5 | 4320 | | | [579] |
| Calcium hydroxide | Lignin | Sorption | 70% | 5 | 10 | 25 | | [580] |

**Table 8** (continued)

| Nanomaterial | Contaminant | Mechanism | Sorption/catalytic capacity | Conditions studied | | | Cycles | References |
|---|---|---|---|---|---|---|---|---|
| | | | | pH | Time | Temp °C | | |
| Granular activated carbon-supported magnesium hydroxide (Mg-GAC) | Cd(II) | Sorption | 3.47 mg/g | 6 | 480 | 25 | | [581] |
| Modified bentonite with magnesium hydroxide $Mg(OH)_2$ | Phosphate | Sorption | > 54% | 7 | 45 | 120 | | [582] |
| $Mg(OH)_2$ | Fluoride | Sorption | | 5 | | | | [583] |
| $Mg(OH)_2$ & $Ba(OH)_2$ | Metals | Sorption | | | | | | [584] |
| NZVI surface coated with $Mg(OH)_2$ shell (NZVI@$Mg(OH)_2$) | Cr(VI) | Sorption | 97.8% | 7.5 | | | | [585] |
| $Mg(OH)_2$ | Phosphorus | Sorption | 588.4 mg/g | | | | | [586] |
| Magnesium hydroxide | Oil | Sorption | 10959 mg/g | | | 25 | 5 | [587] |
| Lignin-$Mg(OH)_2$ nanocomposite | $Ni^{2+}$ | Sorption | Up to 100% | | 1500 | | | [588] |
| | $Cd^{2+}$ | | | | | | | |
| | $Pb^{2+}$ | | | | | | | |
| Cellulose acetate/Mg–Al layered double hydroxide (Mg–Al LDH) nanocomposite membranes | Diclofenac sodium (DS)<br>Tetracycline (TC) | Sorption | Up to 100% | | | | | [589] |

RB5 and SDBS, respectively. Mahmudi et al. [593] prepared dendritic fibrous nanosilica-grafted d-penicillamine. The prepared dPA-DFNS-$NH_2$ had a surface area of 78.2$m^2$/g, pore volume of 0.13$cm^3$/g, and average pore size of 6.7 nm. The prepared material was used as an efficient sorbent for the removal of heavy metals $Co^{2+}$, $Ni^{2+}$, $Ag^{+}$, and $Pb^{2+}$from water samples, with complete removal efficiency. Wang et al. [594] prepared silica nanotubes through an electrospinning and calcination process followed by their modification by sym-diphenylcarbazide (SD-SNTs). The prepared composite was used as an effective sorbent for the removal of Pb(II). The surface functionalization conspicuously enhanced the sorptive efficiency of the material due to the increased possibility for chelation between the imino groups and lead ions (Table 9).

## 11 Quantum Dots, a New-Fashioned Approach for Utilizing Nanomaterials in Wastewater Contamination

Quantum dots (QDs) can be described as semiconductor nanoparticles having size- and composition-dependent electronic and optical properties (optoelectronic properties). The quantum dots are manmade nanoscale crystals that have the tendency to transport electrons [611]. The QDs, nanoparticles of semiconductor materials, are ultra-small, with a size range of 1.5–10 nm. When the size of semiconductors is this small, quantum effects are initiated, limiting the energies at which the electrons and holes (in the absence of $e^{-}$) can exist in particles. As there is a relationship between energy and wavelength, the optical properties of the particle can be tuned depending on its size [612, 613]. Thus the particles can emit or absorb certain wavelengths of light by controlling their size. QDs have been found to possess unique properties including high extinction coefficient and brightness, photo-stability, size-dependent optical properties, and large Stokes shift. Based on the unique chemistry and properties of QDs, they have been used extensively in the fields of electronics, catalysis, medicine, imaging, sensing, and information storage, among others [614]. In this section of the paper, we will discuss QDs of different materials and their applicability with respect to environmental remediation.

### 11.1 Graphene QDs

Graphene QDs can be described as small fragments of graphene in which electronic transport is observed in all three spatial dimensions. Graphene semiconductor material has a zero bandgap and possesses an infinite exciton Bohr diameter. The confinement can be seen in any of the fragments, but the GQDs possess dimensions in the size range below 20 nm [615]. The GQDs are usually prepared by the cutting or fragmentation of the graphene sheets through the top-down approach. The most attractive properties of the GQDs include their abundant presence, low toxicity, solubility in a variety of solvents, and capacity for further functionalization. These properties enhance the applicability of the GQDs in various fields [616]. Kaur et al. [617] prepared nitrogen-doped graphene quantum dots through a cost-effective

**Table 9** Silica-based nanomaterials in wastewater remediation

| Nanomaterial | Contaminant | Mechanism | Sorption/catalytic capacity | Conditions studied | | | Cycles | References |
|---|---|---|---|---|---|---|---|---|
| | | | | pH | Time | Temp °C | | |
| Mesoporous silica | $Co^{2+}$ | Sorption | 89% | 7 | 480 | | | [595] |
| Silica coated β-cyclodextrin polymeric adsorbent | 17β-estradiol | Sorption | 90% | 6.1–6.8 | 2880 | | 4 | [596] |
| Magnetic silica microrods (R-$Fe_3O_4$@$SiO_2$) | Cu(II) | Sorption | 322.58 mg/g | | 30 | | | [597] |
| | Pb(II) | | 346.02 mg/g | | | | | |
| | Cr(III) | | 384.62 mg/g | | | | | |
| | Zn(II) | | 308.64 mg/g | | | | | |
| | Co(II) | | 316.46 mg/g | | | | | |
| Ordered mesoporous silica (OMS) incorporated polyvinylidene fluoride (PVDF) | Methylene blue | Sorption | 14.5 mg/g | | | | 5 | [598] |
| | Cu(II) | | 1.5 mg/g | | | | | |
| Corn cob silica-alginate beads | Phenol | Sorption | 93% | | 5760 | | | [599] |
| CuO/$ZrO_2$–MCM-41 (CuO@ZM-41) | $Cr^{6+}$ | Photocatalytic degradation | 100% | | 30 | | | [600] |
| Iron-incorporated mesoporous silica | Tetracycline | Sorption | 155.76 mg/g | 5–7 | 800 | 25 | | [601] |
| Amino-functionalized SBA-15-$NH_2$ ordered mesoporous silica (OMS) materials | Ampicillin | Sorption | 333 mg/g | 7.4 | 1500 | 25 | | [602] |
| Silica ($SiO_2$)-decorated carbon nanotubes (CNTs) sponge | Oil | Sorption | 100% | | | | 10 | [603] |
| Mesoporous silica (AMS) | Cd(II) | Sorption | 11.54 mg/g | 5 | | | 5 | [604] |
| | Pb(II) | | 8.59 mg/g | | | | | |
| Diamine-functionalized mesoporous silica on multi-walled carbon nanotubes (NN-m$SiO_2$@MWCNTs) | Cu(II) | Sorption | 66.57 mg/g | 6.2 | | 25 | | [605] |
| All-silica zeolite beta | Perfluorinated compounds | Sorption | | | | | | [606] |
| 3D organized mesoporous silica (OMS) | As(V) | Sorption | 55 mg/g | 5 | | | | [607] |
| Silica gel | Polychlorinated diphenyl sulfides (PCDPSs) | Degradation | 75.6% | 11 | | | | [608] |

**Table 9** (continued)

| Nanomaterial | Contaminant | Mechanism | Sorption/ catalytic capacity | Conditions studied | | | Cycles | References |
|---|---|---|---|---|---|---|---|---|
| | | | | pH | Time | Temp °C | | |
| Silica gel modified with p-toluidine formaldehyde resin | Cr(VI) | Sorption | 43.47 mg/g | 1 | 300 | 50 | | [609] |
| Silica mesoporous materials of MCM-48 type | Safranin dye | Sorption | 62.5 mg/g | | | | | [610] |

thermal pyrolysis process [618]. The N-GQDs exhibited excellent fluorescence with a maximum fluorescence at 440 nm. The prepared chemosensor was analyzed for its selectivity towards the analyte of interest (TNT) by treating it with a mixture of nitro-substituted phenols, metal ions, and other aromatics. The results showed that the fluorescence spectrum of the N-GQDs was greatly quenched as trinitrotoluene was added to the system, while the rest of the aromatics had little or no effect at all on the fluorescence spectrum. These results confirmed the specificity and the sensitivity of the prepared QDs for the detection of TNT. The mechanistic pathway for the quenching between N-GQDs and TNT was explained based on the fact that a spectral overlap was developed between the emission spectrum of N-GQDs and the absorption spectrum of TNT, according to the fluorescence resonance energy transfer (FRET) mechanism, leading to quenching. Another possibility is that an electrostatic interactive force was developed between the OH end of TNT, $NH_2$-group, and pyridinic nitrogen of the N-GQDs, eventually resulting in quenching [619]. The excessive presence of TNT led to a redshift in the emission peak due to the high acidity of TNT relative to other contaminants, leading to the formation of a non-fluorescent complex, thus resulting in quenching [620]. These prepared N-GQDs were used as a probe sensor for the detection of an explosive, trinitrotoluene (TNT), and showed excellent efficiency.

Qu et al. [621] also prepared a composite of $TiO_2$ nanotubes decorated with graphene quantum dots (GQDs/$TiO_2$ NT composites) that exhibits greater photoluminescence quantum yield, leading to excellent optical properties and thus making it a useful photocatalyst. The prepared photocatalyst was used for exploiting its photocatalytic activity for the degradation of MO dye under a UV–Vis irradiation source. The greatest efficiency of 94.64% in 20 min was obtained, which was attributed to the broadened visible light absorption and enhanced photocatalytic activity of the prepared composite. The mechanism for the degradation of MO was explained by the fact that incorporation of GQDs with $TiO_2$ led to enhanced absorption ability of $TiO_2$ in the visible range, due to the π-state combination of the GQDs and the CB of $TiO_2$. Upon photogeneration of electrons from the $TiO_2$, the GQDs come forward to capture these electrons, ensuring the separation of $e^-/h^+$ pairs [622]. The up-conversion photoluminescence properties of GQDs cause the conversion of longer irradiation wavelength into a shorter one, and the presence of oxygen on the surface of GQDs captures electrons and oxygen radicals, which then eventually cause the oxidation of MO dye. In addition, holes on the surface of $TiO_2$ cause the production of hydroxyl radicals, which completes the degradation of MO into simpler compounds [623].

### 11.2 Carbon QDs

Another huge class of QDs is carbon quantum dots (CQDs) or fluorescent carbon nanoparticles. CQDs generally exist in quasi-spherical nanoparticle form. They consist of an amorphous to nanocrystalline core of graphitic or turbostratic carbon ($sp^2$ carbon) [624]. Another possibility is the presence of graphene and graphene oxide sheets fused together by diamond-like $sp^3$-hybridized carbon insertions. The

oxidized form of CQDs contains many carboxyl moieties on its surface. The carboxyl moieties may impart a solubility factor to the CQDs and also provide suitable chemically reactive groups which help in further functionalization and surface passivation. Surface passivation using groups such as inorganic, organic, or polymer materials will further enhance the fluorescence properties and solubility of the CQDs [625]. Saud et al. [626] prepared carbon quantum dot/titanium dioxide nanocomposite (CQD/$TiO_2$) nanofibers by a hydrothermal method [627]. The prepared nanocomposite was utilized to evaluate its efficiency for the photocatalytic degradation of MB under visible light irradiation and antibacterial activity against *Escherichia coli.* $TiO_2$ is known to have excellent photocatalytic properties under UV-irradiation, and the incorporation of CQDs will enhance its photocatalytic efficiency by decreasing the wavelength, promoting the production of electrons in a wider range of visible irradiation. The CQDs act as a sink for capturing the produced electrons and their mobilization. The CQD/$TiO_2$exhibited complete degradation of the MB dye in 20 min with an additional property of the reusability of the photocatalyst for up to three cycles. The efficiency was slightly reduced for the third run due to the covering of the active sites of the catalyst, hence minimizing their availability for the photocatalytic operation.

Muthulingam et al. [628] prepared carbon quantum dots/nitrogen-doped ZnO composites by a simple one-step method, which were utilized for the photocatalytic degradation of commercial dyes including malachite green, MB, and fluorescein. The obtained results showed that the CQD/N-ZnO photocatalyst exhibited 100% removal efficiency for the malachite green in 30 min irradiation under visible light (Fig. 15). For MB, it took 45 min to completely degrade the dye, while in the case

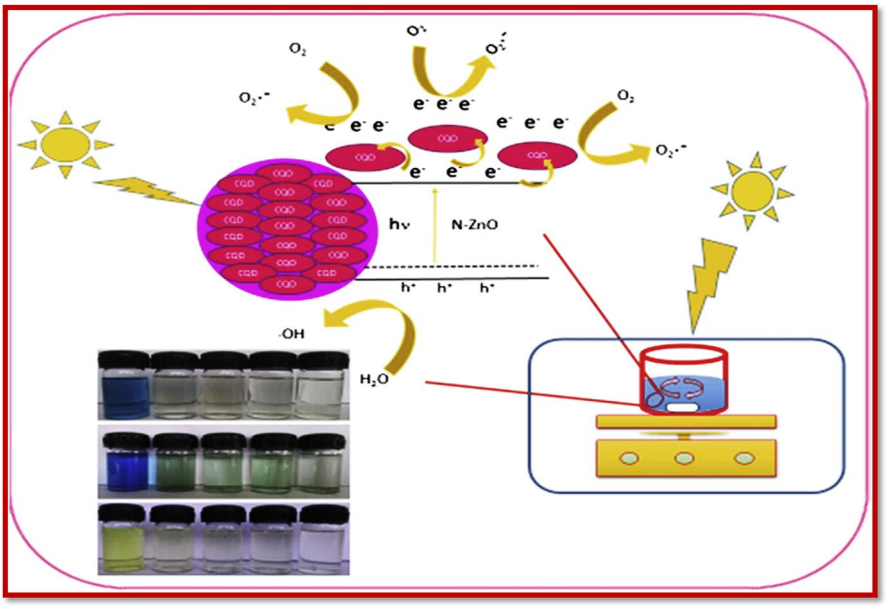


**Fig. 15** Schematic explanation, experimental setup, and mechanism of CQD/N-ZnO on dyes under natural daylight irradiation. Reproduced with permission [628], Copyright 2015, Elsevier

of fluorescein, 95% was obtained in 15 min of daylight exposure. The excellent degradation efficiency exhibited by CQD/N-ZnO was attributed to the combined features of the CQDs and ZnO, and inhibition of the recombination of photogenerated electron/hole pairs due to the CQD and nitrogen doping of the ZnO [629]. Once the energy equal to or higher than the bandgap of the photocatalyst is achieved, the photogeneration of electron/hole pairs indicates the beginning of the process. The π-electronic interaction of the carbon with the CB of the ZnO photocatalyst leads to the up-converting property of the QDs, leading to the high absorption of light in a wider wavelength range. A larger number of holes created near the VB of the ZnO may cause the production of radicals, eventually leading to maximal degradation efficiency. The electrons trapped in the CQDs initiate the production of superoxide radicals, while the combination of holes with water molecules tends to produce hydroxyl radicals. These powerful radicals lead to a combinational approach towards the degradation of dye into simpler and less toxic compounds [630].

### 11.3 Metal Oxide QDs

Many metal oxide-based quantum dots have been prepared to date to take advantage of their useful properties including optical activity, stability, and conductivity. One significant example is titanium oxide QDs. $TiO_2$ has been widely studied since the discovery of its photocatalytic water-splitting ability, owing to its desirable properties such as nonhazardous nature, stability, ease of availability, wider bandgap($E_{bg}$ = 3.2 eV for anatase phase), and cost-effectiveness [631]. Gnanasekaranet al. [632] prepared $TiO_2$ quantum dots by the sol–gel method [633], and the efficiency of the prepared material was checked by photocatalytic degradation of MO and MB. The bandgap obtained for the prepared $TiO_2$ QDs was 3.79 eV in the UV region. Degradation efficiency of 97% was obtained for both MO and MB in 80 min. The UV light irradiation to the mixture of dye and photocatalyst produces electrons in the CB and in the VB of the photocatalyst. The electrons react with oxygen, producing(oxidation) radicals, while the holes react with water(reduction) producing radicals [634]. The combined radicals cause the degradation of dyes into simpler nontoxic compounds completing the process. Kaur et al. [635] prepared a composite of $Ag_2O/TiO_2$ quantum dots (QDs)thus enhancing the photocatalytic efficiency of the bare $TiO_2$ QDs. The prepared QDs had a spherical shape with a size of 2–9 nm. The prepared photocatalyst was utilized for the degradation of the fluoroquinolone levofloxacin drug. The excellent photocatalytic efficiency is attributed to the separation of the produced electron/hole pairs due to the enhanced light absorption property due to the incorporation of $Ag_2O$ with $TiO_2$ QDs. The results showed 81% removal of levofloxacin drug utilizing the QDs in 90 min. The removal efficiency was attained based on the sorption as well as the photocatalytic activity of the QDs. The main photocatalytic species involved are the holes, electrons, $^1O_2$, and $^{\cdot}OH$. Soodet al. [636] also prepared $TiO_2$ quantum dots using the sol–gel method [633] and performed photocatalytic degradation of indigo carmine dye. The unique characteristics properties of $TiO_2$ led to the maximum degradation of the said dye making it an attractive process for the removal of the contaminants. The results

indicated that 95% of dye degradation was obtained in 60 min of the photocatalytic process in acidic pH at 25 °C (Table 10).

### 11.4 Metal Sulfide QDs

Metal sulfides constitute a distinct class of quantum dots. Upgraded metal sulfide QDs have proved to be more effective in their respective activity based on their advanced properties than their simple sums. Rajabi et al. [637] performed a comparative study to evaluate the photocatalytic efficiency of functionalized ZnS QDs and iron oxide ($Fe_3O_4$) MNPs for the removal of Victoria blue R dye. Both photocatalysts were prepared by a simple chemical precipitation method, while the surface modification was performed using 2-mercaptoethanol and sodium dodecyl sulfate. The particle size calculated for the ZnS QDs and the MNPs was 1–3 nm and 50–80 nm, respectively. The results obtained showed 95% and 65% removal efficiency for MNPs and QDs, respectively. Zinc sulfide quantum dots doped with Fe(III) were prepared for the removal of methyl violet [638]. The bandgap calculated for the prepared photocatalyst was > 4.58. About 98.8% decolorization was obtained using the prepared photocatalyst, showing the extraordinary activity of the doped photocatalyst.

## 12 Miscellaneous Functionalized Nanomaterials

Apart from the FNMs discussed above, several other NMs have demonstrated attractive properties, such as dendrimers [697], nanoclays [698], ceramics [699], and mesoporous materials [700]. Sohail et al. [701] studied the preparation of polyamidoamine (PAMAM) dendrimers for the removal of nickel ions. Dendrimers have special qualities including radial symmetry and homogeneity, having a monodisperse and well-defined structure, with tree-like branches characterized by terminal poly-functionality. The dendrimers were synthesized using the divergent method, by initiating at the core, leading towards the periphery following two basic operations. The first one is the coupling of the monomer, while in the second step the de-protection/transformation of the monomer end group occurs. It creates a new reactive surface functionality that couples a new monomer in a similar way as that of the solid-phase synthesis of peptides or oligonucleotides. A particle size of 827 nm was found for the prepared zero-generation dendrimer, and the sorption capacity for the prepared material was 98.6 mg/g.

Hayati et al. [702] studied the efficiency of a poly(propylene imine) (PPI) dendrimer against the decantation of Direct Red 80 (DR80) and Acid Green 25 (AG25) dyes. Maximum removal efficiency was obtained for the removal of both dyes. Analysis of the data showed that the sorption results best fitted the Langmuir isotherm, which predicts the monolayer sorption of the dyes onto the dendrimer surface.

Almasri et al. [703] studied the preparation of hydroxyl iron-modified montmorillonite (HyFe-MMT) nanoclay through the wet chemical synthesis method. The prepared HyFe-MMT nanoclay was used for the removal of arsenite(III). The

**Table 10** Quantum dot-based nanomaterial in wastewater remediation

| Nanomaterial | Contaminant | Mechanism | Sorption/catalytic capacity | Conditions studied | | | Cycles | References |
|---|---|---|---|---|---|---|---|---|
| | | | | pH | Time | Temp °C | | |
| Carbon quantum dots and reduced graphene oxide layers-modified S@g-$C_3N_4$/B@g-$C_3N_4$ (CRSB) photocatalyst | Chloramphenicol | Photocatalytic degradation | 92.4% | 6 | 120 | 30 | 5 | [639] |
| Graphene quantum dots-ZnO nanocomposites | Methylene blue | Photocatalytic degradation | | | 180 | | | [640] |
| | Methyl orange | | | | | | | |
| Nitrogen-doped carbon quantum dots modified with g-$C_3N_4$ NCDs/DCN | Ofloxacin | Photocatalytic degradation | 75.2% | 3.5–7.5 | 120 | | | [641] |
| | Bisphenol A | | 47.4% | | | | | |
| | Ciprofloxacin | | 75.8% | | | | | |
| | Cr(VI) | | 92.6% | | | | | |
| Sulfur-doped carbon quantum dots (S-CQDs)/hollow tubular g-$C_3N_4$ photocatalyst (HTCN-C) | Tetracycline | Photocatalytic degradation | 82.67% | | 40 | | 5 | [642] |
| BiOBr/CDs/g-$C_3N_4$ composites | Tetracycline | Photocatalytic degradation | 82.7% | | 60 | | 10 | [643] |
| | Ciprofloxacin | | 81.3% | | | | | |
| Nitrogen-doped CDs/g-$C_3N_4$ (NCDs) | Indomethacin | Photocatalytic degradation | 91% | | 90 | | 6 | [644] |
| Carbon quantum dots with polydopamine (PDA/CQDs) | Methylene blue | Photocatalytic degradation | | | | | | [645] |
| | Orange II | | | | | | | |
| Graphitic carbon nitride nanorods decorated with graphene quantum dots (GQDs/g-CNNR) | Oxytetracycline | Photocatalytic degradation | 80% | | 120 | | 5 | [646] |
| ZnO sensitized by carbon quantum dots (L-CQDs/ZnO) | Phenol | Photocatalytic degradation | 100% | | 330 | | 10 | [647] |
| $SnO_2$ quantum dots decorated on 2-D material g-$C_3N_4$ | Rhodamine B | Photocatalytic degradation | 95% | | 60 | | | [648] |

**Table 10** (continued)

| Nanomaterial | Contaminant | Mechanism | Sorption/ catalytic capacity | Conditions studied | | | Cycles | References |
|---|---|---|---|---|---|---|---|---|
| | | | | pH | Time | Temp °C | | |
| $SnS_2$ modified with nitrogen-doped carbon quantum dots (N-CQDs/$SnS_2$ Composite) | Cr(VI) | Photocatalytic degradation | 100% | | 25 | | 6 | [649] |
| $MnO_x$ quantum dots dispersed on N-doped porous carbon shells (denoted as $MnO_x$/N-HPCS) | Bisphenol A | Photocatalytic degradation | 99% | | 20 | 25 | 4 | [650] |
| Phenylhydrazine-modified carbon quantum dots | Methylene blue | Photocatalytic degradation | 94.3% | | 60 | | | [651] |
| CDs-N-$TiO_{2-x}$ nanocomposite | Cr(VI) | Photocatalytic degradation | 94% | 5.36 | 60 | | | [652] |
| PVA/CQDs | Methylene blue | Sorption | 97% | 12 | 40 | | 5 | [653] |
| Nitrogen-doped carbon quantum dots with g-$C_3N_4$ (NCQD/g-$C_3N_4$) | Methylene blue | Photocatalytic degradation | 91.2% | | 180 | | 3 | [654] |
| Nitrogen-doped graphene quantum dots | Methylene blue | Photocatalytic degradation | 93% | | 60 | | | [655] |
| α-$Bi_2O_3$/C-dots | Indigo carmine | Photocatalytic degradation | 86% | 6 | 120 | | 3 | [656] |
| | Levofloxacin | | 79% | | | | | |
| Nitrogen-sulfur-doped carbon quantum dots N,S-CQDs/$TiO_2$ nanocomposite | Diclofenac | Photocatalytic degradation | 62.3% | | 120 | | | [657] |
| Carbon quantum dots modified with graphitic carbon nitride | Carbamazepine | Photocatalytic degradation | 100% | 7 | 60 | 25 | 4 | [658] |
| Biomass-derived carbon quantum dots | Methylene blue | Photocatalytic degradation | 99.5% | | 130 | | | [659] |
| $SnO_2$ quantum dot encapsulated carbon nano-flake ($SnO_2$–CNF) | Bisphenol A | Photocatalytic degradation | 98% | 6 | 60 | | 3 | [660] |
| Ag-doped $SnO_2$ quantum dots | Rhodamine B | Photocatalytic degradation | 97.5% | | 120 | | 7 | [661] |
| Bismuth (Bi)-doped tin oxide ($SnO_2$) quantum dots | Rhodamine B | Photocatalytic degradation | 98.2% | | 100 | | 5 | [662] |
| | Ciprofloxacin hydrochloride | | 92.13% | | 90 | | | |

**Table 10** (continued)

| Nanomaterial | Contaminant | Mechanism | Sorption/ catalytic capacity | Conditions studied | | | Cycles | References |
|---|---|---|---|---|---|---|---|---|
| | | | | pH | Time | Temp °C | | |
| $NiFe_2O_4$/SQD | Rhodamine B | Photocatalytic degradation | 98% | | 105 | | | [663] |
| Carbon quantum dots implanted CdSnanosheets (CQD/CdS-NSs) | Cr(VI) | Photocatalytic degradation | 94% | | 10 | | 3 | [664] |
| $SnO_2$ quantum dot/gold (SQD/Au) nanocomposites | Methylene blue | Photocatalytic degradation | 99% | | 150 | | 3 | [665] |
| | Rhodamine B | | 99% | | 200 | | | |
| | Methyl orange | | 93.5% | | 180 | | | |
| $C_3N_4$/AgI/ZnO/CQDs (PGCN) | 2,4-Dinitrophenol | Photocatalytic degradation | 98% | | 120 | | 10 | [666] |
| Ternary carbon quantum dots (CDs)/$Bi_2MoO_6$ (BMO)/graphitic carbon nanofibers (GNFs) composites (CDs/BMO/GNFs) | Rhodamine B | Photocatalytic degradation | 99.4% | | 70 | | | [667] |
| $CeO_2$ QDs/BiOX (X = Cl, Br) heterojunctions | Tetracycline | Photocatalytic degradation | 97% | | 120 | | 6 | [668] |
| | Cr(VI) | | | | | | | |
| Ag-$SnO_2$ quantum dots(QDs)/silver phosphate (AgSn/AgP) composites | Carbamazepine | Photocatalytic degradation | 63.6% | | 120 | | 3 | [669] |
| Mn-doped ZnS quantum dots capped by L-cysteine (Mn@ZnS/L-cyst) | 4′,5′-Dibromofluorescein dye | Photocatalytic degradation | 97% | 5.5 | 30 | | | [670] |
| Carbon quantum dots modified with chitosan (CH-CQDs) | $Cd^{2+}$ | Sorption | 112.4 mg/g | 8 | 30 | 25 | | [671] |
| Amine-functionalized graphene quantum dots | Methyl orange | Photocatalytic degradation | 99% | | 120 | | 4 | [672] |
| Graphene quantum dots with silver NPs (GQDs/Ag NPs) | Rhodamine B | Photocatalytic degradation | | | 540 | | | [673] |
| Black $TiO_{2-x}$/N-doped graphene quantum dots (BTNG) | Rhodamine B | Photocatalytic degradation | 100% | | 30 | | | [674] |

**Table 10** (continued)

| Nanomaterial | Contaminant | Mechanism | Sorption/ catalytic capacity | Conditions studied | | | Cycles | References |
|---|---|---|---|---|---|---|---|---|
| | | | | pH | Time | Temp °C | | |
| Nitrogen-doped graphene quantum dots (NGQDs)-$BiVO_4$/g-$C_3N_4$ Z-scheme heterojunction | Tetracycline | Photocatalytic degradation | 91.5% | | 30 | | 4 | [675] |
| Carbon quantum dots/CdS quantum dots/g-C3N4 (CDs/CdS/GCN) photocatalysts | 4-Nitrophenol | Photocatalytic degradation | 95% | | 120 | | 4 | [676] |
| p-type phosphorus-doped graphene quantum dots (P-GQDs) | Methyl orange | Photocatalytic degradation | 95.5% | | 14 | | | [677] |
| N-doped graphene quantum dots (NGQDs) | Methylene blue | Photocatalytic degradation | 98% | | 150 | | | [678] |
| Bi(III) containing oxides with quantum dots (QDs) | $Cl^-$ removal in leachate | | 66.1% | 1 | 480 | | | [679] |
| Carbon quantum dots modified potassium titanate nanotubes (CQDs/$K_2Ti_6O_{13}$) composite | Amoxicillin | Photocatalytic degradation | 100% | 6 | 90 | 25 | | [680] |
| Nitrogen–phosphorus-doped fluorescent carbon dots (NP-CD) | Cr(VI) | Photocatalytic degradation | 100% | | 110 | | | [681] |
| N-doped carbon quantum dots/$TiO_2$ (NCQDs/$TiO_2$) | Methylene blue | Photocatalytic degradation | 86.9% | | 420 | | | [682] |
| ZnS quantum dots | Methyl violet | Photocatalytic degradation | 95% | 12 | 120 | | | [683] |
| Zinc oxide quantum dots/CuO NSs | Tetanus toxin | Photocatalytic degradation | Up to 90% | | | 25 | | [684] |
| (CdS–CdSe)/$TiO_2$-NTAs | Methyl orange | Photocatalytic degradation | 95.1 | | 120 | | 3 | [685] |
| ZnS quantum dots impregnated-mesoporous $TiO_2$ nanospheres | Methylene blue | Photocatalytic degradation | 100% | | 32 | | | [686] |
| CdTeSe Quantum Dots (QDs) | Rhodamine B | | 61% | 12 | 1440 | | | [687] |

**Table 10** (continued)

| Nanomaterial | Contaminant | Mechanism | Sorption/ catalytic capacity | Conditions studied | | | Cycles | References |
|---|---|---|---|---|---|---|---|---|
| | | | | pH | Time | Temp °C | | |
| Graphene quantum dots (GQDs) infilled titanium dioxide ($TiO_2$) nanotube arrays (NTAs) hybrid | Methylene blue | Photocatalytic degradation | 99.8% | | 180 | | 10 | [688] |
| Cadmium selenide/graphene quantum dots (CdSe/GQDs) | Methylene blue | Sonocatalytic degradation | 99% | 9 | 90 | | 5 | [689] |
| Graphene quantum dots | Oxamyl | Sorption | 125 mg/g | 8 | 25 | 20 | | [690] |
| N-doped reduced graphene quantum dots | Rhodamine B | Sorption | 24.62 mg/g | 7 | 720 | | | [691] |
| $Fe_3O_4$/hydroxyapatite/graphene quantum dots ($Fe_3O_4$/HAP/GQDs) | Methyl orange | ICP-AES | 37.99 mg/g | | | | 7 | [692] |
| | Methylene blue | | 15.35 mg/g | | | | | |
| | Cu | | 83–104% | | | | | |
| Layered double hydroxide–carbon dot composite | Methyl blue | Sorption | 185 mg/g | | 60 | 25 | | [693] |
| CQDs@PAFPnanobiosorbent | U(VI) | Sorption | 95–98% | 5 | | | 4 | [694] |
| Graphene quantum dots (GQDs) immobilized onto the $NiFe_2O_4$-halloysite nanotubes ($NiFe_2O_4$-HNTs) | Pb(II) | Sorption | 42.02 mg/g | | | 25 | | [695] |
| PVA/CMC-B@GO/$Fe_3O_4$/GQD (L) | Methylene blue | Sorption | 1000 mg | 8 | 240 | | 4 | [696] |

BET-analyzed surface area of MMT nanoclay was found to be in the range of 277–355 $m^2$/g. The mechanistic approach confirmed that the sorption of arsenite took place through both the outer-sphere (physisorption) and inner-sphere complexes (chemisorption) at the hydroxyl iron nanoclay surface. The sorption capacity obtained for the arsenite removal was 3.85 mg/g. Nikkhah et al. [704] explored the synthesis of a Cloisite 20A nanoclay-modified polyurethane foam structure and used it for the removal of oil from an oil–water system. Sorption capacity of 21.5 mg/g was achieved by the prepared sorbent. Narwade et al. [705] explored the synthesis of hydroxyapatite (HAp) by the wet-chemical precipitation method and used it as a sorbent for phenol removal. Sorption capacity of ~ 64 mg/g was achieved, confirming the efficiency of the prepared substance. Phenol tends to form phenoxide ions when dissolved in water. At acidic pH, a variety of reactions take place between the phenoxide ions and the surface of the CNF–HAp films.

## 13 Mechanism of Pollutant Remediation

Generally, the mechanism of the interaction of heavy metal ions with the sorbents can be discussed in terms of the chelation of the metals with anionic functional groups present on the surface of the sorbent [706]. Heavy metals can be removed through sorption only if they are completely entrapped by the chelating agents present on the surface of the sorbent. Most of the chelating groups contain carboxylic acids which are directly connected to one or more nitrogen atoms. These groups also hinder the precipitation of the metals, inhibit metal ion catalysis, and ensure the availability of metal ions in the reaction system [707]. The key groups taking part in metal chelation are the carboxyl and amino groups.

The pH also affects the uptake of the metals by the chelating groups. If the pH is low, ligands tend to be associated with hydronium ions and inhibit the metal cation approach. Also, at lower pH, the carboxylic groups are mostly not dissociated, although they are part of the complexation reactions. The chelation mechanism follows the formation of quinquedentate, hexadentate, and sometimes distorted structures [708]. In the case of the dye molecules, they generally tend to follow the electrostatic interaction with that of the adsorbent surface. The electrostatic interaction can be affected by properties such as surface charge, degree of ionization, and speciation. In general, the sorbent surface may have acidic or alkaline characteristics, which may interact with the dye contaminants through the pH effect. At lower pH, the surface of the sorbent is protonated, bearing a positive charge. This positive charge will electrostatically attract the negatively charged dyes, causing their removal from the aqueous solution. In the case of a basic medium, the surface of the sorbent may be completely ionized, causing repulsive forces with the dye anions [709].

The interaction of pharmaceutical compounds with sorbent molecules can be explained based on hydrogen bonding. The hydrogen bonding occurs when the hydrogen bonding donor groups on the surface of the sorbent interact with those of

the hydrogen bonding acceptor atoms on the surface of the contaminants. Generally, the functional groups containing nitrogen and oxygen atoms act as the H-acceptors, which may interact with the –OH or phosphorus-containing groups. Other factors involved in the interaction include n–π, and π–π interaction is also common, which is a specific and non-covalent interaction and exists between electron-rich and electron-poor compounds [710].

### 13.1 Mechanism of Sorption

Sorption is a surface phenomenon in which the sorbate molecules attach to the surface of the sorbent through either physical or chemical interactions. The physical interaction, or physisorption, may be driven by van der Waals forces or electrostatic interactions, which are fast, reversible, and result in multilayer formation on the surface of the sorbent. On the contrary, chemical interaction, or chemisorption, exhibits strong covalent bonding which is slower and requires activation energy, is irreversible, and produces a monolayer on the surface of the sorbent. The sorption phenomenon is greatly affected by the reaction conditions such as pH, temperature, time, and sorbate concentration and dosage. The sorption of contaminants can be analyzed by the amount of contaminant sorbed per unit mass of sorbent ($q_e$) and the residual left ($C_e$) at equilibrium conditions. Different isotherm models have been designed to explain the mechanism and bonding interactions [711, 712].

### 13.2 Sorption Isotherm Models

The sorption results can be further evaluated by applying the sorption isotherm models, which are discussed in detail as follows. The Langmuir isotherm model is based on the conditions where the surface of the sorbent is homogeneous, providing equal binding sites, and the sorbate molecules tend to form a monolayer on the surface. The following equation is designed based on the Langmuir model (Eq. 9):

$$\frac{C_e}{q_m} = \frac{1}{K_L q_{\max}} + \frac{C_e}{q_{\max}} \tag{9}$$

where $C_e$ stands for the equilibrium concentration (mg/L), $q_m$ is the amount sorbed per unit mass of sorbent (mg/g), and $K_L$ is the Langmuir equilibrium constant related to the heat of sorption [713].

Another model to explain the sorption process is the Freundlich isotherm model, which is generally applied to the multilayer sorption of sorbate molecules onto a heterogeneous surface. The linear equation of the Freundlich isotherm model is as follows (Eq. 10):

$$\log_{q_m} = logK_f + \frac{1}{n}\log C_e \tag{10}$$

where $q_m$ (mg/g) indicates the molecules sorbed (amount) onto the sorbent surface, *Ce* (mg/L) denotes the equilibrium concentration, and $n$ and $K_f$ are the Freundlich constant and Freundlich exponent, respectively. $K_f$ (mg/g) is the sorption capacity, while $n$ shows the degree of the surface heterogeneity and conveys the distribution of the sorbed molecules on the sorbent surface. A higher value of $n$ indicates a positive rise in sorption and gives the intensity of sorption [714].

Yet another isotherm model, called the Temkin isotherm, shows the effect of the heat of sorption, which is inversely related to the sorption and monolayer formation. The linear decrease in the sorption heat is caused by the interaction between the sorbent and sorbate molecules. The Temkin isotherm model is expressed in the following form (Eq. 11):

$$q_e = \left(\frac{RT}{b_T}\right) ln\left(AC_e\right) \tag{11}$$

Here, $T$ is the temperature (K), $R$ is the ideal gas constant (8.314 J/mol/K), $b_T$ represents the Temkin constant (J/mol), which depends on the heat of sorption, and $A$ is the equilibrium sorption constant, corresponding to the maximum sorption energy (L/mg) [715].

The sorption phenomenon can also be described by the Brunauer–Emmett–Teller isotherm model, which is generally based on the assumptions of the Langmuir sorption isotherms and is widely used to calculate the surface area and porosity of the system. This model is generally applied to gas–solid systems [716]. The equation form of the model can be represented as Eq. (12):

$$lnq_e \tag{12}$$

The Redlich–Peterson isotherm is a combined form of the Langmuir and Freundlich isotherm models, taking hints from the assumptions of both the models. This model is applied to systems having both homogeneous and heterogeneous surfaces of sorbents over a wide range of sorbate concentrations. At higher sorbate concentrations, Freundlich isotherm assumptions are followed, while at a lower concentration, Henry's law is obeyed [717]. The equation, Eq. (13), for this model is represented as follows:

$$\ln q_e = \left(\frac{1}{n_H}\ln K_H\right) - \left(\frac{1}{n_H} ln \frac{1}{C_e}\right) \tag{13}$$

where $K_{RP}$ (L/g) and $\alpha$ (L/mg) are Redlich–Peterson constants, and $\beta$ is an exponential value in the range between 0 and 1. If the $\beta$ value is 0, the isotherm behaves as Langmuir's model, while it obeys Henry's law when the $\beta$ value is 1.

### 13.3 Mechanism of Photocatalysis

A general definition of photocatalysis can be derived from the reported literature, as the breakdown of organic pollutants in a spontaneous reaction from the principles of thermodynamics. As its name suggests, photocatalysis refers to the lysis/breakdown/degradation of pollutants with the aid of light and a catalyst [718–720]. The mechanism of photocatalysis can be divided into four major steps:

- Light is absorbed, which generates electron/hole pairs.
- The excited charges are separated.
- The electrons and the holes are transported to the surface of the photocatalyst.
- The redox reactions occur on the surface by utilizing the charges.

In the third step, the electrons/holes may recombine and scatter the harvested light energy in the form of heat (non-radiative recombination) or light (radiative recombination). The remaining photogenerated charges present on the surface of the catalysts tend to carry out the redox reactions, depending on the acceptor or donor properties of the absorbed species [721, 722].

## 14 Conclusion

Worldwide concern related to wastewater contamination has driven researchers to develop advanced, rapid, and accurate methods for the removal of a variety of contaminants primarily emerging from industrial sources. These contaminants have hazardous effects on living organisms, requiring the development of efficient means of decontamination. This quest has led researchers to the use of NMs based on their unique properties including very small size and high surface area-to-volume ratios. NMs have revolutionized conventional techniques used for the treatment of contaminants such as sorption and photocatalysis by improving and enhancing the productivity of these techniques. Innovation in the field of nanotechnology has been achieved by the functionalization of the pristine NMs, thus incorporating the useful properties of multiple materials to provide better results. This review covers the available reports on the removal of contaminants by FNMs for the past 10 years, highlighting their bright future.

**Acknowledgements** The authors are thankful for the financial support provided by the Practice and Innovation Program of Postgraduates in Jiangsu Province, SJCX20_1332 and the Key Laboratory for Special Resource Development and Medicinal Research in Jiangsu Province, project numbers LPRK202101, 202111049338 and 202111049352.

**Funding** Open Access funding provided by the Qatar National Library.

### Declarations

**Conflict of interest** The authors have no competing interest.

## References

1. Ali N, Bilal M, Khan A, Ali F, Yang Y, Malik S, Iqbal HM (2021) Deployment of metal-organic frameworks as robust materials for sustainable catalysis and remediation of pollutants in environmental settings. Chemosphere 20:129605
2. Saxena G, Purchase D, Bharagava RN (2020) Environmental hazards and toxicity profile of organic and inorganic pollutants of tannery wastewater and bioremediation approaches. Bioremediation of industrial waste for environmental safety. Springer, Singapore, pp 381–398
3. Syam Babu D, Anantha Singh TS, Nidheesh PV, Suresh Kumar M (2019) Industrial wastewater treatment by electrocoagulation process. Sep Sci Technol 20:1–33
4. Goli A, Shamiri A, Khosroyar S, Talaiekhozani A, Sanaye R, Azizi K (2019) A review on different aerobic and anaerobic treatment methods in dairy industry wastewater. J Environ Treat Tech 6(1):113–141
5. Lopera AEC, Ruiz SG, Alonso JMQ (2019) Removal of emerging contaminants from wastewater using reverse osmosis for its subsequent reuse: pilot plant. J Water Process Eng 29:100800
6. Chauhan A, Sillu D, Agnihotri S (2019) Removal of pharmaceutical contaminants in wastewater using nanomaterials: a comprehensive review. Curr Drug Metab 20(6):483–505
7. Wen X, Du C, Zeng G, Huang D, Zhang J, Yin L, Hu X (2018) A novel biosorbent prepared by immobilized *Bacillus licheniformis* for lead removal from wastewater. Chemosphere 200:173–179
8. Akpor OB, Ohiobor GO, Olaolu DT (2014) Heavy metal pollutants in wastewater effluents: sources, effects and remediation. Adv Biosci Bioeng 2(4):37–43
9. Arunakumara KKIU, Walpola BC, Yoon MH (2013) Current status of heavy metal contamination in Asia's rice lands. Rev Environ Sci Bio/Technol 12(4):355–377
10. Pavithra KG, Jaikumar V (2019) Removal of colorants from wastewater: a review on sources and treatment strategies. J Ind Eng Chem 75:1–19
11. Husain Q (2010) Peroxidase mediated decolorization and remediation of wastewater containing industrial dyes: a review. Rev Environ Sci Bio/Technol 9(2):117–140
12. K'oreje KO, Vergeynst L, Ombaka D, De Wispelaere P, Okoth M, Van Langenhove H, Demeestere K (2016) Occurrence patterns of pharmaceutical residues in wastewater, surface water and groundwater of Nairobi and Kisumu city, Kenya. Chemosphere 149:238–244
13. Carbonaro S, Sugihara MN, Strathmann TJ (2013) Continuous-flow photocatalytic treatment of pharmaceutical micropollutants: activity, inhibition, and deactivation of TiO2 photocatalysts in wastewater effluent. Appl Catal B 129:1–12
14. Li X, Wang B, Cao Y, Zhao S, Wang H, Feng X, Ma X (2019) Water contaminant elimination based on metal–organic frameworks and perspective on their industrial applications. ACS Sustain Chem Eng 7(5):4548–4563
15. Peña A, Rodríguez-Liébana JA, Mingorance MD (2011) Persistence of two neonicotinoid insecticides in wastewater, and in aqueous solutions of surfactants and dissolved organic matter. Chemosphere 84(4):464–470
16. Munoz G, Labadie P, Botta F, Lestremau F, Lopez B, Geneste E, Budzinski H (2017) Occurrence survey and spatial distribution of perfluoroalkyl and polyfluoroalkyl surfactants in groundwater, surface water, and sediments from tropical environments. Sci Total Environ 607:243–252
17. Dolar D, Gros M, Rodriguez-Mozaz S, Moreno J, Comas J, Rodriguez-Roda I, Barceló D (2012) Removal of emerging contaminants from municipal wastewater with an integrated membrane system, MBR–RO. J Hazard Mater 239:64–69

18. Mahmood A, Malik RN (2014) Human health risk assessment of heavy metals via consumption of contaminated vegetables collected from different irrigation sources in Lahore, Pakistan. Arab J Chem 7(1):91–99
19. Balsamo M, Di Natale F, Erto A, Lancia A, Montagnaro F, Santoro L (2010) Arsenate removal from synthetic wastewater by adsorption onto fly ash. Desalination 263(1–3):58–63
20. Salmani MH, Davoodi M, Ehrampoush MH, Ghaneian MT, Fallahzadah MH (2013) Removal of cadmium (II) from simulated wastewater by ion flotation technique. Iran J Environ Health Sci Eng 10(1):16
21. Fang D, Liao X, Zhang X, Teng A, Xue X (2018) A novel resource utilization of the calcium-based semi-dry flue gas desulfurization ash: as a reductant to remove chromium and vanadium from vanadium industrial wastewater. J Hazard Mater 342:436–445
22. Bhatluri KK, Manna MS, Saha P, Ghoshal AK (2014) Supported liquid membrane-based simultaneous separation of cadmium and lead from wastewater. J Membr Sci 459:256–263
23. Soni R, Bhatnagar A, Vivek R, Singh R, Chaturvedi TP, Singh A (2012) A systematic review on mercury toxicity from dental amalgam fillings and its management strategies. J Sci Res 56:81–92
24. Attari M, Bukhari SS, Kazemian H, Rohani S (2017) A low-cost adsorbent from coal fly ash for mercury removal from industrial wastewater. J Environ Chem Eng 5(1):391–399
25. Bafana A, Devi SS, Chakrabarti T (2011) Azo dyes: past, present and the future. Environ Rev 19:350–371
26. Ahmad A, Mohd-Setapar SH, Chuong CS, Khatoon A, Wani WA, Kumar R, Rafatullah M (2015) Recent advances in new generation dye removal technologies: novel search for approaches to reprocess wastewater. RSC Adv 5(39):30801–30818
27. Wawrzkiewicz M, Bartczak P, Jesionowski T (2017) Enhanced removal of hazardous dye form aqueous solutions and real textile wastewater using bifunctional chitin/lignin biosorbent. Int J Biol Macromol 99:754–764
28. Kimura A, Osawa M, Taguchi M (2012) Decomposition of persistent pharmaceuticals in wastewater by ionizing radiation. Radiat Phys Chem 81(9):1508–1512
29. Gros M, Petrović M, Ginebreda A, Barceló D (2010) Removal of pharmaceuticals during wastewater treatment and environmental risk assessment using hazard indexes. Environ Int 36(1):15–26
30. Patneedi CB, Prasadu KD (2015) Impact of pharmaceutical wastes on human life and environment. Rasayan J Chem 8(1):67–70
31. Shahmoradi MH, Zade BA, Torabian A, Salehi MS (2015) Removal of nitrate from ground water using activated carbon prepared from rice husk and sludge of paper industry wastewater treatment. ARPN J Eng Appl Sci 10(17):7856–7863
32. Nawaz A, Khan A, Ali N, Ali N, Bilal M (2020) Fabrication and characterization of new ternary ferrites-chitosan nanocomposite for solar-light driven photocatalytic degradation of a model textile dye. Environ Technol Innov 20:101079
33. Ali N, Bilal M, Khan A, Ali F, Yang Y, Khan M, Iqbal HM (2020) Dynamics of oil-water interface demulsification using multifunctional magnetic hybrid and assembly materials. J Mol Liquids 20:113434
34. Rai PK, Lee SS, Zhang M, Tsang YF, Kim KH (2019) Heavy metals in food crops: health risks, fate, mechanisms, and management. Environ Int 125:365–385
35. Ali N, Naz N, Shah Z, Khan A, Nawaz R (2020) Selective transportation of molybdenum from model and ore through poly inclusion membrane. Bull Chem Soc Ethiop 34(1):93–104
36. Ali N, Bilal M, Nazir MS, Khan A, Ali F, Iqbal HM (2020) Thermochemical and electrochemical aspects of carbon dioxide methanation: a sustainable approach to generate fuel via waste to energy theme. Sci Total Environ 712:136482
37. Ali N, Azeem S, Khan A, Khan H, Kamal T, Asiri AM (2020) Experimental studies on removal of arsenites from industrial effluents using tridodecylamine supported liquid membrane. Environ Sci Pollut Res 20:1–12
38. Ali N, Bilal M, Khan A, Ali F, Iqbal HM (2020) Design, engineering and analytical perspectives of membrane materials with smart surfaces for efficient oil/water separation. Trends Anal Chem 20:115902
39. Pan ZF, An L (2019) Removal of heavy metal from wastewater using ion exchange membranes. Applications of ion exchange materials in the environment. Springer, Cham, pp 25–46
40. Jamil S, Loganathan P, Listowski A, Kandasamy J, Khourshed C, Vigneswaran S (2019) Simultaneous removal of natural organic matter and micro-organic pollutants from reverse osmosis concentrate using granular activated carbon. Water Res 155:106–114

41. Segundo IDB, Silva TF, Moreira FC, Silva GV, Boaventura RA, Vilar VJ (2019) Sulphur compounds removal from an industrial landfill leachate by catalytic oxidation and chemical precipitation: from a hazardous effluent to a value-added product. Sci Total Environ 655:1249–1260
42. Efome JE, Rana D, Matsuura T, Lan CQ (2019) Effects of operating parameters and coexisting ions on the efficiency of heavy metal ions removal by nano-fibrous metal-organic framework membrane filtration process. Sci Total Environ 674:355–362
43. Bruno P, Campo R, Giustra MG, De Marchis M, Di Bella G (2020) Bench scale continuous coagulation-flocculation of saline industrial wastewater contaminated by hydrocarbons. J Water Process Eng 34:101156
44. Chen F, Yu W, Qie Y, Zhao L, Zhang H, Guo LH (2019) Enhanced photocatalytic removal of hexavalent chromium through localized electrons in polydopamine-modified TiO2 under visible irradiation. Chem Eng J 373:58–67
45. Sartaj S, Ali N, Khan A, Malik S, Bilal M, Khan M, Khan S (2020) Performance evaluation of photolytic and electrochemical oxidation processes for enhanced degradation of food dyes laden wastewater. Water Sci Technol 81(5):971–984
46. Khan MF, Yu L, Achari G, Tay JH (2019) Degradation of sulfolane in aqueous media by integrating activated sludge and advanced oxidation process. Chemosphere 222:1–8
47. Regkouzas P, Diamadopoulos E (2019) Adsorption of selected organic micro-pollutants on sewage sludge biochar. Chemosphere 224:840–851
48. Crini G, Lichtfouse E (2019) Advantages and disadvantages of techniques used for wastewater treatment. Environ Chem Lett 17(1):145–155
49. Khan A, Shah SJ, Mehmood K, Ali N, Khan H (2019) Synthesis of potent chitosan beads a suitable alternative for textile dye reduction in sunlight. J Mater Sci Mater Electron 30(1):406–414
50. Ali N, Kamal T, Ul-Islam M, Khan A, Shah SJ, Zada A (2018) Chitosan-coated cotton cloth supported copper nanoparticles for toxic dye reduction. Int J Biol Macromol 111:832–838
51. Ali N, Khan A, Malik S, Badshah S, Bilal M, Iqbal HM (2020) Chitosan-based green sorbent material for cations removal from an aqueous environment. J Environ Chem Eng 20:104064
52. Khan H, Gul K, Ara B, Khan A, Ali N, Ali N, Bilal M (2020) Adsorptive removal of acrylic acid from the aqueous environment using raw and chemically modified alumina: batch adsorption, kinetic, equilibrium and thermodynamic studies. J Environ Chem Eng 20:103927
53. Ali N, Khan A, Bilal M, Malik S, Badshah S, Iqbal H (2020) Chitosan-based bio-composite modified with thiocarbamate moiety for decontamination of cations from the aqueous media. Molecules 25(1):226
54. Ali N, Khan A, Nawaz S, Bilal M, Malik S, Badshah S, Iqbal HM (2020) Characterization and deployment of surface-engineered chitosan-triethylenetetramine nanocomposite hybrid nanoadsorbent for divalent cations decontamination. Int J Biol Macromol 152:663–671
55. Khan A, Ali N, Bilal M, Malik S, Badshah S, Iqbal H (2019) Engineering functionalized chitosan-based sorbent material: characterization and sorption of toxic elements. Appl Sci 9(23):5138
56. Vaiano V, Sacco O, Sannino D, Ciambelli P (2015) Photocatalytic removal of spiramycin from wastewater under visible light with N-doped TiO2 photocatalysts. Chem Eng J 261:3–8
57. Ali N, Zada A, Zahid M, Ismail A, Rafiq M, Riaz A, Khan A (2019) Enhanced photodegradation of methylene blue with alkaline and transition-metal ferrite nanophotocatalysts under direct sun light irradiation. J Chin Chem Soc 66(4):402–408
58. Saeed K, Sadiq M, Khan I, Ullah S, Ali N, Khan A (2018) Synthesis, characterization, and photocatalytic application of Pd/ZrO 2 and Pt/ZrO 2. Appl Water Sci 8(2):60
59. Lu F, Astruc D (2020) Nanocatalysts and other nanomaterials for water remediation from organic pollutants. Coord Chem Rev 408:213180
60. Yaqoob AA, Parveen T, Umar K, Mohamad Ibrahim MN (2020) Role of nanomaterials in the treatment of wastewater: a review. Water 12(2):495
61. Xiao B (2019) Development status, prospects and industrial policies of nanomaterials and nanotechnology. In: AIP conference proceedings (vol 2185, No. 1, p. 020042). AIP Publishing LLC.
62. Bolade OP, Williams AB, Benson NU (2020) Green synthesis of iron-based nanomaterials for environmental remediation: a review. Environ Nanotechnol Monit Manage 13:100279
63. Agarwal P, Gupta R, Agarwal N (2019) Advances in synthesis and applications of microalgal nanoparticles for wastewater treatment. J Nanotechnol 20:20
64. Ahmad J, Naeem S, Ahmad M, Usman AR, Al-Wabel MI (2019) A critical review on organic micropollutants contamination in wastewater and removal through carbon nanotubes. J Environ Manage 246:214–228

65. Han R, Zhang Y, Xie Y (2020) Application of Mn3O4 nanowires in the dye waste water treatment at room temperature. Sep Purif Technol 234:116119
66. Gandavadi D, Sundarrajan S, Ramakrishna S (2019) Bio-based nanofibers involved in wastewater treatment. Macromol Mater Eng 304(11):1900345
67. Sadegh H, Ali GA (2019) Potential applications of nanomaterials in wastewater treatment: nanoadsorbents performance. In: Advanced treatment techniques for industrial wastewater, pp 51–61. IGI Global
68. Wadhawan S, Jain A, Nayyar J, Mehta SK (2020) Role of nanomaterials as adsorbents in heavy metal ion removal from waste water: a review. J Water Process Eng 33:101038
69. Fadlalla MI, Kumar PS, Selvam V, Babu SG (2019) Recent advances in nanomaterials for wastewater treatment. Advanced nanostructured materials for environmental remediation. Springer, Cham, pp 21–58
70. Meng Z, Stolz RM, Mendecki L, Mirica KA (2019) Electrically-transduced chemical sensors based on two-dimensional nanomaterials. Chem Rev 119(1):478–598
71. Huang CH, Chen P, Liu XM, Li F (2020) Metal-organic nanomaterials for drug delivery. Polymers in therapeutic delivery. American Chemical Society, New York, pp 79–95
72. Khieu DQ, Dinh NT, Mau TX, Mai HD (2019) Synthesis and application of novel hybrid nanomaterials in catalysis, adsorption, and electrochemistry. Adv Mater Sci Eng 20:19
73. Pomerantseva E, Bonaccorso F, Feng X, Cui Y, Gogotsi Y (2019) Energy storage: the future enabled by nanomaterials. Science 366:6468
74. Chenab KK, Sohrabi B, Jafari A, Ramakrishna S (2020) Water treatment: functional nanomaterials and applications from adsorption to photodegradation. Mater Today Chem 16:100262
75. Khan A, Begum S, Ali N, Khan S, Hussain S, Sotomayor MDPT (2017) Preparation of crosslinked chitosan magnetic membrane for cations sorption from aqueous solution. Water Sci Technol 75(9):2034–2046
76. Khan A, Badshah S, Airoldi C (2015) Environmentally benign modified biodegradable chitosan for cation removal. Polym Bull 72(2):353–370
77. Khan A, Wahid F, Ali N, Badshah S, Airoldi C (2015) Single-step modification of chitosan for toxic cations remediation from aqueous solution. Desalin Water Treat 56(4):1099–1109
78. Khan A, Badshah S, Airoldi C (2011) Biosorption of some toxic metal ions by chitosan modified with glycidylmethacrylate and diethylenetriamine. Chem Eng J 171(1):159–166
79. Gatoo MA, Naseem S, Arfat MY, Mahmood Dar A, Qasim K, Zubair S (2014) Physicochemical properties of nanomaterials: implication in associated toxic manifestations. BioMed Res Int 20:14
80. Madamsetty VS, Paul MK, Mukherjee A, Mukherjee S (2019) Functionalization of nanomaterials and their application in melanoma cancer theranostics. ACS Biomater Sci Eng 6(1):167–181
81. Yadav T, Pfaffenbach K (2011) U.S. Patent No. 7,892,599. Washington, DC: U.S. Patent and Trademark Office
82. Hore MJ, Korley LT, Kumar SK (2020) Polymer-grafted nanoparticles
83. Chaudhary S, Sharma P, Chauhan P, Kumar R, Umar A (2019) Functionalized nanomaterials: a new avenue for mitigating environmental problems. Int J Environ Sci Technol 20:1–28
84. Chong WC, Koo CH, Lau WJ (2020) Mixed-matrix membranes incorporated with functionalized nanomaterials for water applications. Handbook of functionalized nanomaterials for industrial applications. Elsevier, New York, pp 15–51
85. Luo T, Wang X, Qian Y, Liu J, Li L, Liu J, Chen J (2019) Direct and sensitive detection of sulfide ions based on one-step synthesis of ionic liquid functionalized fluorescent carbon nanoribbons. RSC Adv 9(64):37484–37490
86. Rani M, Shanker U (2020) Remediation of organic pollutants by potential functionalized nanomaterials. Handbook of functionalized nanomaterials for industrial applications. Elsevier, New York, pp 327–398
87. Rawtani D, Tharmavaram M, Pandey G, Hussain CM (2019) Functionalized nanomaterial for forensic sample analysis. Trends Anal Chem 20:115661
88. Jawed A, Saxena V, Pandey LM (2020) Engineered nanomaterials and their surface functionalization for the removal of heavy metals: a review. J Water Process Eng 33:101009
89. Liu J, Ye Y, Xue Y, Xie X, Mai YW (2017) Recent advances in covalent functionalization of carbon nanomaterials with polymers: strategies and perspectives. J Polym Sci Part A Polym Chem 55(4):622–631

90. Liu H, Zhao HY, Müller-Plathe F, Qian HJ, Sun ZY, Lu ZY (2018) Distribution of the number of polymer chains grafted on nanoparticles fabricated by grafting-to and grafting-from procedures. Macromolecules 51(10):3758–3766
91. Yang Y, Liu X, Ye G, Zhu S, Wang Z, Huo X, Chen J (2017) Metal-free photoinduced electron transfer-atom transfer radical polymerization integrated with bioinspired polydopamine chemistry as a green strategy for surface engineering of magnetic nanoparticles. ACS Appl Mater Interfaces 9(15):13637–13646
92. Magenau AJ, Strandwitz NC, Gennaro A, Matyjaszewski K (2011) Electrochemically mediated atom transfer radical polymerization. Science 332(6025):81–84
93. Massoumi B, Mousavi-Hamamlu SV, Ghamkhari A, Jaymand M (2017) A novel strategy for synthesis of polystyrene/Fe3O4 nanocomposite: RAFT polymerization, functionalization, and coordination techniques. Polym-Plast Technol Eng 56(8):873–882
94. Moad G, Rizzardo E, Thang SH (2013) RAFT polymerization and some of its applications. Chem Asian J 8(8):1634–1644
95. Roy S, Das T, Yue CY, Hu X (2014) Improved polymer encapsulation on multiwalled carbon nanotubes by selective plasma induced controlled polymer grafting. ACS Appl Mater Interfaces 6(1):664–670
96. Rajendran Royan NR, Sulong AB, Yuhana NY, Chen RS, Ab Ghani MH, Ahmad S (2018) UV/O3 treatment as a surface modification of rice husk towards preparation of novel biocomposites. PLoS One 13(5):e0197345
97. Ibrahim GS, Isloor AM, Asiri AM, Ismail N, Ismail AF, Ashraf GM (2017) Novel, one-step synthesis of zwitterionic polymer nanoparticles via distillation-precipitation polymerization and its application for dye removal membrane. Sci Rep 7(1):1–16
98. Liu J, Yang K, Qu Y, Li S, Wu Q, Liang Z, Zhang Y (2015) An efficient approach to prepare boronate core–shell polymer nanoparticles for glycoprotein recognition via combined distillation precipitation polymerization and RAFT media precipitation polymerization. Chem Commun 51(18):3896–3898
99. Huang Q, Liu M, Mao L, Xu D, Zeng G, Huang H, Wei Y (2017) Surface functionalized SiO2 nanoparticles with cationic polymers via the combination of mussel inspired chemistry and surface initiated atom transfer radical polymerization: characterization and enhanced removal of organic dye. J Colloid Interface Sci 499:170–179
100. Zoppe JO, Ataman NC, Mocny P, Wang J, Moraes J, Klok HA (2017) Surface-initiated controlled radical polymerization: state-of-the-art, opportunities, and challenges in surface and interface engineering with polymer brushes. Chem Rev 117(3):1105–1318
101. Zhang X, Wu D, Shen J, Wei Y, Wang C (2020) Preparation of bottlebrush polymer–modified magnetic graphene as immobilized metal ion affinity adsorbent for purification of hemoglobin from blood samples. Microchim Acta 187(8):1–9
102. Chen X, Yi M, Wu S, Tan L, Ge X, He M, Yin G (2019) Synthesis of structurally precise polysiloxanes via the Piers-Rubinsztajn reaction. Materials 12(2):304
103. Park HM, Oh H, Jee KY, Lee YT (2020) Synthesis of PVDF/MWCNT nanocomplex microfiltration membrane via atom transfer radical addition (ATRA) with enhanced fouling performance. Sep Purif Technol 20:116860
104. Jamshaid A, Hamid A, Muhammad N, Naseer A, Ghauri M, Iqbal J, Shah NS (2017) Cellulose-based materials for the removal of heavy metals from wastewater—an overview. ChemBioEng Rev 4(4):240–256
105. Tahir MB, Kiran H, Iqbal T (2019) The detoxification of heavy metals from aqueous environment using nano-photocatalysis approach: a review. Environ Sci Pollut Res 26(11):10515–10528
106. Khan H, Khalil AK, Khan A, Saeed K, Ali N (2016) Photocatalytic degradation of bromophenol blue in aqueous medium using chitosan conjugated magnetic nanoparticles. Korean J Chem Eng 33(10):2802–2807
107. Grassi M, Kaykioglu G, Belgiorno V, Lofrano G (2012) Removal of emerging contaminants from water and wastewater by adsorption process. Emerging compounds removal from wastewater. Springer, Dordrecht, pp 15–37
108. Bashir A, Malik LA, Ahad S, Manzoor T, Bhat MA, Dar GN, Pandith AH (2019) Removal of heavy metal ions from aqueous system by ion-exchange and biosorption methods. Environ Chem Lett 17(2):729–754
109. Ahmed MJ, Hameed BH (2018) Removal of emerging pharmaceutical contaminants by adsorption in a fixed-bed column: a review. Ecotoxicol Environ Saf 149:257–266

110. Sulyman M, Namiesnik J, Gierak A (2017) Low-cost adsorbents derived from agricultural by-products/wastes for enhancing contaminant uptakes from wastewater: a review. Pol J Environ Stud 26:3
111. Crini G, Lichtfouse E, Wilson LD, Morin-Crini N (2019) Conventional and non-conventional adsorbents for wastewater treatment. Environ Chem Lett 17(1):195–213
112. Mallampati R, Xuanjun L, Adin A, Valiyaveettil S (2015) Fruit peels as efficient renewable adsorbents for removal of dissolved heavy metals and dyes from water. ACS Sustain Chem Eng 3(6):1117–1124
113. Kurniawan TA, Waihung L, Repo E, Sillanpää ME (2010) Removal of 4-chlorophenol from contaminated water using coconut shell waste pretreated with chemical agents. J Chem Technol Biotechnol 85(12):1616–1627
114. Dimpe KM, Ngila JC, Nomngongo PN (2017) Application of waste tyre-based activated carbon for the removal of heavy metals in wastewater. Cogent Eng 4(1):1330912
115. Asl SMH, Javadian H, Khavarpour M, Belviso C, Taghavi M, Maghsudi M (2019) Porous adsorbents derived from coal fly ash as cost-effective and environmentally-friendly sources of aluminosilicate for sequestration of aqueous and gaseous pollutants: a review. J Clean Prod 208:1131–1147
116. Adegoke KA, Oyewole RO, Lasisi BM, Bello OS (2017) Abatement of organic pollutants using fly ash based adsorbents. Water Sci Technol 76(10):2580–2592
117. Gao W, Fatehi P (2018) Fly ash based adsorbent for treating bleaching effluent of kraft pulping process. Sep Purif Technol 195:60–69
118. Zhou Y, Liu X, Xiang Y, Wang P, Zhang J, Zhang F, Tang L (2017) Modification of biochar derived from sawdust and its application in removal of tetracycline and copper from aqueous solution: adsorption mechanism and modelling. Biores Technol 245:266–273
119. Kasiuliene A, Carabante I, Bhattacharya P, Caporale AG, Adamo P, Kumpiene J (2018) Removal of metal (oid) s from contaminated water using iron-coated peat sorbent. Chemosphere 198:290–296
120. Shamsollahi Z, Partovinia A (2019) Recent advances on pollutants removal by rice husk as a bio-based adsorbent: a critical review. J Environ Manage 246:314–323
121. Ratnamala GM, Shetty KV, Srinikethan G (2012) Removal of remazol brilliant blue dye from dye-contaminated water by adsorption using red mud: equilibrium, kinetic, and thermodynamic studies. Water Air Soil Pollut 223(9):6187–6199
122. Pietrelli L, Ippolito NM, Ferro S, Dovì VG, Vocciante M (2019) Removal of Mn and As from drinking water by red mud and pyrolusite. J Environ Manage 237:526–533
123. Gu S, Kang X, Wang L, Lichtfouse E, Wang C (2019) Clay mineral adsorbents for heavy metal removal from wastewater: a review. Environ Chem Lett 17(2):629–654
124. Yasipourtehrani S, Strezov V, Evans T (2019) Investigation of phosphate removal capability of blast furnace slag in wastewater treatment. Sci Rep 9(1):1–9
125. Devi P, Saroha AK (2017) Utilization of sludge based adsorbents for the removal of various pollutants: a review. Sci Total Environ 578:16–33
126. Sari AA, Amriani F, Muryanto M, Triwulandari E, Sudiyani Y, Barlianti V, Hadibarata T (2017) Mechanism, adsorption kinetics and applications of carbonaceous adsorbents derived from black liquor sludge. J Taiwan Inst Chem Eng 77:236–243
127. Anastopoulos I, Bhatnagar A, Hameed BH, Ok YS, Omirou M (2017) A review on waste-derived adsorbents from sugar industry for pollutant removal in water and wastewater. J Mol Liq 240:179–188
128. Labidi A, Salaberria AM, Fernandes SC, Labidi J, Abderrabba M (2016) Adsorption of copper on chitin-based materials: kinetic and thermodynamic studies. J Taiwan Inst Chem Eng 65:140–148
129. Wilson LD, Tewari BB (2018) Chitosan-based adsorbents: environmental applications for the removal of arsenicals. Mater Res Found 34:133–160
130. Edathil AA, Pal P, Banat F (2018) Alginate clay hybrid composite adsorbents for the reclamation of industrial lean methyldiethanolamine solutions. Appl Clay Sci 156:213–223
131. Xiang Y, Xu Z, Wei Y, Zhou Y, Yang X, Yang Y, Zhou Z (2019) Carbon-based materials as adsorbent for antibiotics removal: mechanisms and influencing factors. J Environ Manage 237:128–138
132. Jiang N, Shang R, Heijman SG, Rietveld LC (2018) High-silica zeolites for adsorption of organic micro-pollutants in water treatment: a review. Water Res 144:145–161
133. Nagpal M, Kakkar R (2019) Use of metal oxides for the adsorptive removal of toxic organic pollutants. Sep Purif Technol 211:522–539

134. Khan AA, Kumari S, Chowdhury A, Hussain S (2018) Phase tuned originated dual properties of cobalt sulfide nanostructures as photocatalyst and adsorbent for removal of dye pollutants. ACS Appl Nano Mater 1(7):3474–3485
135. Xia X, Wang L, Sui N, Colvin VL, William WY (2020) Recent progress in transition metal selenide electrocatalysts for water splitting. Nanoscale 12(23):12249–12262
136. Hakami O, Zhang Y, Banks CJ (2012) Thiol-functionalised mesoporous silica-coated magnetite nanoparticles for high efficiency removal and recovery of Hg from water. Water Res 46(12):3913–3922
137. Singh S, Barick KC, Bahadur D (2011) Surface engineered magnetic nanoparticles for removal of toxic metal ions and bacterial pathogens. J Hazard Mater 192(3):1539–1547
138. Song J, Oh H, Kong H, Jang J (2011) Polyrhodanine modified anodic aluminum oxide membrane for heavy metal ions removal. J Hazard Mater 187(1–3):311–317
139. Parida K, Mishra KG, Dash SK (2012) Adsorption of toxic metal ion Cr (VI) from aqueous state by TiO2-MCM-41: equilibrium and kinetic studies. J Hazard Mater 241:395–403
140. Zhang J, Zhai S, Li S, Xiao Z, Song Y, An Q, Tian G (2013) Pb (II) removal of Fe3O4@ SiO2–NH2 core–shell nanomaterials prepared via a controllable sol–gel process. Chem Eng J 215:461–471
141. Ge F, Li MM, Ye H, Zhao BX (2012) Effective removal of heavy metal ions Cd2+, Zn2+, Pb2+, Cu2+ from aqueous solution by polymer-modified magnetic nanoparticles. J Hazard Mater 211:366–372
142. Papoulis D (2019) Halloysite based nanocomposites and photocatalysis: a review. Appl Clay Sci 168:164–174
143. Al-Mamun MR, Kader S, Islam MS, Khan MZH (2019) Photocatalytic activity improvement and application of UV-TiO2 photocatalysis in textile wastewater treatment: a review. J Environ Chem Eng 7(5):103248
144. Yan Y, Yang H, Yi Z, Xian T, Wang X (2019) Direct Z-scheme CaTiO 3@ BiOBr composite photocatalysts with enhanced photodegradation of dyes. Environ Sci Pollut Res 26(28):29020–29031
145. Wu LY, Mu YF, Guo XX, Zhang W, Zhang ZM, Zhang M, Lu TB (2019) Encapsulating perovskite quantum dots in iron-based metal–organic frameworks (MOFs) for efficient photocatalytic CO2 reduction. Angew Chem Int Ed 58(28):9491–9495
146. Xue X, Chen R, Yan C, Zhao P, Hu Y, Zhang W, Jin Z (2019) Review on photocatalytic and electrocatalytic artificial nitrogen fixation for ammonia synthesis at mild conditions: advances, challenges and perspectives. Nano Res 20:1–21
147. Schreck M, Niederberger M (2019) Photocatalytic gas phase reactions. Chem Mater 31(3):597–618
148. Iervolino G, Zammit I, Vaiano V, Rizzo L (2020) Limitations and prospects for wastewater treatment by UV and visible-light-active heterogeneous photocatalysis: a critical review. Top Curr Chem 378(1):7
149. Ateia M, Alalm MG, Awfa D, Johnson MS, Yoshimura C (2020) Modeling the degradation and disinfection of water pollutants by photocatalysts and composites: a critical review. Sci Total Environ 698:134197
150. Shayegan Z, Lee CS, Haghighat F (2018) TiO2 photocatalyst for removal of volatile organic compounds in gas phase—a review. Chem Eng J 334:2408–2439
151. Sanwald KE, Berto TF, Jentys A, Camaioni DM, Gutiérrez OY, Lercher JA (2018) Kinetic coupling of water splitting and photoreforming on SrTiO3-based photocatalysts. ACS Catal 8(4):2902–2913
152. Zarezadeh S, Habibi-Yangjeh A, Mousavi M (2019) BiOBr and AgBr co-modified ZnO photocatalyst: a novel nanocomposite with pnn heterojunctions for highly effective photocatalytic removal of organic contaminants. J Photochem Photobiol A 379:11–23
153. Vaiano V, Sacco O, Sannino D, Ciambelli P (2015) Process intensification in the removal of organic pollutants from wastewater using innovative photocatalysts obtained coupling Zinc Sulfide based phosphors with nitrogen doped semiconductors. J Clean Prod 100:208–211
154. Ma N, Chen A, Bian Z, Yang Y, Wang H (2019) In situ synthesis of a cadmium sulfide/reduced graphene oxide/bismuth Z-scheme oxyiodide system for enhanced photocatalytic performance in chlorinated paraben degradation. Chem Eng J 359:530–541
155. Pouran SR, Raman AAA, Daud WMAW (2014) Review on the application of modified iron oxides as heterogeneous catalysts in Fenton reactions. J Clean Prod 64:24–35
156. Zinatloo-Ajabshir S, Morassaei MS, Salavati-Niasari M (2017) Facile fabrication of Dy2Sn2O7-SnO2 nanocomposites as an effective photocatalyst for degradation and removal of organic contaminants. J Colloid Interface Sci 497:298–308

157. Rey A, García-Muñoz P, Hernández-Alonso MD, Mena E, García-Rodríguez S, Beltrán FJ (2014) WO3–TiO2 based catalysts for the simulated solar radiation assisted photocatalytic ozonation of emerging contaminants in a municipal wastewater treatment plant effluent. Appl Catal B 154:274–284
158. Men Q, Wang T, Ma C, Yang L, Liu Y, Huo P, Yan Y (2019) In-suit preparation of CdSe quantum dots/porous channel biochar for improving photocatalytic activity for degradation of tetracycline. J Taiwan Inst Chem Eng 99:180–192
159. Haldorai Y, Shim JJ (2013) Multifunctional chitosan-copper oxide hybrid material: photocatalytic and antibacterial activities. Int J Photoenergy 20:13
160. Hong Y, Li C, Zhang G, Meng Y, Yin B, Zhao Y, Shi W (2016) Efficient and stable Nb2O5 modified g-C3N4 photocatalyst for removal of antibiotic pollutant. Chem Eng J 299:74–84
161. Varma KS, Tayade RJ, Shah KJ, Joshi PA, Shukla AD, Gandhi VG (2020) Photocatalytic degradation of pharmaceutical and pesticide compounds (PPCs) using doped TiO2 nanomaterials: a review. Water-Energy Nexus 20:20
162. Narayanam N, Chintakrinda K, Fang WH, Kang Y, Zhang L, Zhang J (2016) Azole functionalized polyoxo-titanium clusters with sunlight-driven dye degradation applications: synthesis, structure, and photocatalytic studies. Inorg Chem 55(20):10294–10301
163. Gomes J, Lincho J, Domingues E, Quinta-Ferreira RM, Martins RC (2019) N-TiO2 photocatalysts: a review of their characteristics and capacity for emerging contaminants removal. Water 11(2):373
164. Hussain M, Sun H, Karim S, Nisar A, Khan M, Ul Haq A, Ahmad M (2016) Noble metal nanoparticle-functionalized ZnO nanoflowers for photocatalytic degradation of RhB dye and electrochemical sensing of hydrogen peroxide. J Nanopart Res 18(4):95
165. Di Giovanni C, Wang WA, Nowak S, Grenèche JM, Lecoq H, Mouton L, Tard C (2014) Bioinspired iron sulfide nanoparticles for cheap and long-lived electrocatalytic molecular hydrogen evolution in neutral water. ACS Catal 4(2):681–687
166. Di T, Xu Q, Ho W, Tang H, Xiang Q, Yu J (2019) Review on metal sulphide-based Z-scheme photocatalysts. ChemCatChem 11(5):1394–1411
167. He Y, Zhao DL, Chung TS (2018) Na+ functionalized carbon quantum dot incorporated thin-film nanocomposite membranes for selenium and arsenic removal. J Membr Sci 564:483–491
168. Wu C, Xie Q, Hong Z, Shen L, Yu T, Guo H, Shao W (2021) Thin-film nanocomposite nanofiltration membrane with enhanced desalination and antifouling performance via incorporating L-aspartic acid functionalized graphene quantum dots. Desalination 498:114811
169. Yáñez-Sedeño P, Campuzano S, Pingarrón JM (2017) Fullerenes in electrochemical catalytic and affinity biosensing: a review. C J Carbon Res 3(3):21
170. Ali I, Mbianda XY, Burakov A, Galunin E, Burakova I, Mkrtchyan E, Grachev V (2019) Graphene based adsorbents for remediation of noxious pollutants from wastewater. Environ Int 127:160–180
171. Wahid F, Mohammadzai IU, Khan A, Shah Z, Hassan W, Ali N (2017) Removal of toxic metals with activated carbon prepared from *Salvadora persica*. Arab J Chem 10:S2205–S2212
172. Gusain R, Kumar N, Ray SS (2020) Recent advances in carbon nanomaterial-based adsorbents for water purification. Coord Chem Rev 405:213111
173. Shoukat R, Khan MI (2021) Carbon nanotubes: a review on properties, synthesis methods and applications in micro and nanotechnology. Microsyst Technol 20:1–10
174. Alkahlawy A, El-Salamony R, Gobara HM (2021) Photocatalytic degradation of congo red dye via multi-walled carbon nanotubes modified CuO and ZnO nanoparticles under visible light irradiation. Egypt J Chem 64(3):10–11
175. Ho CH, Tseng CY, Tien LC (2010) Thermoreflectance characterization of β-Ga 2 O 3 thin-film nanostrips. Opt Express 18(16):16360–16369
176. El-Salamony RA (2016) Advances in photo-catalytic materials for environmental applications. Res Rev J Mat Sci 4(2):26–50
177. Li Z, Sellaoui L, Franco D, Netto MS, Georgin J, Dotto GL, Li Q (2020) Adsorption of hazardous dyes on functionalized multiwalled carbon nanotubes in single and binary systems: experimental study and physicochemical interpretation of the adsorption mechanism. Chem Eng J 389:124467
178. Mallakpour S, Rashidimoghadam S (2019) Poly (vinyl alcohol)/Vitamin C-multi walled carbon nanotubes composites and their applications for removal of methylene blue: advanced comparison between linear and nonlinear forms of adsorption isotherms and kinetics models. Polymer 160:115–125

179. Shao D, Sheng G, Chen C, Wang X, Nagatsu M (2010) Removal of polychlorinated biphenyls from aqueous solutions using β-cyclodextrin grafted multiwalled carbon nanotubes. Chemosphere 79(7):679–685
180. Rajabi M, Mahanpoor K, Moradi O (2017) Removal of dye molecules from aqueous solution by carbon nanotubes and carbon nanotube functional groups: critical review. RSC Adv 7(74):47083–47090
181. Dehghani MH, Yetilmezsoy K, Salari M, Heidarinejad Z, Yousefi M, Sillanpää M (2020) Adsorptive removal of cobalt (II) from aqueous solutions using multi-walled carbon nanotubes and γ-alumina as novel adsorbents: modelling and optimization based on response surface methodology and artificial neural network. J Mol Liq 299:112154
182. Alguacil FJ, López FA (2020) On the active adsorption of chromium (III) from alkaline solutions using multiwalled carbon nanotubes. Appl Sci 10(1):36
183. Ahmad M, Wang J, Xu J, Zhang Q, Zhang B (2020) Magnetic tubular carbon nanofibers as efficient Cu (II) ion adsorbent from wastewater. J Clean Prod 252:119825
184. Yuan MM, Zou J, Guan JF, Huang ZN, Yu JG (2020) Highly sensitive and selective determination of p-nitrophenol at an interpenetrating networks structure of self-assembled rod-like lanthanum hydroxide-oxidized multi-walled carbon nanotubes nanocomposite. Ecotoxicol Environ Saf 201:110862
185. Fayazi M (2020) Removal of mercury (II) from wastewater using a new and effective composite: sulfur-coated magnetic carbon nanotubes. Environ Sci Pollut Res 20:1–10
186. Bin-Dahman OA, Saleh TA (2020) Synthesis of carbon nanotubes grafted with PEG and its efficiency for the removal of phenol from industrial wastewater. Environ Nanotechnol Monit Manage 13:100286
187. Li S, Li Z, Ke B, He Z, Cui Y, Pan Z, Su J (2019) Magnetic multi-walled carbon nanotubes modified with polyaluminium chloride for removal of humic acid from aqueous solution. J Mol Liq 279:241–250
188. Xue JH, Zhang H, Ding DX, Hu N, Wang YD, Wang YS (2019) Linear β-cyclodextrin polymer functionalized multiwalled carbon nanotubes as nanoadsorbent for highly effective removal of U (VI) from aqueous solution based on inner-sphere surface complexation. Ind Eng Chem Res 58(10):4074–4083
189. Bhatia D, Datta D (2019) Removal of bisphenol—a using amine-modified magnetic multiwalled carbon nanotubes: batch and column studies. J Chem Eng Data 64(6):2877–2887
190. Ding Z, Yang H, Du M, Ruan X, Luo J, Chen S, Li D (2019) Efficient adsorption of Cu (II) Ions by a laminar nanocomposite of multi-walled carbon nanotubes coupled with fungal mycelium in aqueous solution. Nanosci Nanotechnol Lett 11(10):1366–1374
191. Kapoor N, Ameta R, Ameta SC (2019) Degradation of evans blue using multi-walled carbon nanotubes (MWCNTs)–barium chromate composite. J Nanosci Technol 20:662–665
192. Kamaraj R, Vasudevan S (2015) Decontamination of selenate from aqueous solution by oxidized multi-walled carbon nanotubes. Powder Technol 274:268–275
193. Ren X, Li J, Tan X, Wang X (2013) Comparative study of graphene oxide, activated carbon and carbon nanotubes as adsorbents for copper decontamination. Dalton Trans 42(15):5266–5274
194. Prola LD, Machado FM, Bergmann CP, de Souza FE, Gally CR, Lima EC, Calvete T (2013) Adsorption of Direct Blue 53 dye from aqueous solutions by multi-walled carbon nanotubes and activated carbon. J Environ Manage 130:166–175
195. Mishra AK, Arockiadoss T, Ramaprabhu S (2010) Study of removal of azo dye by functionalized multi walled carbon nanotubes. Chem Eng J 162(3):1026–1034
196. Moussavi SP, Ehrampoush MH, Mahvi AH, Rahimi S, Ahmadian M (2014) Efficiency of multiwalled carbon nanotubes in adsorbing humic acid from aqueous solutions. Asian J Chem 26(3):821
197. Oyetade OA, Skelton AA, Nyamori VO, Jonnalagadda SB, Martincigh BS (2017) Experimental and DFT studies on the selective adsorption of Pb2+ and Zn2+ from aqueous solution by nitrogen-functionalized multiwalled carbon nanotubes. Sep Purif Technol 188:174–187
198. Chen B, Zhu Z, Ma J, Yang M, Hong J, Hu X, Chen J (2014) One-pot, solid-phase synthesis of magnetic multiwalled carbon nanotube/iron oxide composites and their application in arsenic removal. J Colloid Interface Sci 434:9–17
199. Ansari MO, Kumar R, Ansari SA, Ansari SP, Barakat MA, Alshahrie A, Cho MH (2017) Anion selective pTSA doped polyaniline@ graphene oxide-multiwalled carbon nanotube composite for Cr (VI) and Congo red adsorption. J Colloid Interface Sci 496:407–415

200. Akl MA, Abou-Elanwar AM (2015) Adsorption studies of cd (II) from water by acid modified multiwalled carbon nanotubes. J Nanomed Nanotechnol 6(6):1
201. Reza Sohrabi M, Mansouriieh N, Khosravi M, Zolghadr M (2015) Removal of diazo dye Direct Red 23 from aqueous solution using zero-valent iron nanoparticles immobilized on multi-walled carbon nanotubes. Water Sci Technol 71(9):1367–1374
202. Huang H, Yu J, Jiang X (2014) Preparation of magnetic oxidized multi-walled carbon nanotubes for the adsorption of rhodamine b in aqueous solution. NANO 9(08):1450093
203. Machado FM, Bergmann CP, Lima EC, Adebayo MA, Fagan SB (2014) Adsorption of a textile dye from aqueous solutions by carbon nanotubes. Mater Res 17:153–160
204. Yang S, Guo Z, Sheng G, Wang X (2012) Application of a novel plasma-induced CD/MWCNT/iron oxide composite in zinc decontamination. Carbohyd Polym 90(2):1100–1105
205. Zhou S, Shao Y, Gao N, Deng J, Tan C (2013) Equilibrium, kinetic, and thermodynamic studies on the adsorption of triclosan onto multi-walled carbon nanotubes. Clean: Soil, Air, Water 41(6):539–547
206. Jiang L, Yu H, Zhou X, Hou X, Zou Z, Li S, Yao X (2016) Preparation, characterization, and adsorption properties of magnetic multi-walled carbon nanotubes for simultaneous removal of lead (II) and zinc (II) from aqueous solutions. Desalin Water Treat 57(39):18446–18462
207. Hayati F, Isari AA, Anvaripour B, Fattahi M, Kakavandi B (2020) Ultrasound-assisted photocatalytic degradation of sulfadiazine using MgO@ CNT heterojunction composite: effective factors, pathway and biodegradability studies. Chem Eng J 381:122636
208. Mahmoodi NM (2014) Synthesis of magnetic carbon nanotube and photocatalytic dye degradation ability. Environ Monit Assess 186(9):5595–5604
209. Feng K, Song B, Li X, Liao F, Gong J (2019) Enhanced photocatalytic performance of magnetic multi-walled carbon nanotubes/cerium dioxide nanocomposite. Ecotoxicol Environ Saf 171:587–593
210. Cano OA, González CR, Paz JH, Madrid PA, Casillas PG, Hernández AM, Pérez CM (2017) Catalytic activity of palladium nanocubes/multiwalled carbon nanotubes structures for methyl orange dye removal. Catal Today 282:168–173
211. Mahmoodi NM (2013) Photodegradation of dyes using multiwalled carbon nanotube and ferrous ion. J Environ Eng 139(11):1368–1374
212. Elsagh A, Moradi O, Fakhri A, Najafi F, Alizadeh R, Haddadi V (2017) Evaluation of the potential cationic dye removal using adsorption by graphene and carbon nanotubes as adsorbents surfaces. Arab J Chem 10:S2862–S2869
213. Ghaedi M, Hassanzadeh A, Kokhdan SN (2011) Multiwalled carbon nanotubes as adsorbents for the kinetic and equilibrium study of the removal of alizarin red S and morin. J Chem Eng Data 56(5):2511–2520
214. Bahgat M, Farghali AA, El Rouby WMA, Khedr MH (2011) Synthesis and modification of multi-walled carbon nano-tubes (MWCNTs) for water treatment applications. J Anal Appl Pyrol 92(2):307–313
215. Ghaedi M, Shokrollahi A, Hossainian H, Kokhdan SN (2011) Comparison of activated carbon and multiwalled carbon nanotubes for efficient removal of eriochrome cyanine R (ECR): kinetic, isotherm, and thermodynamic study of the removal process. J Chem Eng Data 56(7):3227–3235
216. Ghaedi M, Shokrollahi A, Tavallali H, Shojaiepoor F, Keshavarz B, Hossainian H, Purkait MK (2011) Activated carbon and multiwalled carbon nanotubes as efficient adsorbents for removal of arsenazo (III) and methyl red from waste water. Toxicol Environ Chem 93(3):438–449
217. Machado FM, Bergmann CP, Fernandes TH, Lima EC, Royer B, Calvete T, Fagan SB (2011) Adsorption of reactive red M-2BE dye from water solutions by multi-walled carbon nanotubes and activated carbon. J Hazard Mater 192(3):1122–1131
218. Jahangiri-Rad M, Nadafi K, Mesdaghinia A, Nabizadeh R, Younesian M, Rafiee M (2013) Sequential study on reactive blue 29 dye removal from aqueous solution by peroxy acid and single wall carbon nanotubes: experiment and theory. Iran J Environ Health Sci Eng 10(1):5
219. Ma J, Yu F, Zhou L, Jin L, Yang M, Luan J, Chen J (2012) Enhanced adsorptive removal of methyl orange and methylene blue from aqueous solution by alkali-activated multiwalled carbon nanotubes. ACS Appl Mater Interfaces 4(11):5749–5760
220. Bazrafshan E, Mostafapour FK, Hosseini AR, Raksh Khorshid A, Mahvi AH (2013) Decolorisation of reactive red 120 dye by using single-walled carbon nanotubes in aqueous solutions. J Chem 20:13

221. Zaib Q, Khan IA, Saleh NB, Flora JR, Park YG, Yoon Y (2012) Removal of bisphenol A and 17β-estradiol by single-walled carbon nanotubes in aqueous solution: adsorption and molecular modeling. Water Air Soil Pollut 223(6):3281–3293
222. Jafari M, Aghamiri SF (2011) Evaluation of carbon nanotubes as solid-phase extraction sorbent for the removal of cephalexin from aqueous solution. Desalin Water Treat 28(1–3):55–58
223. Zhang L, Song X, Liu X, Yang L, Pan F, Lv J (2011) Studies on the removal of tetracycline by multi-walled carbon nanotubes. Chem Eng J 178:26–33
224. Sotelo JL, Rodríguez AR, Mateos MM, Hernández SD, Torrellas SA, Rodríguez JG (2012) Adsorption of pharmaceutical compounds and an endocrine disruptor from aqueous solutions by carbon materials. J Environ Sci Health B 47(7):640–652
225. Moradi O, Fakhri A, Adami S, Adami S (2013) Isotherm, thermodynamic, kinetics, and adsorption mechanism studies of Ethidium bromide by single-walled carbon nanotube and carboxylate group functionalized single-walled carbon nanotube. J Colloid Interface Sci 395:224–229
226. Xu J, Sheng T, Hu Y, Baig SA, Lv X, Xu X (2013) Adsorption–dechlorination of 2, 4-dichlorophenol using two specified MWCNTs-stabilized Pd/Fe nanocomposites. Chem Eng J 219:162–173
227. Mamba G, Mbianda XY, Govender PP (2013) Phosphorylated multiwalled carbon nanotube-cyclodextrin polymer: synthesis, characterisation and potential application in water purification. Carbohyd Polym 98(1):470–476
228. Yu F, Wu Y, Li X, Ma J (2012) Kinetic and thermodynamic studies of toluene, ethylbenzene, and m-xylene adsorption from aqueous solutions onto KOH-activated multiwalled carbon nanotubes. J Agric Food Chem 60(50):12245–12253
229. Chakraborty A, Deva D, Sharma A, Verma N (2011) Adsorbents based on carbon microfibers and carbon nanofibers for the removal of phenol and lead from water. J Colloid Interface Sci 359(1):228–239
230. Li X, Chen S, Fan X, Quan X, Tan F, Zhang Y, Gao J (2015) Adsorption of ciprofloxacin, bisphenol and 2-chlorophenol on electrospun carbon nanofibers: in comparison with powder activated carbon. J Colloid Interface Sci 447:120–127
231. Al-Khaldi FA, Abusharkh B, Khaled M, Atieh MA, Nasser MS, Saleh TA, Gupta VK (2015) Adsorptive removal of cadmium (II) ions from liquid phase using acid modified carbon-based adsorbents. J Mol Liq 204:255–263
232. Babaei AA, Lima EC, Takdastan A, Alavi N, Goudarzi G, Vosoughi M, Shirmardi M (2016) Removal of tetracycline antibiotic from contaminated water media by multi-walled carbon nanotubes: operational variables, kinetics, and equilibrium studies. Water Sci Technol 74(5):1202–1216
233. Balarak D, Mahdavi Y, Maleki A, Daraei H, Sadeghi S (2016) Studies on the removal of amoxicillin by single walled carbon nanotubes. J Pharm Res Int 20:1–9
234. Deng J, Shao Y, Gao N, Deng Y, Tan C, Zhou S, Hu X (2012) Multiwalled carbon nanotubes as adsorbents for removal of herbicide diuron from aqueous solution. Chem Eng J 193:339–347
235. Li X, Zhao H, Quan X, Chen S, Zhang Y, Yu H (2011) Adsorption of ionizable organic contaminants on multi-walled carbon nanotubes with different oxygen contents. J Hazard Mater 186(1):407–415
236. Mohammadi A, Kazemipour M, Ranjbar H, Walker RB, Ansari M (2015) Amoxicillin removal from aqueous media using multi-walled carbon nanotubes. Fullerenes Nanotubes Carbon Nanostruct 23(2):165–169
237. Liu H, Zhang J, Bao N, Cheng C, Ren L, Zhang C (2012) Textural properties and surface chemistry of lotus stalk-derived activated carbons prepared using different phosphorus oxyacids: adsorption of trimethoprim. J Hazard Mater 235:367–375
238. Talreja N, Kumar D, Verma N (2014) Removal of hexavalent chromium from water using Fe-grown carbon nanofibers containing porous carbon microbeads. J Water Process Eng 3:34–45
239. Umukoro EH, Peleyeju MG, Ngila JC, Arotiba OA (2017) Towards wastewater treatment: photo-assisted electrochemical degradation of 2-nitrophenol and orange II dye at a tungsten trioxide-exfoliated graphite composite electrode. Chem Eng J 317:290–301
240. Wu S, He W, Yang W, Ye Y, Huang X, Logan BE (2017) Combined carbon mesh and small graphite fiber brush anodes to enhance and stabilize power generation in microbial fuel cells treating domestic wastewater. J Power Sources 356:348–355
241. Rodrigues TM, Kavashima L, Adas EG, Antoniassi B, Chaves MR (2016) Adsorption of rhodamine B from aqueous effluents on graphite from spent lithium-ion battery anode. Int J Res Eng Sci 4:27–36

242. Muddemann T, Haupt D, Engelke M, Sievers M, Fischer A, Kiefer C, Kunz U (2020) Combination of magnetically actuated flexible graphite–polymer composite cathode and boron-doped diamond anode for electrochemical water softening or wastewater treatment. Electrochim Acta 354:136729
243. Zhao T, Yao Y, Wang M, Chen R, Yu Y, Wu F, Zhang C (2017) Preparation of MnO2-modified graphite sorbents from spent Li-ion batteries for the treatment of water contaminated by lead, cadmium, and silver. ACS Appl Mater Interfaces 9(30):25369–25376
244. Zamani S, Salem S (2021) Couple of graphene oxide and functionalized carbon nanotubes for dye degradation enhancement of anatase under visible light and solar irradiation. Environ Sci Pollut Res 20:1–14
245. Parashar M, Shukla VK, Singh R (2020) Metal oxides nanoparticles via sol–gel method: a review on synthesis, characterization and applications. J Mater Sci Mater Electron 31(5):3729–3749
246. Nagarajan S, Skillen NC, Fina F, Zhang G, Randorn C, Lawton LA, Robertson PK (2017) Comparative assessment of visible light and UV active photocatalysts by hydroxyl radical quantification. J Photochem Photobiol A 334:13–19
247. Xiang Q, Yu J, Wong PK (2011) Quantitative characterization of hydroxyl radicals produced by various photocatalysts. J Colloid Interface Sci 357(1):163–167
248. Wang Z, Gao M, Li X, Ning J, Zhou Z, Li G (2020) Efficient adsorption of methylene blue from aqueous solution by graphene oxide modified persimmon tannins. Mater Sci Eng C 108:110196
249. Firdaus RM, Rosli NIM, Ghanbaja J, Vigolo B, Mohamed AR (2019) Enhanced adsorption of methylene blue on chemically modified graphene nanoplatelets thanks to favorable interactions. J Nanopart Res 21(12):257
250. Karimi-Maleh H, Shafieizadeh M, Taher MA, Opoku F, Kiarii EM, Govender PP, Orooji Y (2020) The role of magnetite/graphene oxide nano-composite as a high-efficiency adsorbent for removal of phenazopyridine residues from water samples, an experimental/theoretical investigation. J Mol Liq 298:112040
251. Balasubramani K, Sivarajasekar N, Naushad M (2020) Effective adsorption of antidiabetic pharmaceutical (metformin) from aqueous medium using graphene oxide nanoparticles: equilibrium and statistical modelling. J Mol Liq 301:112426
252. Ikram M, Ali S, Aqeel M, Ul-Hamid A, Imran M, Haider J, Ali S (2020) Reduced graphene oxide nanosheets doped by Cu with highly efficient visible light photocatalytic behavior. J Alloys Compds 20:155588
253. Barakat MA, Anjum M, Kumar R, Alafif ZO, Oves M, Ansari MO (2020) Design of ternary Ni (OH) 2/graphene oxide/TiO2 nanocomposite for enhanced photocatalytic degradation of organic, microbial contaminants, and aerobic digestion of dairy wastewater. J Clean Prod 258:120588
254. Modi A, Bellare J (2020) Efficient removal of 2, 4-dichlorophenol from contaminated water and alleviation of membrane fouling by high flux polysulfone-iron oxide/graphene oxide composite hollow fiber membranes. J Water Process Eng 33:101113
255. Tantubay K, Das P, Baskey M (2020) Ternary reduced graphene oxide–CuO/ZnO nanocomposite as a recyclable catalyst with enhanced reducing capability. J Environ Chem Eng 103:818
256. Salawudeen AO, Tawabini BS, Al-Shaibani AM, Saleh TA (2020) Poly (2-hydroxyethyl methacrylate) grafted graphene oxide for cadmium removal from water with interaction mechanisms. Environ Nanotechnol Monit Manage 100:288
257. Zong P, Cheng Y, Wang S, Wang L (2020) Simultaneous removal of Cd (II) and phenol pollutions through magnetic graphene oxide nanocomposites coated polyaniline using low temperature plasma technique. Int J Hydrog Energy 20:20
258. Kalita H, Tyagi H, Aslam M (2020) Surface-tailored graphene oxide paper: an efficient filter for dye pollutants. Environ Sci Water Res Technol 6(4):963–975
259. Aboelfetoh EF, Gemeay AH, El-Sharkawy RG (2020) Effective disposal of methylene blue using green immobilized silver nanoparticles on graphene oxide and reduced graphene oxide sheets through one-pot synthesis. Environ Monit Assess 192:1–20
260. Bao S, Yang W, Wang Y, Yu Y, Sun Y (2020) One-pot synthesis of magnetic graphene oxide composites as an efficient and recoverable adsorbent for Cd (II) and Pb (II) removal from aqueous solution. J Hazard Mater 381:120914
261. Ikram M, Raza A, Imran M, Ul-Hamid A, Shahbaz A, Ali S (2020) Hydrothermal synthesis of silver decorated reduced graphene oxide (rGO) nanoflakes with effective photocatalytic activity for wastewater treatment. Nanosc Res Lett 15:1–11

262. Chang S, Zhang Q, Lu Y, Wu S, Wang W (2020) High-efficiency and selective adsorption of organic pollutants by magnetic CoFe2O4/graphene oxide adsorbents: experimental and molecular dynamics simulation study. Sep Purif Technol 238:116400
263. Yang X, Guo N, Yu Y, Li H, Xia H, Yu H (2020) Synthesis of magnetic graphene oxide-titanate composites for efficient removal of Pb (II) from wastewater: performance and mechanism. J Environ Manage 256:109943
264. Li Y, Liu S, Wang C, Ying Z, Huo M, Yang W (2020) Effective column adsorption of triclosan from pure water and wastewater treatment plant effluent by using magnetic porous reduced graphene oxide. J Hazard Mater 386:121942
265. He J, Ni F, Cui A, Chen X, Deng S, Shen F, Tian D (2020) New insight into adsorption and co-adsorption of arsenic and tetracycline using a Y-immobilized graphene oxide-alginate hydrogel: adsorption behaviours and mechanisms. Sci Total Environ 701:134363
266. Ulucan-Altuntas K, Debik E, Ustundag CB, Guven MD, Gocen KA (2020) Effect of visible light on the removal of trichloromethane by graphene oxide. Diamond Relat Mater 10:7814
267. Chen H, Liu T, Meng Y, Cheng Y, Lu J, Wang H (2020) Novel graphene oxide/aminated lignin aerogels for enhanced adsorption of malachite green in wastewater. Colloids Surf A Physicochem Eng Aspects 20:125281
268. Giwa A, Hasan SW (2020) Novel polyethersulfone-functionalized graphene oxide (PES-fGO) mixed matrix membranes for wastewater treatment. Sep Purif Technol 241:116735
269. Lee J, Park JA, Kim HG, Lee JH, Cho SH, Choi K, Choi JW (2020) Most suitable amino silane molecules for surface functionalization of graphene oxide toward hexavalent chromium adsorption. Chemosphere 20:126387
270. Elanchezhiyan SS, Prabhu SM, Kim Y, Park CM (2020) Lanthanum-substituted bimetallic magnetic materials assembled carboxylate-rich graphene oxide nanohybrids as highly efficient adsorbent for perfluorooctanoic acid adsorption from aqueous solutions. Appl Surf Sci 509:144716
271. Dong C, Lu J, Qiu B, Shen B, Xing M, Zhang J (2018) Developing stretchable and graphene-oxide-based hydrogel for the removal of organic pollutants and metal ions. Appl Catal B 222:146–156
272. Ganesan V, Louis C, Damodaran SP (2018) Graphene oxide-wrapped magnetite nanoclusters: a recyclable functional hybrid for fast and highly efficient removal of organic dyes from wastewater. J Environ Chem Eng 6(2):2176–2190
273. Hao J, Ji L, Li C, Hu C, Wu K (2018) Rapid, efficient and economic removal of organic dyes and heavy metals from wastewater by zinc-induced in-situ reduction and precipitation of graphene oxide. J Taiwan Inst Chem Eng 88:137–145
274. Fang Z, Hu Y, Wu X, Qin Y, Cheng J, Chen Y, Li H (2018) A novel magnesium ascorbyl phosphate graphene-based monolith and its superior adsorption capability for bisphenol A. Chem Eng J 334:948–956
275. Zhang Y, Cao B, Zhao L, Sun L, Gao Y, Li J, Yang F (2018) Biochar-supported reduced graphene oxide composite for adsorption and coadsorption of atrazine and lead ions. Appl Surf Sci 427:147–155
276. Zhang W, Chen J, Hu Y, Fang Z, Cheng J, Chen Y (2018) Adsorption characteristics of tetrabromobisphenol A onto sodium bisulfite reduced graphene oxide aerogels. Colloids Surf A 538:781–788
277. Abdul G, Zhu X, Chen B (2017) Structural characteristics of biochar-graphene nanosheet composites and their adsorption performance for phthalic acid esters. Chem Eng J 319:9–20
278. Jiang LH, Liu YG, Zeng GM, Xiao FY, Hu XJ, Hu X, Tan XF (2016) Removal of 17β-estradiol by few-layered graphene oxide nanosheets from aqueous solutions: external influence and adsorption mechanism. Chem Eng J 284:93–102
279. Tanhaei M, Mahjoub AR, Safarifard V (2018) Sonochemical synthesis of amide-functionalized metal-organic framework/graphene oxide nanocomposite for the adsorption of methylene blue from aqueous solution. Ultrason Sonochem 41:189–195
280. Wei XN, Ou CL, Guan XX, Peng ZK, Zheng XC (2019) Facile assembly of CdS-reduced graphene oxide heterojunction with enhanced elimination performance for organic pollutants in wastewater. Appl Surf Sci 469:666–673
281. Lingamdinne LP, Koduru JR, Chang YY, Karri RR (2018) Process optimization and adsorption modeling of Pb (II) on nickel ferrite-reduced graphene oxide nano-composite. J Mol Liq 250:202–211
282. Naeem H, Ajmal M, Qureshi RB, Muntha ST, Farooq M, Siddiq M (2019) Facile synthesis of graphene oxide–silver nanocomposite for decontamination of water from multiple pollutants by adsorption, catalysis and antibacterial activity. J Environ Manage 230:199–211

283. Wang J, Huang T, Zhang L, Yu QJ, Hou LA (2018) Dopamine crosslinked graphene oxide membrane for simultaneous removal of organic pollutants and trace heavy metals from aqueous solution. Environ Technol 39(23):3055–3065
284. Mangalam J, Kumar M, Sharma M, Joshi M (2019) High adsorptivity and visible light assisted photocatalytic activity of silver/reduced graphene oxide (Ag/rGO) nanocomposite for wastewater treatment. Nano-Struct Nano-Objects 17:58–66
285. Naeem H, Ajmal M, Muntha S, Ambreen J, Siddiq M (2018) Synthesis and characterization of graphene oxide sheets integrated with gold nanoparticles and their applications to adsorptive removal and catalytic reduction of water contaminants. RSC Adv 8(7):3599–3610
286. Mohammadi Nodeh MK, Radfard M, Zardari LA, Rashidi Nodeh H (2018) Enhanced removal of naproxen from wastewater using silica magnetic nanoparticles decorated onto graphene oxide; parametric and equilibrium study. Sep Sci Technol 53(15):2476–2485
287. Sohni S, Gul K, Ahmad F, Ahmad I, Khan A, Khan N, Bahadar Khan S (2018) Highly efficient removal of acid red-17 and bromophenol blue dyes from industrial wastewater using graphene oxide functionalized magnetic chitosan composite. Polym Compos 39(9):3317–3328
288. Lin Z, Weng X, Ma L, Sarkar B, Chen Z (2019) Mechanistic insights into Pb (II) removal from aqueous solution by green reduced graphene oxide. J Colloid Interface Sci 550:1–9
289. Catherine HN, Ou MH, Manu B, Shih YH (2018) Adsorption mechanism of emerging and conventional phenolic compounds on graphene oxide nanoflakes in water. Sci Total Environ 635:629–638
290. Hosseinzadeh H, Ramin S (2018) Effective removal of copper from aqueous solutions by modified magnetic chitosan/graphene oxide nanocomposites. Int J Biol Macromol 113:859–868
291. Ramezanzadeh M, Asghari M, Ramezanzadeh B, Bahlakeh G (2018) Fabrication of an efficient system for Zn ions removal from industrial wastewater based on graphene oxide nanosheets decorated with highly crystalline polyaniline nanofibers (GO-PANI): experimental and ab initio quantum mechanics approaches. Chem Eng J 337:385–397
292. White RL, White CM, Turgut H, Massoud A, Tian ZR (2018) Comparative studies on copper adsorption by graphene oxide and functionalized graphene oxide nanoparticles. J Taiwan Inst Chem Eng 85:18–28
293. Alwan SH, Alshamsi HAH, Jasim LS (2018) Rhodamine B removal on A-rGO/cobalt oxide nanoparticles composite by adsorption from contaminated water. J Mol Struct 1161:356–365
294. Hemmati S, Mehrazin L, Ghorban H, Garakani SH, Mobaraki TH, Mohammadi P, Veisi H (2018) Green synthesis of Pd nanoparticles supported on reduced graphene oxide, using the extract of Rosa canina fruit, and their use as recyclable and heterogeneous nanocatalysts for the degradation of dye pollutants in water. RSC Adv 8(37):21020–21028
295. Soleimani K, Tehrani AD, Adeli M (2018) Bioconjugated graphene oxide hydrogel as an effective adsorbent for cationic dyes removal. Ecotoxicol Environ Saf 147:34–42
296. Guo H, Jiao T, Zhang Q, Guo W, Peng Q, Yan X (2015) Preparation of graphene oxide-based hydrogels as efficient dye adsorbents for wastewater treatment. Nanosc Res Lett 10(1):272
297. Zhang J, Azam MS, Shi C, Huang J, Yan B, Liu Q, Zeng H (2015) Poly (acrylic acid) functionalized magnetic graphene oxide nanocomposite for removal of methylene blue. RSC Adv 5(41):32272–32282
298. Xiao W, Yan B, Zeng H, Liu Q (2016) Dendrimer functionalized graphene oxide for selenium removal. Carbon 105:655–664
299. Gopalakrishnan A, Krishnan R, Thangavel S, Venugopal G, Kim SJ (2015) Removal of heavy metal ions from pharma-effluents using graphene-oxide nanosorbents and study of their adsorption kinetics. J Ind Eng Chem 30:14–19
300. Yang X, Qin J, Jiang Y, Chen K, Yan X, Zhang D, Tang H (2015) Fabrication of P25/Ag3PO4/graphene oxide heterostructures for enhanced solar photocatalytic degradation of organic pollutants and bacteria. Appl Catal B 166:231–240
301. Heidarizad M, Şengör SS (2016) Synthesis of graphene oxide/magnesium oxide nanocomposites with high-rate adsorption of methylene blue. J Mol Liq 224:607–617
302. Zambianchi M, Durso M, Liscio A, Treossi E, Bettini C, Capobianco ML, Brucale M (2017) Graphene oxide doped polysulfone membrane adsorbers for the removal of organic contaminants from water. Chem Eng J 326:130–140
303. Dong S, Sun Y, Wu J, Wu B, Creamer AE, Gao B (2016) Graphene oxide as filter media to remove levofloxacin and lead from aqueous solution. Chemosphere 150:759–764

304. Xing R, Wang W, Jiao T, Ma K, Zhang Q, Hong W, Peng Q (2017) Bioinspired polydopamine sheathed nanofibers containing carboxylate graphene oxide nanosheet for high-efficient dyes scavenger. ACS Sustain Chem Eng 5(6):4948–4956
305. Russo P, D'Urso L, Hu A, Zhou N, Compagnini G (2015) In liquid laser treated graphene oxide for dye removal. Appl Surf Sci 348:85–91
306. Azizi A, Torabian A, Moniri E, Hassani AH, Ahmad Panahi H (2016) Adsorption performance of modified graphene oxide nanoparticles for the removal of toluene, ethylbenzene, and xylenes from aqueous solution. Desalin Water Treat 57(59):28806–28821
307. Mahmoodi NM, Ghezelbash M, Shabanian M, Aryanasab F, Saeb MR (2017) Efficient removal of cationic dyes from colored wastewaters by dithiocarbamate-functionalized graphene oxide nanosheets: from synthesis to detailed kinetics studies. J Taiwan Inst Chem Eng 81:239–246
308. Gul K, Sohni S, Waqar M, Ahmad F, Norulaini NN, AK, M. O. (2016) Functionalization of magnetic chitosan with graphene oxide for removal of cationic and anionic dyes from aqueous solution. Carbohyd Polym 152:520–531
309. Chen G, Sun M, Wei Q, Zhang Y, Zhu B, Du B (2013) Ag3PO4/graphene-oxide composite with remarkably enhanced visible-light-driven photocatalytic activity toward dyes in water. J Hazard Mater 244:86–93
310. He K, Zeng G, Chen A, Huang Z, Peng M, Huang T, Chen G (2019) Graphene hybridized polydopamine-kaolin composite as effective adsorbent for methylene blue removal. Compos B Eng 161:141–149
311. Castro E, Garcia AH, Zavala G, Echegoyen L (2017) Fullerenes in biology and medicine. J Mater Chem B 5(32):6523–6535
312. Clancy AJ, Bayazit MK, Hodge SA, Skipper NT, Howard CA, Shaffer MS (2018) Charged carbon nanomaterials: redox chemistries of fullerenes, carbon nanotubes, and graphenes. Chem Rev 118(16):7363–7408
313. Semenov KN, Andrusenko EV, Charykov NA, Litasova EV, Panova GG, Penkova AV, Piotrovskiy LB (2017) Carboxylated fullerenes: physico-chemical properties and potential applications. Prog Solid State Chem 47:19–36
314. Wu ZY, Xu YJ, Huang LJ, Zhang QX, Tang DL (2021) Fullerene-cored star-shaped polyporphyrin-incorporated TiO2 as photocatalysts for the enhanced degradation of rhodamine B. J Environ Chem Eng 20:106142
315. Elessawy NA, Elnouby M, Gouda MH, Hamad HA, Taha NA, Gouda M, Eldin MSM (2020) Ciprofloxacin removal using magnetic fullerene nanocomposite obtained from sustainable PET bottle wastes: adsorption process optimization, kinetics, isotherm, regeneration and recycling studies. Chemosphere 239:124728
316. Mahdavian L (2020) Efficiency evaluating of modified fullerene nanofiltration on removal of heavy metals from aqueous media. J Res Many-body Syst 10(2):85–95
317. Ju L, Wu P, Lai X, Yang S, Gong B, Chen M, Zhu N (2017) Synthesis and characterization of Fullerene modified ZnAlTi-LDO in photo-degradation of Bisphenol A under simulated visible light irradiation. Environ Pollut 228:234–244
318. Cai Q, Hu Z, Zhang Q, Li B, Shen Z (2017) Fullerene (C60)/CdS nanocomposite with enhanced photocatalytic activity and stability. Appl Surf Sci 403:151–158
319. Meng ZD, Zhang FJ, Zhu L, Park CY, Ghosh T, Choi JG, Oh WC (2012) Synthesis and characterization of M-fullerene/TiO2 photocatalysts designed for degradation azo dye. Mater Sci Eng C 32(8):2175–2182
320. Velzeboer I, Kwadijk CJAF, Koelmans AA (2014) Strong sorption of PCBs to nanoplastics, microplastics, carbon nanotubes, and fullerenes. Environ Sci Technol 48(9):4869–4876
321. Bai W, Krishna V, Wang J, Moudgil B, Koopman B (2012) Enhancement of nano titanium dioxide photocatalysis in transparent coatings by polyhydroxy fullerene. Appl Catal B 125:128–135
322. Zhou P, Huo X, Zhang J, Liu Y, Cheng F, Cheng X, Zhang Y (2020) Visible light induced acceleration of Fe (III)/Fe (II) cycles for enhancing phthalate degradation in C60 fullerenol modified Fe (III)/peroxymonosulfate process. Chem Eng J 387:124126
323. Wang Y, Zhou P, Wang Q, Huo X, Huang X, Ye Q, Zhang J (2020) Fullerol mediated enhancement of chloramphenicol degradation in Fe (III)/H2O2 system by accelerating Fe (III)/Fe (II) cycle via a non-photochemical pathway. Chem Eng J 402:126176
324. Xu T, Zhu R, Liu J, Zhou Q, Zhu J, Liang X, He H (2016) Fullerol modification ferrihydrite for the degradation of acid red 18 under simulated sunlight irradiation. J Mol Catal A Chem 424:393–401

325. Zhou DB, Sheng X, Han F, Hu YY, Ding L, Lv YL, Zheng P (2018) Magnetic solid-phase extraction based on [60] fullerene functionalization of magnetic nanoparticles for the determination of sixteen polycyclic aromatic hydrocarbons in tea samples. J Chromatogr A 1578:53–60
326. Grandcolas M, Ye J, Miyazawa K (2014) Titania nanotubes and fullerenes C60 assemblies and their photocatalytic activity under visible light. Ceram Int 40(1):1297–1302
327. Justh N, Firkala T, László K, Lábár J, Szilágyi IM (2017) Photocatalytic C60-amorphous TiO2 composites prepared by atomic layer deposition. Appl Surf Sci 419:497–502
328. Katsumata KI, Matsushita N, Okada K (2012) Preparation of TiO2-fullerene composites and their photocatalytic activity under visible light. Int J Photoenergy 20:12
329. Chai B, Liao X, Song F, Zhou H (2014) Fullerene modified C 3 N 4 composites with enhanced photocatalytic activity under visible light irradiation. Dalton Trans 43(3):982–989
330. Liu J, Jiang J, Meng Y, Aihemaiti A, Xu Y, Xiang H, Chen X (2020) Preparation, environmental application and prospect of biochar-supported metal nanoparticles: a review. J Hazard Mater 388:122026
331. Ali N, Ismail M, Khan A, Khan H, Haider S, Kamal T (2018) Spectrophotometric methods for the determination of urea in real samples using silver nanoparticles by standard addition and 2nd order derivative methods. Spectrochim Acta Part A Mol Biomol Spectrosc 189:110–115
332. Shah S, Din S, Khan A, Shah SA (2018) Green synthesis and antioxidant study of silver nanoparticles of root extract of Sageretia thea and its role in oxidation protection technology. J Polym Environ 26(6):2323–2332
333. Adnan MAM, Phoon BL, Julkapli NM (2020) Mitigation of pollutants by chitosan/metallic oxide photocatalyst: a review. J Clean Prod 1:21190
334. Hassan M, Naidu R, Du J, Liu Y, Qi F (2020) Critical review of magnetic biosorbents: their preparation, application, and regeneration for wastewater treatment. Sci Total Environ 702:134893
335. Kalra A, Gupta A (2020) Recent advances in decolourization of dyes using iron nanoparticles: a mini review. Mater Today Proc 20:20
336. Ou JH, Sheu YT, Tsang DC, Sun YJ, Kao CM (2020) Application of iron/aluminum bimetallic nanoparticle system for chromium-contaminated groundwater remediation. Chemosphere 127:158
337. Mustapha S, Ndamitso MM, Abdulkareem AS, Tijani JO, Shuaib DT, Ajala AO, Mohammed AK (2020) Application of TiO 2 and ZnO nanoparticles immobilized on clay in wastewater treatment: a review. Appl Water Sci 10(1):1–36
338. Ajormal F, Moradnia F, Taghavi Fardood S, Ramazani A (2020) Zinc ferrite nanoparticles in photo-degradation of dye: mini-review. J Chem Rev 20:20
339. Ali A, Hira Zafar MZ, UlHaq I, Phull AR, Ali JS, Hussain A (2016) Synthesis, characterization, applications, and challenges of iron oxide nanoparticles. Nanotechnol Sci Appl 9:49
340. Shipley HJ, Engates KE, Guettner AM (2011) Study of iron oxide nanoparticles in soil for remediation of arsenic. J Nanopart Res 13(6):2387–2397
341. Cheng Z, Tan ALK, Tao Y, Shan D, Ting KE, Yin XJ (2012) Synthesis and characterization of iron oxide nanoparticles and applications in the removal of heavy metals from industrial wastewater. Int J Photoenergy 20:12
342. Yoon SY, Lee CG, Park JA, Kim JH, Kim SB, Lee SH, Choi JW (2014) Kinetic, equilibrium and thermodynamic studies for phosphate adsorption to magnetic iron oxide nanoparticles. Chem Eng J 236:341–347
343. Ali I, Peng C, Naz I, Khan ZM, Sultan M, Islam T, Abbasi IA (2017) Phytogenic magnetic nanoparticles for wastewater treatment: a review. RSC Adv 7(64):40158–40178
344. Kefeni KK, Mamba BB, Msagati TA (2017) Application of spinel ferrite nanoparticles in water and wastewater treatment: a review. Sep Purif Technol 188:399–422
345. Bhateria R, Singh R (2019) A review on nanotechnological application of magnetic iron oxides for heavy metal removal. J Water Process Eng 31:100845
346. Song X, Ren C, Zhao Q, Su B (2020) Simultaneous removal of Cr (VI) and triclosan from aqueous solutions through Fe3O4 magnetic nanoscale-activated persulfate oxidation. Chem Eng J 381:122586
347. Rispoli F, Angelov A, Badia D, Kumar A, Seal S, Shah V (2010) Understanding the toxicity of aggregated zero valent copper nanoparticles against *Escherichia coli*. J Hazard Mater 180(1–3):212–216
348. D'Cruz B, Madkour M, Amin MO, Al-Hetlani E (2020) Efficient and recoverable magnetic AC-Fe3O4 nanocomposite for rapid removal of promazine from wastewater. Mater Chem Phys 240:122109

349. Magnacca G, Allera A, Montoneri E, Celi L, Benito DE, Gagliardi LG, Carlos L (2014) Novel magnetite nanoparticles coated with waste-sourced biobased substances as sustainable and renewable adsorbing materials. ACS Sustain Chem Eng 2(6):1518–1524
350. Andhare DD, Patade SR, Kounsalye JS, Jadhav KM (2020) Effect of Zn doping on structural, magnetic and optical properties of cobalt ferrite nanoparticles synthesized via. Co-precipitation method. Phys B Condensed Matter 583:412051
351. Giri SK, Das NN, Pradhan GC (2011) Synthesis and characterization of magnetite nanoparticles using waste iron ore tailings for adsorptive removal of dyes from aqueous solution. Colloids Surf A 389(1–3):43–49
352. Afkhami A, Moosavi R (2010) Adsorptive removal of Congo red, a carcinogenic textile dye, from aqueous solutions by maghemite nanoparticles. J Hazard Mater 174(1–3):398–403
353. Behera SK, Sahni S, Tiwari G, Rai A, Mahanty B, Vinati A, Pugazhendhi A (2020) Removal of chromium from synthetic wastewater using modified maghemite nanoparticles. Appl Sci 10(9):3181
354. Minisy IM, Zasońska BA, Petrovský E, Veverka P, Šeděnková I, Hromádková J, Bober P (2020) Poly (p-phenylenediamine)/maghemite composite as highly effective adsorbent for anionic dye removal. React Funct Polym 146:104436
355. Tadic M, Panjan M, Damnjanovic V, Milosevic I (2014) Magnetic properties of hematite (α-Fe2O3) nanoparticles prepared by hydrothermal synthesis method. Appl Surf Sci 320:183–187
356. Kefeni KK, Msagati TA, Nkambule TT, Mamba BB (2018) Synthesis and application of hematite nanoparticles for acid mine drainage treatment. J Environ Chem Eng 6(2):1865–1874
357. Saad AHA, Azzam AM, El-Wakeel ST, Mostafa BB, Abd El-latif MB (2018) Removal of toxic metal ions from wastewater using ZnO@ Chitosan core-shell nanocomposite. Environ Nanotechnol Monit Manage 9:67–75
358. Thinh NN, Hanh PTB, Hoang TV, Hoang VD, Van Khoi N, Dai Lam T (2013) Magnetic chitosan nanoparticles for removal of Cr (VI) from aqueous solution. Mater Sci Eng C 33(3):1214–1218
359. Chen D, Cheng Y, Zhou N, Chen P, Wang Y, Li K, Wang L (2020) Photocatalytic degradation of organic pollutants using TiO2-based photocatalysts: a review. J Clean Prod 121:725
360. Gopinath KP, Madhav NV, Krishnan A, Malolan R, Rangarajan G (2020) Present applications of titanium dioxide for the photocatalytic removal of pollutants from water: a review. J Environ Manage 270:110906
361. He X, Wang A, Wu P, Tang S, Zhang Y, Li L, Ding P (2020) Photocatalytic degradation of microcystin-LR by modified TiO2 photocatalysis: a review. Sci Total Environ 140:694
362. Malakootian M, Nasiri A, Amiri Gharaghani M (2020) Photocatalytic degradation of ciprofloxacin antibiotic by TiO2 nanoparticles immobilized on a glass plate. Chem Eng Commun 207(1):56–72
363. Dlamini LN, Krause RW, Kulkarni GU, Durbach SH (2011) Photodegradation of bromophenol blue with fluorinated TiO 2 composite. Appl Water Sci 1(1):19–24
364. Chen Y, Liu Y, Li Y, Wu Y, Chen Y, Liu Y, Li L (2020) Synthesis, application and mechanisms of Ferro-Manganese binary oxide in water remediation: a review. Chem Eng J 388:124313
365. Mohanta J, Dey B, Dey S (2020) Highly porous iron-zirconium binary oxide for efficient removal of congo red from water. Desalin Water Treat 20:20
366. Du Y, Wang X, Nie G, Xu L, Hu Y (2020) Enhanced phosphate removal by using La-Zr binary metal oxide nanoparticles confined in millimeter-sized anion exchanger. J Colloid Interface Sci 580:234–244
367. Ghasemipour P, Fattahi M, Rasekh B, Yazdian F (2020) Developing the ternary ZnO doped MoS 2 nanostructures grafted on CNT and reduced graphene oxide (RGO) for photocatalytic degradation of aniline. Sci Rep 10(1):1–16
368. Eniola JO, Kumar R, Al-Rashdi AA, Barakat MA (2020) Hydrothermal synthesis of structurally variable binary CuAl, MnAl and ternary CuMnAl hydroxides for oxytetracycline antibiotic adsorption. J Environ Chem Eng 8(2):103535
369. Khan ST, Ahmad F, Shahadat M, Rehman WU, Khan AM (2020) Metal and metal oxide nanoparticles for water decontamination and purification. Environ Nanotechnol Water Purif 20:151
370. Anku WW, Ama OM, Ray SS, Osifo PO (2020) Application of modified metal oxide electrodes in photoelectrochemical removal of organic pollutants from wastewater. Nanostructured metal-oxide electrode materials for water purification. Springer, Cham, pp 151–166

371. Kumar SS, Venkateswarlu P, Rao VR, Rao GN (2013) Synthesis, characterization and optical properties of zinc oxide nanoparticles. Int Nano Lett 3(1):1–6
372. Rafique M, Tahir MB, Irshad M, Nabi G, Gillani SSA, Iqbal T, Mubeen M (2020) Novel Citrus aurantifolia leaves based biosynthesis of copper oxide nanoparticles for environmental and wastewater purification as an efficient photocatalyst and antibacterial agent. Optik 20:165138
373. Safwat SM, Medhat M, Abdel-Halim H (2019) Adsorption of phenol onto aluminium oxide and zinc oxide: a comparative study with titanium dioxide. Sep Sci Technol 54(17):2840–2852
374. Ghanbari F, Ahmadi M, Gohari F (2019) Heterogeneous activation of peroxymonosulfate via nanocomposite CeO2-Fe3O4 for organic pollutants removal: the effect of UV and US irradiation and application for real wastewater. Sep Purif Technol 228:115732
375. Jadhav SA, Garud HB, Patil AH, Patil GD, Patil CR, Dongale TD, Patil PS (2019) Recent advancements in silica nanoparticles based technologies for removal of dyes from water. Colloid Interface Sci Commun 30:100181
376. Liu F, Li W, Wu D, Tian T, Wu JF, Dong ZM, Zhao GC (2020) New insight into the mechanism of peroxymonosulfate activation by nanoscaled lead-based spinel for organic matters degradation: a singlet oxygen-dominated oxidation process. J Colloid Interface Sci 20:20
377. Mohamed AK, Mahmoud ME (2020) Metoprolol beta-blocker decontamination from water by the adsorptive action of metal-organic frameworks-nano titanium oxide coated tin dioxide nanoparticles. J Mol Liquids 20:113096
378. Debnath P, Mondal NK (2020) Effective removal of congo red dye from aqueous solution using biosynthesized zinc oxide nanoparticles. Environ Nanotechnol Monit Manage 20:100320
379. Karnan T, Selvakumar SAS (2016) Biosynthesis of ZnO nanoparticles using rambutan (*Nephelium lappaceum* L.) peel extract and their photocatalytic activity on methyl orange dye. J Mol Struct 1125:358–365
380. Rafique M, Shafiq F, Gillani SSA, Shakil M, Tahir MB, Sadaf I (2020) Eco-friendly green and biosynthesis of copper oxide nanoparticles using Citrofortunella microcarpa leaves extract for efficient photocatalytic degradation of Rhodamin B dye form textile wastewater. Optik 208:164053
381. Das P, Ghosh S, Ghosh R, Dam S, Baskey M (2018) Madhuca longifolia plant mediated green synthesis of cupric oxide nanoparticles: a promising environmentally sustainable material for waste water treatment and efficient antibacterial agent. J Photochem Photobiol B 189:66–73
382. Zhang H, Ruan Y, Feng Y, Su M, Diao Z, Chen D, Kong L (2019) Solvent-free hydrothermal synthesis of gamma-aluminum oxide nanoparticles with selective adsorption of Congo red. J Colloid Interface Sci 536:180–188
383. Liu X, He X, Zhang J, Yang J, Xiang X, Ma Z, Zong E (2020) Cerium oxide nanoparticle functionalized lignin as a nano-biosorbent for efficient phosphate removal. RSC Adv 10(3):1249–1260
384. Li M, Zhang B, Zou S, Liu Q, Yang M (2020) Highly selective adsorption of vanadium (V) by nano-hydrous zirconium oxide-modified anion exchange resin. J Hazard Mater 384:121386
385. Imran M, Khan ZUH, Iqbal J, Shah NS, Muzammil S, Ali S, Amjad M (2020) Potential of siltstone and its composites with biochar and magnetite nanoparticles for the removal of cadmium from contaminated aqueous solutions: batch and column scale studies. Environ Pollut 259:113938
386. Imran M, Khan ZUH, Iqbal MM, Iqbal J, Shah NS, Munawar S, Rizwan M (2020) Effect of biochar modified with magnetite nanoparticles and HNO3 for efficient removal of Cr (VI) from contaminated water: a batch and column scale study. Environ Pollut 261:114231
387. El-Dib FI, Mohamed DE, El-Shamy OA, Mishrif MR (2020) Study the adsorption properties of magnetite nanoparticles in the presence of different synthesized surfactants for heavy metal ions removal. Egypt J Pet 29(1):1–7
388. Guo W, Fu Z, Zhang Z, Wang H, Liu S, Feng W, Giesy JP (2020) Synthesis of Fe3O4 magnetic nanoparticles coated with cationic surfactants and their applications in Sb (V) removal from water. Sci Total Environ 710:136302
389. Bangari RS, Yadav VK, Singh JK, Sinha N (2020) Fe3O4-Functionalized boron nitride nanosheets as novel adsorbents for removal of arsenic (III) from contaminated water. ACS Omega 5(18):10301–10314
390. Singh V, Srivastava VC (2020) Self-engineered iron oxide nanoparticle incorporated on mesoporous biochar derived from textile mill sludge for the removal of an emerging pharmaceutical pollutant. Environ Pollut 259:113822
391. Xing M, Xie Q, Li X, Guan T, Wu D (2020) Monolayers of an organosilane on magnetite nanoparticles for the fast removal of Cr (VI) from water. Environ Technol 41(5):658–668

392. Ajmal Z, Usman M, Anastopoulos I, Qadeer A, Zhu R, Wakeel A, Dong R (2020) Use of nano-/micro-magnetite for abatement of cadmium and lead contamination. J Environ Manage 264:110477
393. Ren G, Wang X, Zheng B, Zhang Z, Yang L, Yang X (2020) Fabrication of Mg doped magnetite nanoparticles by recycling of titanium slag and their application of arsenate adsorption. J Clean Prod 252:119599
394. Kulal P, Badalamoole V (2020) Efficient removal of dyes and heavy metal ions from waste water using Gum ghatti–graft–poly (4-acryloylmorpholine) hydrogel incorporated with magnetite nanoparticles. J Environ Chem Eng 20:104207
395. Arabkhani P, Asfaram A (2020) Development of a novel three-dimensional magnetic polymer aerogel as an efficient adsorbent for malachite green removal. J Hazard Mater 384:121394
396. Kumar AKR, Saikia K, Neeraj G, Cabana H, Kumar VV (2020) Remediation of bio-refinery wastewater containing organic and inorganic toxic pollutants by adsorption onto chitosan-based magnetic nanosorbent. Water Qual Res J 55(1):36–51
397. Khan H, Khalil AK, Khan A (2019) Photocatalytic degradation of alizarin yellow in aqueous medium and real samples using chitosan conjugated tin magnetic nanocomposites. J Mater Sci Mater Electron 30(24):21332–21342
398. Roya M, Mostafa F, Mohammad J (2020) Synthesis of ZnO-magnetic/ZSM-5 and its application for removal of Disperse Blue 56 from contaminated water. Chem Eng Process Process Intensification 20:107969
399. Li Z, Liu Y, Zou S, Lu C, Bai H, Mu H, Duan J (2020) Removal and adsorption mechanism of tetracycline and cefotaxime contaminants in water by NiFe2O4-COF-chitosan-terephthalaldehyde nanocomposites film. Chem Eng J 382:123008
400. Chen T, Wang Q, Lyu J, Bai P, Guo X (2020) Boron removal and reclamation by magnetic magnetite (Fe3O4) nanoparticle: an adsorption and isotopic separation study. Sep Purif Technol 231:115930
401. Liyanage AS, Canaday S, Pittman CU Jr, Mlsna T (2020) Rapid remediation of pharmaceuticals from wastewater using magnetic Fe3O4/Douglas fir biochar adsorbents. Chemosphere 20:127336
402. Wang J, Zhang Q, Deng F, Luo X, Dionysiou DD (2020) Rapid toxicity elimination of organic pollutants by the photocatalysis of environment-friendly and magnetically recoverable step-scheme SnFe2O4/ZnFe2O4 nano-heterojunctions. Chem Eng J 379:122264
403. Raha S, Ahmaruzzaman M (2020) Enhanced performance of a novel superparamagnetic g-C3N4/NiO/ZnO/Fe3O4 nanohybrid photocatalyst for removal of Esomeprazole: effects of reaction parameters, co-existing substances and water matrices. Chem Eng J 20:124969
404. Pourzad A, Sobhi HR, Behbahani M, Esrafili A, Kalantary RR, Kermani M (2020) Efficient visible light-induced photocatalytic removal of paraquat using N-doped TiO2@ SiO2@ Fe3O4 nanocomposite. J Mol Liq 299:112167
405. Zhang C, Guo D, Shen T, Hou X, Zhu M, Liu S, Hu Q (2020) Titanium dioxide/magnetic metal-organic framework preparation for organic pollutants removal from water under visible light. Colloids Surf A 589:124484
406. Amin Marsooli M, Rahimi Nasrabadi M, Fasihi-Ramandi M, Adib K, Pourmasoud S, Ahmadi F, Plonska-Brzezinska ME (2020) Synthesis of magnetic Fe3O4/ZnWO4 and Fe3O4/ZnWO4/CeVO4 nanoparticles: the photocatalytic effects on organic pollutants upon irradiation with UV–Vis light. Catalysts 10(5):494
407. Ahmadpour N, Sayadi MH, Sobhani S, Hajiani M (2020) Photocatalytic degradation of model pharmaceutical pollutant by novel magnetic TiO2@ ZnFe2O4/Pd nanocomposite with enhanced photocatalytic activity and stability under solar light irradiation. J Environ Manage 271:110964
408. Khammar S, Bahramifar N, Younesi H (2020) Preparation and surface engineering of CM-β-CD functionalized Fe3O4@ TiO2 nanoparticles for photocatalytic degradation of polychlorinated biphenyls (PCBs) from transformer oil. J Hazard Mater 20:122422
409. Sayadi MH, Sobhani S, Hajiani M (2020) A potential natural solar light active photocatalyst using magnetic ZnFe2O4@ TiO2/Cu nanocomposite as a high performance and recyclable platform for degradation of naproxen from aqueous solution. J Clean Prod 20:122023
410. Villegas VAR, Ramírez JIDL, Guevara EH, Sicairos SP, Ayala LAH, Sanchez BL (2020) Synthesis and characterization of magnetite nanoparticles for photocatalysis of nitrobenzene. J Saudi Chem Soc 24(2):223–235
411. Baig MM, Zulfiqar S, Yousuf MA, Touqeer M, Ullah S, Agboola P, Shakir I (2020) Structural and photocatalytic properties of new rare earth La3+ substituted MnFe2O4 ferrite nanoparticles. Ceram Int 20:20

412. Kianfar AH, Arayesh MA (2020) Synthesis, characterization and investigation of photocatalytic and catalytic applications of Fe3O4/TiO2/CuO nanoparticles for degradation of MB and reduction of nitrophenols. J Environ Chem Eng 8(1):103640
413. Asgari E, Farzadkia M, Esrafili A, Badi MY, Jokandan SF, Sobhi HR (2020) Application of a photocatalytic ozonation process using TiO2 magnetic nanoparticles for the removal of Ceftazide from aqueous solutions: evaluation of performance, comparative study and mechanism. Optik 20:164667
414. Ammar SH, Elaibi AI, Mohammed IS (2020) Core/shell Fe3O4@ Al2O3-PMo magnetic nanocatalyst for photocatalytic degradation of organic pollutants in an internal loop airlift reactor. J Water Process Eng 37:101240
415. Hashemzadeh M, Nilchi A, Hassani AH (2019) Synthesis of novel surface-modified hematite nanoparticles for lead ions removal from aqueous solution. Mater Chem Phys 227:279–290
416. Dehbi A, Dehmani Y, Omari H, Lammini A, Elazhari K, Abdallaoui A (2020) Hematite iron oxide nanoparticles (α-Fe2O3): synthesis and modelling adsorption of malachite green. J Environ Chem Eng 8(1):103394
417. Jerin VM, Remya R, Thomas M, Varkey JT (2019) Investigation on the removal of toxic chromium ion from waste water using Fe2O3 nanoparticles. Mater Today Proc 9:27–31
418. Greenstein KE, Myung NV, Parkin GF, Cwiertny DM (2019) Performance comparison of hematite (α-Fe2O3)-polymer composite and core-shell nanofibers as point-of-use filtration platforms for metal sequestration. Water Res 148:492–503
419. Gunawardhana BPN, Gunathilake CA, Dayananda KEDYT, Dissanayake DMSN, Mantilaka MMMGPG, Kalpage CS, Weerasekara BGND (2020) Synthesis of hematite nanodiscs from natural laterites and investigating their adsorption capability of removing Ni2+ and Cd2+ ions from aqueous solutions. J Compos Sci 4(2):57
420. Abd El Aal SA, Abdelhady AM, Mansour NA, Hassan NM, Elbaz F, Elmaghraby EK (2019) Physical and chemical characteristics of hematite nanoparticles prepared using microwave-assisted synthesis and its application as adsorbent for Cu, Ni Co, Cd and Pb from aqueous solution. Mater Chem Phys 235:121771
421. Shen G, Pan L, Zhang R, Sun S, Hou F, Zhang X, Zou JJ (2020) Low-spin-state hematite with superior adsorption of anionic contaminations for water purification. Adv Mater 32(11):1905988
422. Hashemzadeh M, Nilchi A, Hassani AH, Saberi R (2019) Synthesis of novel surface-modified hematite nanoparticles for the removal of cobalt-60 radiocations from aqueous solution. Int J Environ Sci Technol 16(2):775–792
423. Abdelrahman EA, Hegazey RM, Kotp YH, Alharbi A (2019) Facile synthesis of Fe2O3 nanoparticles from Egyptian insecticide cans for efficient photocatalytic degradation of methylene blue and crystal violet dyes. Spectrochim Acta Part A Mol Biomol Spectrosc 222:117195
424. Liu Q, Tang J, Li X, Lin Q, Xiao R, Zhang M, Zhou Y (2020) Effect of lignosulfonate on the adsorption performance of hematite for Cd (II). Sci Total Environ 20:139952
425. Patra D, Gopalan B, Ganesan R (2019) Direct solid-state synthesis of maghemite as a magnetically recoverable adsorbent for the abatement of methylene blue. J Environ Chem Eng 7(5):103384
426. Devatha CP, Shivani S (2020) Novel application of maghemite nanoparticles coated bacteria for the removal of cadmium from aqueous solution. J Environ Manage 258:110038
427. Siddiqui SI, Singh PN, Tara N, Pal S, Chaudhry SA, Sinha I (2020) Arsenic removal from water by starch functionalized maghemite nano-adsorbents: thermodynamics and kinetics investigations. Colloid Interface Sci Commun 36:100263
428. Irawan C, Nata IF, Lee CK (2019) Removal of Pb (II) and As (V) using magnetic nanoparticles coated montmorillonite via one-pot solvothermal reaction as adsorbent. J Environ Chem Eng 7(2):103000
429. Campos AFC, de Oliveira HAL, da Silva FN, da Silva FG, Coppola P, Aquino R, Depeyrot J (2019) Core-shell bimagnetic nanoadsorbents for hexavalent chromium removal from aqueous solutions. J Hazard Mater 362:82–91
430. Pourmortazavi SM, Sahebi H, Zandavar H, Mirsadeghi S (2019) Fabrication of Fe3O4 nanoparticles coated by extracted shrimp peels chitosan as sustainable adsorbents for removal of chromium contaminates from wastewater: the design of experiment. Compos B Eng 175:107130
431. Areerachakul N, Sakulkhaemaruethai S, Johir MAH, Kandasamy J, Vigneswaran S (2019) Photocatalytic degradation of organic pollutants from wastewater using aluminium doped titanium dioxide. J Water Process Eng 27:177–184

432. Koohestani H (2019) Photocatalytic removal of cyanide and Cr (IV) from wastewater in the presence of each other by using TiO2/UV. Micro Nano Lett 14(1):45–50
433. Sirirerkratana K, Kemacheevakul P, Chuangchote S (2019) Color removal from wastewater by photocatalytic process using titanium dioxide-coated glass, ceramic tile, and stainless steel sheets. J Clean Prod 215:123–130
434. Marcelino RB, Amorim CC, Ratova M, Delfour-Peyrethon B, Kelly P (2019) Novel and versatile TiO2 thin films on PET for photocatalytic removal of contaminants of emerging concern from water. Chem Eng J 370:1251–1261
435. Tang H, Shang Q, Tang Y, Yi X, Wei Y, Yin K, Liu C (2020) Static and continuous flow photoelectrocatalytic treatment of antibiotic wastewater over mesh of TiO2 nanotubes implanted with g-C3N4 nanosheets. J Hazard Mater 384:121248
436. Prasad AR, Garvasis J, Oruvil SK, Joseph A (2019) Bio-inspired green synthesis of zinc oxide nanoparticles using Abelmoschus esculentus mucilage and selective degradation of cationic dye pollutants. J Phys Chem Solids 127:265–274
437. Khalafi T, Buazar F, Ghanemi K (2019) Phycosynthesis and enhanced photocatalytic activity of zinc oxide nanoparticles toward organosulfur pollutants. Sci Rep 9(1):1–10
438. Varadavenkatesan T, Lyubchik E, Pai S, Pugazhendhi A, Vinayagam R, Selvaraj R (2019) Photocatalytic degradation of Rhodamine B by zinc oxide nanoparticles synthesized using the leaf extract of *Cyanometra ramiflora*. J Photochem Photobiol, B 199:111621
439. Rasheed T, Nabeel F, Bilal M, Iqbal HM (2019) Biogenic synthesis and characterization of cobalt oxide nanoparticles for catalytic reduction of direct yellow-142 and methyl orange dyes. Biocatal Agric Biotechnol 19:101154
440. Mohanta J, Dey B, Dey S (2020) Magnetic cobalt oxide nanoparticles: sucrose-assisted self-sustained combustion synthesis, characterization, and efficient removal of malachite green from water. J Chem Eng Data 65(5):2819–2829
441. Parhizkar J, Habibi MH (2019) Investigation and comparison of cobalt ferrite composite nanoparticles with individual iron oxide and cobalt oxide nanoparticles in azo dyes removal. J Water Environ Nanotechnol 4(1):17–30
442. Reddy CV, Reddy IN, Ravindranadh K, Reddy KR, Shetti NP, Kim D, Aminabhavi TM (2020) Copper-doped ZrO2 nanoparticles as high-performance catalysts for efficient removal of toxic organic pollutants and stable solar water oxidation. J Environ Manage 260:110088
443. Singh J, Kumar V, Kim KH, Rawat M (2019) Biogenic synthesis of copper oxide nanoparticles using plant extract and its prodigious potential for photocatalytic degradation of dyes. Environ Res 177:108569
444. Rahdar S, Rahdar A, Igwegbe CA, Moghaddam F, Ahmadi S (2019) Synthesis and physical characterization of nickel oxide nanoparticles and its application study in the removal of ciprofloxacin from contaminated water by adsorption: equilibrium and kinetic studies. Desalin Water Treat 141:386–393
445. Ul Haq A, Saeed M, Usman M, Naqvi SAR, Bokhari TH, Maqbool T, Khalid H (2020) Sorption of chlorpyrifos onto zinc oxide nanoparticles impregnated Pea peels (*Pisum sativum* L.): equilibrium, kinetic and thermodynamic studies. Environ Technol Innov 17:100516
446. Moghaddas SMTH, Elahi B, Javanbakht V (2020) Biosynthesis of pure zinc oxide nanoparticles using Quince seed mucilage for photocatalytic dye degradation. J Alloy Compd 821:153519
447. Aziz A, Ali N, Khan A, Bilal M, Malik S, Ali N, Khan H (2020) Chitosan-zinc sulfide nanoparticles, characterization and their photocatalytic degradation efficiency for azo dyes. Int J Biol Macromol 20:20
448. Shah SJ, Khan A, Naz N, Ismail A, Zahid M, Khan MS, Zada A (2020) Synthesis of CoCrFeO4-chitosan beads sun-light-driven photocatalyst with well recycling for efficiently degrading high-concentration dyes. Spectrochim Acta Part A Mol Biomol Spectrosc 20:118314
449. Adeyemi JO, Onwudiwe DC (2020) SnS2 and SnO2 nanoparticles obtained from organotin (IV) dithiocarbamate complex and their photocatalytic activities on methylene blue. Materials 13(12):2766
450. Dileepkumar VG, Surya PS, Pratapkumar C, Viswanatha R, Ravikumar CR, Kumar MA, Thanh BX (2020) NaFeS2 as a new photocatalytic material for the degradation of industrial dyes. J Environ Chem Eng 20:104005
451. Kaviyarasu K, Magdalane CM, Jayakumar D, Samson Y, Bashir AKH, Maaza M, Kennedy J (2020) High performance of pyrochlore like Sm2Ti2O7 heterojunction photocatalyst for efficient

degradation of rhodamine-B dye with waste water under visible light irradiation. J King Saud Univ Sci 32(2):1516–1522
452. Yousefi R (2014) Metal-selenide nanostructures: growth and properties. Metal Chalcogenide Nanostruct Renew Energy Appl 20:43–81
453. Patil PD, Ghosh S, Wasala M, Lei S, Vajtai R, Ajayan PM, Talapatra S (2019) Gate-induced metal-insulator transition in 2D van der Waals layers of copper indium selenide based field-effect transistors. ACS Nano 13(11):13413–13420
454. Greco T, Ippen C, Wedel A (2017) U.S. Patent No. 9,698,311. Washington, DC: U.S. Patent and Trademark Office
455. Jin Z, Zhang M, Wang M, Feng C, Wang ZS (2017) Metal selenides as efficient counter electrodes for dye-sensitized solar cells. Acc Chem Res 50(4):895–904
456. Ashiq MN, Irshad S, Ehsan MF, Rehman S, Farooq S, Najam-Ul-Haq M, Zia A (2017) Visible-light active tin selenide nanostructures: synthesis, characterization and photocatalytic activity. New J Chem 41(23):14689–14695
457. Darroudi M, KhandaKhandan Nasab N, Salimizand H, Dehnad A (2019) Green synthesis and antibacterial activity of zinc selenide (ZnSe) nanoparticles. Nanomed J 6(4):258–262
458. Gong J, Hao Y, Li L, Xue S, Xie P, Hou X, Huang J (2019) The preparation and photocatalytic performance research of CdSe and wool ball-like GO/CdSe microspheres. J Alloy Compd 779:962–970
459. Shi W, Gao M, Wei J, Gao J, Fan C, Ashalley E, Wang Z (2018) Tin selenide (SnSe): growth, properties, and applications. Adv Sci 5(4):1700602
460. Mansimova SH, Mirzoeva RJ, Mashadiyeva LF, Babanly MB (2018) Thermodynamic properties of lead-antimony selenides. Appl Solid State Chem 4:104–111
461. Nica EM, Yu R, Si Q (2017) Orbital-selective pairing and superconductivity in iron selenides. NPJ Quantum Mater 2(1):1–7
462. Yang CT, Hsiang HI, Tu JH (2016) Copper selenide crystallites synthesized using the hot-injection process. Adv Powder Technol 27(3):959–963
463. Ghaedi M, Jah AH, Khodadoust S, Sahraei R, Daneshfar A, Mihandoost A, Purkait MK (2012) Cadmium telluride nanoparticles loaded on activated carbon as adsorbent for removal of sunset yellow. Spectrochim Acta Part A Mol Biomol Spectrosc 90:22–27
464. Ghaedi M, Amirabad SZ, Marahel F, Kokhdan SN, Sahraei R, Nosrati M, Daneshfar A (2011) Synthesis and characterization of Cadmium selenide nanoparticles loaded on activated carbon and its efficient application for removal of Muroxide from aqueous solution. Spectrochim Acta Part A Mol Biomol Spectrosc 83(1):46–51
465. Sharifpour E, Ghaedi M, Asfaram A, Farsadrooh M, Dil EA, Javadian H (2020) Modeling and optimization of ultrasound-assisted high performance adsorption of Basic Fuchsin by starch-capped zinc selenide nanoparticles/AC as a novel composite using response surface methodology. Int J Biol Macromol 152:913–921
466. Ali N, Uddin S, Khan A, Khan S, Khan S, Ali N, Bilal M (2020) Regenerable chitosan-bismuth cobalt selenide hybrid microspheres for mitigation of organic pollutants in an aqueous environment. Int J Biol Macromol 20:20
467. Altaf S, Ajaz H, Imran M, Ul-Hamid A, Naz M, Aqeel M, Ikram M (2020) Synthesis and characterization of binary selenides of transition metals to investigate its photocatalytic, antimicrobial and anticancer efficacy. Appl Nanosci 20:1–15
468. Ali N, Ahmad S, Khan A, Khan S, Bilal M, Din SU, Khan H (2020) Selenide-chitosan as high-performance nanophotocatalyst for accelerated degradation of pollutants. Chem Asian J 20:20
469. Ahmad W, Khan A, Ali N, Khan S, Uddin S, Malik S, Bilal M (2020) Photocatalytic degradation of crystal violet dye under sunlight by chitosan-encapsulated ternary metal selenide microspheres. Environ Sci Pollut Res 20:1–14
470. Yang J, Zhu W, Qu W, Yang Z, Wang J, Zhang M, Li H (2019) Selenium functionalized metal–organic framework MIL-101 for efficient and permanent sequestration of mercury. Environ Sci Technol 53(4):2260–2268
471. Yang J, Li Q, Zu H, Yang Z, Qu W, Li M, Li H (2020) Surface-engineered sponge decorated with copper selenide for highly efficient gas-phase mercury immobilization. Environ Sci Technol 54(24):16195–16203
472. Ghosh T, Cho KY, Ullah K, Nikam V, Park CY, Meng ZD, Oh WC (2013) High photonic effect of organic dye degradation by CdSe–graphene–TiO2 particles. J Ind Eng Chem 19(3):797–805

473. Yang Z, Li H, Yang Q, Qu W, Zhao J, Feng Y, Shih K (2020) Development of selenized magnetite (Fe3O4-xSey) as an efficient and recyclable trap for elemental mercury sequestration from coal combustion flue gas. Chem Eng J 2:125022
474. Wang S, Yang J, Yang Z, Zhu W, Li H, Song J, Guo X (2019) Nanosized copper selenide for mercury removal from indoor air and emergency disposal of liquid mercury leakage. Ind Eng Chem Res 58(47):21881–21889
475. Yang Z, Li H, Yang J, Feng S, Liu X, Zhao J, Shih K (2019) Nanosized copper selenide functionalized zeolitic imidazolate framework-8 (CuSe/ZIF-8) for efficient immobilization of gas-phase elemental mercury. Adv Func Mater 29(17):1807191
476. Yang J, Li Q, Li M, Zhu W, Yang Z, Qu W, Li H (2020) In situ decoration of selenide on copper foam for the efficient immobilization of gaseous elemental mercury. Environ Sci Technol 54(3):2022–2030
477. Yang Z, Li H, Yang J, Yang Q, Zhao J, Yang J, Shih K (2019) Amorphous molybdenum selenide nanosheet as an efficient trap for the permanent sequestration of vapor-phase elemental mercury. Adv Sci 6(20):1901410
478. Yang Z, Li H, Yang Q, Zhao J, Meng F, Feng Y, Shih K (2020) Amorphous molybdenum selenide intercalated magnetite as a recyclable trap for the effective sequestration of elemental mercury. J Mater Chem A 20:25
479. Li H, Zu H, Yang Z, Yang J, Xu H, Qu W (2021) The adsorption mechanisms of Hg0 on marcasite-type metal selenides: the influences of metal-terminated site. Chem Eng J 406:126723
480. Liu W, Xu H, Guo Y, Yuan Y, Liao Y, Qu Z, Yan N (2019) Immobilization of elemental mercury in non-ferrous metal smelting gas using ZnSe1− xSx nanoparticles. Fuel 254:115641
481. Yang Q, Yang Z, Li H, Zhao J, Yang J, Qu W, Shih K (2020) Selenide functionalized natural mineral sulfides as efficient sorbents for elemental mercury capture from coal combustion flue gas. Chem Eng J 20:125611
482. Wang J, Wang X, Zhao G, Song G, Chen D, Chen H, Wang X (2018) Polyvinylpyrrolidone and polyacrylamide intercalated molybdenum disulfide as adsorbents for enhanced removal of chromium (VI) from aqueous solutions. Chem Eng J 334:569–578
483. Yang X, Wu R, Liu H, Fan H, Zhang H, Sun Y (2018) Amorphous molybdenum selenide as highly efficient photocatalyst for the photodegradation of organic dyes under visible light. Appl Surf Sci 457:214–220
484. Yang S, Shao C, Zhou X, Li X, Tao R, Li X, Liu Y (2020) MoSe2/TiO2 nanofibers for cycling photocatalytic removing water pollutants under UV–Vis–NIR light. ACS Appl Nano Mater 3(3):2278–2287
485. Mkhalid IA (2016) Visible light photocatalytic degradation of 2-chlorophenol in wastewater using copper selenide nanorods. Nanosci Nanotechnol Lett 8(9):744–749
486. Sonia S, Kumar PS, Mangalaraj D, Ponpandian N, Viswanathan C (2013) Influence of growth and photocatalytic properties of copper selenide (CuSe) nanoparticles using reflux condensation method. Appl Surf Sci 283:802–807
487. Lai CH, Lu MY, Chen LJ (2012) Metal sulfide nanostructures: synthesis, properties and applications in energy conversion and storage. J Mater Chem 22(1):19–30
488. Jones CJ, Chattopadhyay S, Gonzalez-Pech NI, Avendano C, Hwang N, Lee SS, Yavuz C (2015) A novel, reactive green iron sulfide (sulfide green rust) formed on iron oxide nanocrystals. Chem Mater 27(3):700–707
489. Gurumoorthy G, Rani PJ, Thirumaran S, Ciattini S (2017) Cobalt (III) dithiocarbamates for anion sensing and preparation of cobalt sulfide and cobalt-iron sulfide nanoparticles: photocatalytic degradation of dyes with as-prepared nanoparticles. Inorg Chim Acta 455:132–139
490. Bagheri AR, Ghaedi M, Asfaram A, Hajati S, Ghaedi AM, Bazrafshan A, Rahimi MR (2016) Modeling and optimization of simultaneous removal of ternary dyes onto copper sulfide nanoparticles loaded on activated carbon using second-derivative spectrophotometry. J Taiwan Inst Chem Eng 65:212–224
491. Aazam ES (2014) Photocatalytic oxidation of methylene blue dye under visible light by Ni doped Ag2S nanoparticles. J Ind Eng Chem 20(6):4033–4038
492. Asfaram A, Ghaedi M, Hajati S, Goudarzi A, Bazrafshan AA (2015) Simultaneous ultrasound-assisted ternary adsorption of dyes onto copper-doped zinc sulfide nanoparticles loaded on activated carbon: optimization by response surface methodology. Spectrochim Acta Part A Mol Biomol Spectrosc 145:203–212

493. Yue L, Wu Y, Liu X, Xin B, Chen S (2014) Controllable extracellular biosynthesis of bismuth sulfide nanostructure by sulfate-reducing bacteria in water–oil two-phase system. Biotechnol Prog 30(4):960–966
494. Wang S, Yang B, Liu Y (2017) Synthesis of a hierarchical SnS2 nanostructure for efficient adsorption of Rhodamine B dye. J Colloid Interface Sci 507:225–233
495. Mishra S, Singh AK, Singh JK (2020) Ferrous sulfide and carboxyl-functionalized ferroferric oxide incorporated PVDF-based nanocomposite membranes for simultaneous removal of highly toxic heavy-metal ions from industrial ground water. J Membr Sci 593:117422
496. Sun M, Cheng G, Ge X, Chen M, Wang C, Lou L, Xu X (2018) Aqueous Hg (II) immobilization by chitosan stabilized magnetic iron sulfide nanoparticles. Sci Total Environ 621:1074–1083
497. Yu Y, Yang Q, Ma J, Sun W, Yin C, Li X, Lu Z (2018) Construction of strontium titanate/binary metal sulfide heterojunction photocatalysts for enhanced visible-light-driven photocatalytic activity. NANO 13(11):1850130
498. Kalpana K, Selvaraj V (2016) Development of ZnS/SnS/A-FA nanorods at ambient temperature: binary catalyst for the removal of congo red dye and pathogenic bacteria from wastewater. J Ind Eng Chem 41:105–113
499. Zhu B, Cheng H, Qin Y, Ma J, Kong Y, Komarneni S (2020) Copper sulfide as an excellent co-catalyst with K2S2O8 for dye decomposition in advanced oxidation process. Sep Purif Technol 233:116057
500. Enesca A, Isac L, Duta A (2015) Charge carriers injection in tandem semiconductors for dyes mineralization. Appl Catal B 162:352–363
501. Duta A, Enesca A, Bogatu C, Gyorgy E (2016) Solar-active photocatalytic tandems. A compromise in the photocatalytic processes design. Mater Sci Semicond Process 42:94–97
502. Andronic L, Isac L, Duta A (2011) Photochemical synthesis of copper sulphide/titanium oxide photocatalyst. J Photochem Photobiol A 221(1):30–37
503. Gao L, Du J, Ma T (2017) Cysteine-assisted synthesis of CuS-TiO2 composites with enhanced photocatalytic activity. Ceram Int 43(12):9559–9563
504. Kao YT, Yang SM, Lu KC (2019) Synthesis and photocatalytic properties of CuO-CuS core-shell nanowires. Materials 12(7):1106
505. Basu M, Garg N, Ganguli AK (2014) A type-II semiconductor (ZnO/CuS heterostructure) for visible light photocatalysis. J Mater Chem A 2(20):7517–7525
506. Mahanthappa M, Kottam N, Yellappa S (2019) Enhanced photocatalytic degradation of methylene blue dye using CuSCdS nanocomposite under visible light irradiation. Appl Surf Sci 475:828–838
507. Wang Y, Zhang L, Jiu H, Li N, Sun Y (2014) Depositing of CuS nanocrystals upon the graphene scaffold and their photocatalytic activities. Appl Surf Sci 303:54–60
508. Chen X, Li H, Wu Y, Wu H, Wu L, Tan P, Xiong X (2016) Facile fabrication of novel porous graphitic carbon nitride/copper sulfide nanocomposites with enhanced visible light driven photocatalytic performance. J Colloid Interface Sci 476:132–143
509. Borthakur P, Boruah PK, Darabdhara G, Sengupta P, Das MR, Boronin AI, Fedorov VE (2016) Microwave assisted synthesis of CuS-reduced graphene oxide nanocomposite with efficient photocatalytic activity towards azo dye degradation. J Environ Chem Eng 4(4):4600–4611
510. Li J, Sun L, Yan Y, Zhu Z (2016) A novel fabrication of Cu2O@ Cu7S4 core-shell micro/nanocrystals from Cu2O temples and enhanced photocatalytic activities. Mater Res Bull 80:200–208
511. He HY (2016) Facile synthesis of ultrafine CuS nanocrystalline/TiO2: Fe nanotubes hybrids and their photocatalytic and Fenton-like photocatalytic activities in the dye degradation. Microporous Mesoporous Mater 227:31–38
512. Varghese J, Varghese KT (2015) Graphene/CuS/ZnO hybrid nanocomposites for high performance photocatalytic applications. Mater Chem Phys 167:258–264
513. Meng N, Zhou Y, Nie W, Song L, Chen P (2015) CuS/MoS 2 nanocomposite with high solar photocatalytic activity. J Nanopart Res 17(7):300
514. Thuy UTD, Liem NQ, Parlett CM, Lalev GM, Wilson K (2014) Synthesis of CuS and CuS/ZnS core/shell nanocrystals for photocatalytic degradation of dyes under visible light. Catal Commun 44:62–67
515. Maleki M, Haghighi M (2016) Sono-dispersion of CuS-CdS over TiO2 in one-pot hydrothermal reactor as visible-light-driven nanostructured photocatalyst. J Mol Catal A Chem 424:283–296

516. Khan A, Alam U, Raza W, Bahnemann D, Muneer M (2018) One-pot, self-assembled hydrothermal synthesis of 3D flower-like CuS/g-C3N4 composite with enhanced photocatalytic activity under visible-light irradiation. J Phys Chem Solids 115:59–68
517. Tavker N, Sharma M (2020) Designing of waste fruit peels extracted cellulose supported molybdenum sulfide nanostructures for photocatalytic degradation of RhB dye and industrial effluent. J Environ Manage 255:109906
518. Wang J, Zhang R, Huo Y, Ai Y, Gu P, Wang X, Wang X (2019) Efficient elimination of Cr (VI) from aqueous solutions using sodium dodecyl sulfate intercalated molybdenum disulfide. Ecotoxicol Environ Saf 175:251–262
519. Du Y, Wang J, Zou Y, Yao W, Hou J, Xia L, Wang X (2017) Synthesis of molybdenum disulfide/reduced graphene oxide composites for effective removal of Pb (II) from aqueous solutions. Sci Bull 62(13):913–922
520. Zhang Y, Niu J, Xu J (2020) Fe (II)-promoted activation of peroxymonosulfate by molybdenum disulfide for effective degradation of acetaminophen. Chem Eng J 381:122718
521. Zhu H, Tan X, Tan L, Chen C, Alharbi NS, Hayat T, Wang X (2018) Biochar derived from sawdust embedded with molybdenum disulfide for highly selective removal of Pb2+. ACS Appl Nano Mater 1(6):2689–2698
522. Wang M, Peng Z, Qian J, Li H, Zhao Z, Fu X (2018) Highly efficient solar-driven photocatalytic degradation on environmental pollutants over a novel C fibers@ MoSe2 nanoplates core-shell composite. J Hazard Mater 347:403–411
523. Fu F, Dionysiou DD, Liu H (2014) The use of zero-valent iron for groundwater remediation and wastewater treatment: a review. J Hazard Mater 267:194–205
524. Shi LN, Zhang X, Chen ZL (2011) Removal of chromium (VI) from wastewater using bentonite-supported nanoscale zero-valent iron. Water Res 45(2):886–892
525. Ali HSM, Khan SA (2020) Stabilization of various zero-valent metal nanoparticles on a superabsorbent polymer for the removal of dyes, nitrophenol, and pathogenic bacteria. ACS Omega 5(13):7379–7391
526. Devi TA, Ananthi N, Amaladhas TP (2016) Photobiological synthesis of noble metal nanoparticles using Hydrocotyle asiatica and application as catalyst for the photodegradation of cationic dyes. J Nanostruct Chem 6(1):75–92
527. Lee YC, Kim JY, Shin HJ (2013) Removal of malachite green (MG) from aqueous solutions by adsorption, precipitation, and alkaline fading using talc. Sep Sci Technol 48(7):1093–1101
528. Han TH, Khan MM, Kalathil S, Lee J, Cho MH (2013) Simultaneous enhancement of methylene blue degradation and power generation in a microbial fuel cell by gold nanoparticles. Ind Eng Chem Res 52(24):8174–8181
529. Sarina S, Waclawik ER, Zhu H (2013) Photocatalysis on supported gold and silver nanoparticles under ultraviolet and visible light irradiation. Green Chem 15(7):1814–1833
530. Liu Y, Yu H, Zhan S, Li Y, Lv Z, Yang X, Yu Y (2011) Fast degradation of methylene blue with electrospun hierarchical α-Fe 2 O 3 nanostructured fibers. J Sol-Gel Sci Technol 58(3):716
531. Shojaei S, Shojaei S, Sasani M (2017) The efficiency of eliminating Direct Red 81 by Zero-valent Iron nanoparticles from aqueous solutions using response surface Model (RSM). Model Earth Syst Environ 3(1):27
532. Lin Z, Weng X, Owens G, Chen Z (2020) Simultaneous removal of Pb (II) and rifampicin from wastewater by iron nanoparticles synthesized by a tea extract. J Clean Prod 242:118476
533. Nidheesh PV, Khatri J, Singh TA, Gandhimathi R, Ramesh ST (2018) Review of zero-valent aluminium based water and wastewater treatment methods. Chemosphere 200:621–631
534. Lin KYA, Lin CH (2016) Simultaneous reductive and adsorptive removal of bromate from water using acid-washed zero-valent aluminum (ZVAl). Chem Eng J 297:19–25
535. Fu F, Cheng Z, Dionysiou DD, Tang B (2015) Fe/Al bimetallic particles for the fast and highly efficient removal of Cr (VI) over a wide pH range: performance and mechanism. J Hazard Mater 298:261–269
536. Pouretedal HR, Shafeie A, Keshavarz MH (2012) Preparation, characterization and catalytic activity of tin dioxide and zero-valent tin nanoparticles. J Korean Chem Soc 56:4
537. Huang YH, Tang C, Zeng H (2012) Removing molybdate from water using a hybridized zero-valent iron/magnetite/Fe (II) treatment system. Chem Eng J 200:257–263
538. Lian JJ, Yang M, Wang HL, Zhong Y, Chen B, Huang WL, Peng PA (2020) Enhanced molybdenum (VI) removal using sulfide-modified nanoscale zerovalent iron: kinetics and influencing factors. Water Sci Technol 20:20

539. Pourrezaei P, Alpatova A, Khosravi K, Drzewicz P, Chen Y, Chelme-Ayala P, El-Din MG (2014) Removal of organic compounds and trace metals from oil sands process-affected water using zero valent iron enhanced by petroleum coke. J Environ Manage 139:50–58
540. Zhu H, Huang Q, Fu S, Zhang X, Shi M, Liu B (2020) Removal of molybdenum (VI) from raw water using nano zero-valent iron supported on activated carbon. Water 12(11):3162
541. Fang Z, Chen J, Qiu X, Qiu X, Cheng W, Zhu L (2011) Effective removal of antibiotic metronidazole from water by nanoscale zero-valent iron particles. Desalination 268(1–3):60–67
542. Ambashta RD, Repo E, Sillanpää M (2011) Degradation of tributyl phosphate using nanopowders of iron and iron–nickel under the influence of a static magnetic field. Ind Eng Chem Res 50(21):11771–11777
543. Klimkova S, Cernik M, Lacinova L, Filip J, Jancik D, Zboril R (2011) Zero-valent iron nanoparticles in treatment of acid mine water from in situ uranium leaching. Chemosphere 82(8):1178–1184
544. Yu S, Wang X, Liu Y, Chen Z, Wu Y, Liu Y, Wang X (2019) Efficient removal of uranium (VI) by layered double hydroxides supported nanoscale zero-valent iron: a combined experimental and spectroscopic studies. Chem Eng J 365:51–59
545. Vollprecht D, Krois LM, Sedlazeck KP, Müller P, Mischitz R, Olbrich T, Pomberger R (2019) Removal of critical metals from waste water by zero-valent iron. J Clean Prod 208:1409–1420
546. Crane RA, Dickinson M, Scott TB (2015) Nanoscale zero-valent iron particles for the remediation of plutonium and uranium contaminated solutions. Chem Eng J 262:319–325
547. Cao Y, Zhang S, Zhong Q, Wang G, Xu X, Li T, Li Y (2018) Feasibility of nanoscale zero-valent iron to enhance the removal efficiencies of heavy metals from polluted soils by organic acids. Ecotoxicol Environ Saf 162:464–473
548. Zhang W, Qian L, Ouyang D, Chen Y, Han L, Chen M (2019) Effective removal of Cr (VI) by attapulgite-supported nanoscale zero-valent iron from aqueous solution: enhanced adsorption and crystallization. Chemosphere 221:683–692
549. Üzüm Ç, Shahwan T, Eroğlu AE, Lieberwirth I, Scott TB, Hallam KR (2008) Application of zero-valent iron nanoparticles for the removal of aqueous Co2+ ions under various experimental conditions. Chem Eng J 144(2):213–220
550. Wu B, Peng D, Hou S, Tang B, Wang C, Xu H (2018) Dynamic study of Cr (VI) removal performance and mechanism from water using multilayer material coated nanoscale zerovalent iron. Environ Pollut 240:717–724
551. Liu J, Ou C, Han W, Shen J, Bi H, Sun X, Wang L (2015) Selective removal of nitroaromatic compounds from wastewater in an integrated zero valent iron (ZVI) reduction and ZVI/H 2 O 2 oxidation process. RSC Adv 5(71):57444–57452
552. Dong G, Ai Z, Zhang L (2014) Total aerobic destruction of azo contaminants with nanoscale zero-valent copper at neutral pH: promotion effect of in-situ generated carbon center radicals. Water Res 66:22–30
553. Wen G, Wang SJ, Ma J, Huang TL, Liu ZQ, Zhao L, Xu JL (2014) Oxidative degradation of organic pollutants in aqueous solution using zero valent copper under aerobic atmosphere condition. J Hazard Mater 275:193–199
554. Chi H, He X, Zhang J, Ma J (2019) Efficient degradation of refractory organic contaminants by zero-valent copper/hydroxylamine/peroxymonosulfate process. Chemosphere 237:124431
555. Zhang J, Guo J, Wu Y, Lan Y, Li Y (2017) Efficient activation of ozone by zero-valent copper for the degradation of aniline in aqueous solution. J Taiwan Inst Chem Eng 81:335–342
556. Marcelo CR, Puiatti GA, Nascimento MA, Oliveira AF, Lopes RP (2018) Degradation of the Reactive Blue 4 dye in aqueous solution using zero-valent copper nanoparticles. J Nanomater 20:18
557. Zhang C, Xuan L, Zhang J, Yuan F, Kong X, Qin C (2020) Degradation of organic contaminants through the activation of oxygen using zero valent copper coupled with sodium tripolyphosphate under neutral conditions. J Environ Sci 90:375–384
558. Liu W, Zhang H, Cao B, Lin K, Gan J (2011) Oxidative removal of bisphenol A using zero valent aluminum–acid system. Water Res 45(4):1872–1878
559. Yang Y, Gai WZ, Zhou JG, Deng ZY (2020) Surface modified zero-valent aluminum for Cr (VI) removal at neutral pH. Chem Eng J 125:140
560. Oualha MA, Omri N, Oualha R, Nouioui MA, Abderrabba M, Amdouni N, Laoutid F (2019) Development of metal hydroxide nanoparticles from eggshell waste and seawater and their application as flame retardants for ethylene-vinyl acetate copolymer (EVA). Int J Biol Macromol 128:994–1001

561. Choi SJ, Choy JH (2011) Layered double hydroxide nanoparticles as target-specific delivery carriers: uptake mechanism and toxicity. Nanomedicine 6(5):803–814
562. Ahmed EM, Aggor FS, Awad AM, El-Aref AT (2013) An innovative method for preparation of nanometal hydroxide superabsorbent hydrogel. Carbohyd Polym 91(2):693–698
563. Nie M, Deng Y, Nie S, Yan C, Ding M, Dong W, Zhang Y (2019) Simultaneous removal of bisphenol A and phosphate from water by peroxymonosulfate combined with calcium hydroxide. Chem Eng J 369:35–45
564. Lee SY, Choi JW, Song KG, Choi K, Lee YJ, Jung KW (2019) Adsorption and mechanistic study for phosphate removal by rice husk-derived biochar functionalized with Mg/Al-calcined layered double hydroxides via co-pyrolysis. Compos B Eng 176:107209
565. Koilraj P, Kalusulingam R, Sasaki K (2019) Arginine and lysine-functionalized layered double hydroxides as efficient sorbents for radioactive Co2+ removal by chelate-facilitated immobilization. Chem Eng J 374:359–369
566. Sadeghalvad B, Azadmehr A, Hezarkhani A (2019) A new approach to improve sulfate uptake from contaminated aqueous solution: metal layered double hydroxides functionalized metasomatic rock. Sep Sci Technol 54(4):447–466
567. Xie Y, Yuan X, Wu Z, Zeng G, Jiang L, Peng X, Li H (2019) Adsorption behavior and mechanism of Mg/Fe layered double hydroxide with Fe3O4-carbon spheres on the removal of Pb (II) and Cu (II). J Colloid Interface Sci 536:440–455
568. Zhang K, Dwivedi V, Chi C, Wu J (2010) Graphene oxide/ferric hydroxide composites for efficient arsenate removal from drinking water. J Hazard Mater 182(1–3):162–168
569. Hu YB, Li XY (2018) Influence of a thin aluminum hydroxide coating layer on the suspension stability and reductive reactivity of nanoscale zero-valent iron. Appl Catal B 226:554–564
570. Saitoh T, Yamaguchi M, Hiraide M (2011) Surfactant-coated aluminum hydroxide for the rapid removal and biodegradation of hydrophobic organic pollutants in water. Water Res 45(4):1879–1889
571. Kamaraj R, Davidson DJ, Sozhan G, Vasudevan S (2015) Adsorption of herbicide 2-(2, 4-dichlorophenoxy) propanoic acid by electrochemically generated aluminum hydroxides: an alternative to chemical dosing. RSC Adv 5(50):39799–39809
572. Hu H, Yang L, Lin Z, Zhao Y, Jiang X, Hou L (2018) A low-cost and environment friendly chitosan/aluminum hydroxide bead adsorbent for fluoride removal from aqueous solutions. Iran Polym J 27(4):253–261
573. Mulugeta E, Zewge F, Annette Johnson C, Chandravanshi BS (2014) A high-capacity aluminum hydroxide-based adsorbent for water defluoridation. Desalin Water Treat 52(28–30):5422–5429
574. Choong CE, Ibrahim S, Basirun WJ (2019) Mesoporous silica from batik sludge impregnated with aluminum hydroxide for the removal of bisphenol A and ibuprofen. J Colloid Interface Sci 541:12–17
575. Wang X, Zhang B, Ma J, Ning P (2020) Novel synthesis of aluminum hydroxide gel-coated nano zero-valent iron and studies of its activity in flocculation-enhanced removal of tetracycline. J Environ Sci 89:194–205
576. Liu J, Zhang H, Yao Z, Li X, Tang J (2019) Thermal desorption of PCBs contaminated soil with calcium hydroxide in a rotary kiln. Chemosphere 220:1041–1046
577. Dal Pozzo A, Moricone R, Antonioni G, Tugnoli A, Cozzani V (2018) Hydrogen chloride removal from flue gas by low-temperature reaction with calcium hydroxide. Energy Fuels 32(1):747–756
578. Chaudhary M, Maiti A (2019) Defluoridation by highly efficient calcium hydroxide nanorods from synthetic and industrial wastewater. Colloids Surf A 561:79–88
579. Choi YK, Jang HM, Kan E, Wallace AR, Sun W (2019) Adsorption of phosphate in water on a novel calcium hydroxide-coated dairy manure-derived biochar. Environ Eng Res 24(3):434–442
580. Xu F, Chen J, Yang G, Ji X, Wang Q, Liu S, Ni Y (2019) Combined treatments consisting of calcium hydroxide and activate carbon for purification of xylo-oligosaccharides of pre-hydrolysis liquor. Polymers 11(10):1558
581. Wang K, Zhao J, Li H, Zhang X, Shi H (2016) Removal of cadmium (II) from aqueous solution by granular activated carbon supported magnesium hydroxide. J Taiwan Inst Chem Eng 61:287–291

582. El Bouraie M, Masoud AA (2017) Adsorption of phosphate ions from aqueous solution by modified bentonite with magnesium hydroxide Mg (OH) 2. Appl Clay Sci 140:157–164
583. Tsuchiya K, Fuchida S, Tokoro C (2020) Experimental study and surface complexation modeling of fluoride removal by magnesium hydroxide in adsorption and coprecipitation processes. J Environ Chem Eng 8(6):104514
584. Bologo V, Maree JP, Carlsson F (2012) Application of magnesium hydroxide and barium hydroxide for the removal of metals and sulphate from mine water. Water SA 38(1):23–28
585. Hu YB, Zhang M, Li XY (2019) Improved longevity of nanoscale zero-valent iron with a magnesium hydroxide coating shell for the removal of Cr (VI) in sand columns. Environ Int 133:105249
586. Zhang Y, Guo X, Wu F, Yao Y, Yuan Y, Bi X, Amine K (2016) Mesocarbon microbead carbon-supported magnesium hydroxide nanoparticles: turning spent Li-ion battery anode into a highly efficient phosphate adsorbent for wastewater treatment. ACS Appl Mater Interfaces 8(33):21315–21325
587. Dong W, Sun D, Li Y, Wu T (2018) Rapid removal and recovery of emulsified oil from ASP produced water using in situ formed magnesium hydroxide. Environ Sci Water Res Technol 4(4):539–548
588. Ponomarev N, Pastushok O, Repo E, Doshi B, Sillanpää M (2019) Lignin-based magnesium hydroxide nanocomposite. Synthesis and application for the removal of potentially toxic metals from aqueous solution. ACS Appl Nano Mater 2(9):5492–5503
589. Raicopol MD, Andronescu C, Voicu SI, Vasile E, Pandele AM (2019) Cellulose acetate/layered double hydroxide adsorptive membranes for efficient removal of pharmaceutical environmental contaminants. Carbohyd Polym 214:204–212
590. Eivazzadeh-Keihan R, Chenab KK, Taheri-Ledari R, Mosafer J, Hashemi SM, Mokhtarzadeh A, Hamblin MR (2020) Recent advances in the application of mesoporous silica-based nanomaterials for bone tissue engineering. Mater Sci Eng C 107:110267
591. Su X, Wu Q, Li J, Xiao X, Lott A, Lu W, Wu J (2014) Silicon-based nanomaterials for lithium-ion batteries: a review. Adv Energy Mater 4(1):1300882
592. Araghi SH, Entezari MH (2015) Amino-functionalized silica magnetite nanoparticles for the simultaneous removal of pollutants from aqueous solution. Appl Surf Sci 333:68–77
593. Mahmudi M, Shadjou N, Hasanzadeh FAM (2019) Synthesis and adsorption behavior of dendritic Fibrous Nano-silica (DFNS) grafted by d-penicillamine as an advanced nanomaterial for the removal of some metal ions from contaminated water. J Electroanal Chem 848:113272
594. Wang P, Du M, Zhu H, Bao S, Yang T, Zou M (2015) Structure regulation of silica nanotubes and their adsorption behaviors for heavy metal ions: pH effect, kinetics, isotherms and mechanism. J Hazard Mater 286:533–544
595. Salmani MH, Ehrampoush MH, Eslami H, Eftekhar B (2020) Synthesis, characterization and application of mesoporous silica in removal of cobalt ions from contaminated water. Groundw Sustain Dev 20:100425
596. Bhattarai B, Muruganandham M, Suri RP (2014) Development of high efficiency silica coated β-cyclodextrin polymeric adsorbent for the removal of emerging contaminants of concern from water. J Hazard Mater 273:146–154
597. Chen D, Li Y, Bao M, Hou Y, Jin J, Yin Z, Wang Z (2019) Magnet-responsive silica microrods as solid stabilizer and adsorbent for simultaneous removal of coexisting contaminants in water. ACS Sustain Chem Eng 7(16):13786–13795
598. Fan J, Li D, Teng W, Yang J, Liu Y, Liu L, Zhao D (2016) Ordered mesoporous silica/polyvinylidene fluoride composite membranes for effective removal of water contaminants. J Mater Chem A 4(10):3850–3857
599. Shim J, Lim JM, Shea PJ, Oh BT (2014) Simultaneous removal of phenol, Cu and Cd from water with corn cob silica-alginate beads. J Hazard Mater 272:129–136
600. Nanda B, Pradhan AC, Parida KM (2017) Fabrication of mesoporous CuO/ZrO2-MCM-41 nanocomposites for photocatalytic reduction of Cr (VI). Chem Eng J 316:1122–1135
601. Zhang Z, Lan H, Liu H, Li H, Qu J (2015) Iron-incorporated mesoporous silica for enhanced adsorption of tetracycline in aqueous solution. RSC Adv 5(53):42407–42413
602. Nairi V, Medda L, Monduzzi M, Salis A (2017) Adsorption and release of ampicillin antibiotic from ordered mesoporous silica. J Colloid Interface Sci 497:217–225

603. Siddiqa A, Shahid A, Gill R (2015) Silica decorated CNTs sponge for selective removal of toxic contaminants and oil spills from water. J Environ Chem Eng 3(2):892–897
604. Tiwari D, Lee SM (2017) Chitosan templated synthesis of mesoporous silica and its application in the treatment of aqueous solutions contaminated with cadmium (II) and lead (II). Chem Eng J 328:434–444
605. Yang W, Ding P, Zhou L, Yu J, Chen X, Jiao F (2013) Preparation of diamine modified mesoporous silica on multi-walled carbon nanotubes for the adsorption of heavy metals in aqueous solution. Appl Surf Sci 282:38–45
606. Van den Bergh M, Krajnc A, Voorspoels S, Tavares SR, Mullens S, Beurroies I, De Vos D (2020) Highly selective removal of perfluorinated contaminants by adsorption on all-silica zeolite Beta. Angew Chem 20:20
607. Glocheux Y, Albadarin AB, Galán J, Oyedoh E, Mangwandi C, Gerente C, Walker GM (2014) Adsorption study using optimised 3D organised mesoporous silica coated with Fe and Al oxides for specific As (III) and As (V) removal from contaminated synthetic groundwater. Microporous Mesoporous Mater 198:101–114
608. Ge J, Wang X, Li C, Wang S, Wang L, Qu R, Wang Z (2019) Photodegradation of polychlorinated diphenyl sulfides mediated by reactive oxygen species on silica gel. Chem Eng J 359:1056–1064
609. Dinker MK, Kulkarni PS (2015) Temperature based adsorption studies of Cr (vi) using p-toluidine formaldehyde resin coated silica material. New J Chem 39(5):3687–3697
610. Abukhadra MR, Shaban M (2019) Recycling of different solid wastes in synthesis of high-order mesoporous silica as adsorbent for safranin dye. Int J Environ Sci Technol 16(11):7573–7582
611. Wang Y, Hu R, Lin G, Roy I, Yong KT (2013) Functionalized quantum dots for biosensing and bioimaging and concerns on toxicity. ACS Appl Mater Interfaces 5(8):2786–2799
612. Kryuchkyan GY, Shahnazaryan V, Kibis OV, Shelykh IA (2017) Resonance fluorescence from an asymmetric quantum dot dressed by a bichromatic electromagnetic field. Phys Rev A 95(1):013834
613. Tuncer Degim I, Kadioglu D (2013) Cheap, suitable, predictable and manageable nanoparticles for drug delivery: quantum dots. Curr Drug Deliv 10(1):32–38
614. Wang C, Grillot F, Even J (2012) Impacts of wetting layer and excited state on the modulation response of quantum-dot lasers. IEEE J Quantum Electron 48(9):1144–1150
615. Ghosh D, Sarkar K, Devi P, Kim KH, Kumar P (2021) Current and future perspectives of carbon and graphene quantum dots: from synthesis to strategy for building optoelectronic and energy devices. Renew Sustain Energy Rev 135:110391
616. Paszkiewicz-Gawron M, Kowalska E, Endo-Kimura M, Zwara J, Pancielejko A, Wang K, Grabowska-Musiał E (2021) Stannates, titanates and tantalates modified with carbon and graphene quantum dots for enhancement of visible-light photocatalytic activity. Appl Surf Sci 541:148425
617. Kaur M, Mehta SK, Kansal SK (2017) Nitrogen doped graphene quantum dots: efficient fluorescent chemosensor for the selective and sensitive detection of 2, 4, 6-trinitrophenol. Sens Actuators B Chem 245:938–945
618. Atienzar P, Primo A, Lavorato C, Molinari R, García H (2013) Preparation of graphene quantum dots from pyrolyzed alginate. Langmuir 29(20):6141–6146
619. Rong M, Lin L, Song X, Zhao T, Zhong Y, Yan J, Chen X (2015) A label-free fluorescence sensing approach for selective and sensitive detection of 2, 4, 6-trinitrophenol (TNP) in aqueous solution using graphitic carbon nitride nanosheets. Anal Chem 87(2):1288–1296
620. Lin L, Rong M, Lu S, Song X, Zhong Y, Yan J, Chen X (2015) A facile synthesis of highly luminescent nitrogen-doped graphene quantum dots for the detection of 2, 4, 6-trinitrophenol in aqueous solution. Nanoscale 7(5):1872–1878
621. Qu A, Xie H, Xu X, Zhang Y, Wen S, Cui Y (2016) High quantum yield graphene quantum dots decorated TiO2 nanotubes for enhancing photocatalytic activity. Appl Surf Sci 375:230–241
622. Yu X, Liu J, Yu Y, Zuo S, Li B (2014) Preparation and visible light photocatalytic activity of carbon quantum dots/TiO2 nanosheet composites. Carbon 68:718–724
623. Ming H, Ma Z, Liu Y, Pan K, Yu H, Wang F, Kang Z (2012) Large scale electrochemical synthesis of high quality carbon nanodots and their photocatalytic property. Dalton Trans 41(31):9526–9531
624. Tian L, Li Z, Wang P, Zhai X, Wang X, Li T (2021) Carbon quantum dots for advanced electrocatalysis. J Energy Chem 55:279–294

625. Du XY, Wang CF, Wu G, Chen S (2021) The rapid and large-scale production of carbon quantum dots and their integration with polymers. Angew Chem Int Ed 60(16):8585–8595
626. Saud PS, Pant B, Alam AM, Ghouri ZK, Park M, Kim HY (2015) Carbon quantum dots anchored TiO2 nanofibers: effective photocatalyst for waste water treatment. Ceram Int 41(9):11953–11959
627. Niu WJ, Li Y, Zhu RH, Shan D, Fan YR, Zhang XJ (2015) Ethylenediamine-assisted hydrothermal synthesis of nitrogen-doped carbon quantum dots as fluorescent probes for sensitive biosensing and bioimaging. Sens Actuators B Chem 218:229–236
628. Muthulingam S, Lee IH, Uthirakumar P (2015) Highly efficient degradation of dyes by carbon quantum dots/N-doped zinc oxide (CQD/N-ZnO) photocatalyst and its compatibility on three different commercial dyes under daylight. J Colloid Interface Sci 455:101–109
629. Yu H, Zhang H, Huang H, Liu Y, Li H, Ming H, Kang Z (2012) ZnO/carbon quantum dots nanocomposites: one-step fabrication and superior photocatalytic ability for toxic gas degradation under visible light at room temperature. New J Chem 36(4):1031–1035
630. Safajou H, Khojasteh H, Salavati-Niasari M, Mortazavi-Derazkola S (2017) Enhanced photocatalytic degradation of dyes over graphene/Pd/TiO2 nanocomposites: TiO2 nanowires versus TiO2 nanoparticles. J Colloid Interface Sci 498:423–432
631. Lutz T, MacLachlan A, Sudlow A, Nelson J, Hill MS, Molloy KC, Haque SA (2012) Thermal decomposition of solution processable metal xanthates on mesoporous titanium dioxide films: a new route to quantum-dot sensitized heterojunctions. Phys Chem Chem Phys 14(47):16192–16196
632. Gnanasekaran L, Hemamalini R, Ravichandran K (2015) Synthesis and characterization of TiO2 quantum dots for photocatalytic application. J Saudi Chem Soc 19(5):589–594
633. Javed S, Islam M, Mujahid M (2019) Synthesis and characterization of TiO2 quantum dots by sol gel reflux condensation method. Ceram Int 45(2):2676–2679
634. Saravanan R, Gupta VK, Narayanan V, Stephen A (2013) Comparative study on photocatalytic activity of ZnO prepared by different methods. J Mol Liq 181:133–141
635. Kaur A, Salunke DB, Umar A, Mehta SK, Sinha ASK, Kansal SK (2017) Visible light driven photocatalytic degradation of fluoroquinolone levofloxacin drug using Ag 2 O/TiO 2 quantum dots: a mechanistic study and degradation pathway. New J Chem 41(20):12079–12090
636. Sood S, Kumar S, Umar A, Kaur A, Mehta SK, Kansal SK (2015) TiO2 quantum dots for the photocatalytic degradation of indigo carmine dye. J Alloy Compd 650:193–198
637. Rajabi HR, Arjmand H, Kazemdehdashti H, Farsi M (2016) A comparison investigation on photocatalytic activity performance and adsorption efficiency for the removal of cationic dye: quantum dots vs magnetic nanoparticles. J Environ Chem Eng 4(3):2830–2840
638. Shamsipur M, Rajabi HR (2014) Study of photocatalytic activity of ZnS quantum dots as efficient nanoparticles for removal of methyl violet: effect of ferric ion doping. Spectrochim Acta Part A Mol Biomol Spectrosc 122:260–267
639. Kumar A, Kumari A, Sharma G, Du B, Naushad M, Stadler FJ (2020) Carbon quantum dots and reduced graphene oxide modified self-assembled S@ C3N4/B@ C3N4 metal-free nano-photocatalyst for high performance degradation of chloramphenicol. J Mol Liq 300:112356
640. Phophayu S, Pimpang P, Wongrerkdee S, Sujinnapram S, Wongrerkdee S (2020) Modified graphene quantum dots-zinc oxide nanocomposites for photocatalytic degradation of organic dyes and commercial herbicide. J Reinf Plast Compos 39(3–4):81–94
641. Liu H, Liang J, Fu S, Li L, Cui J, Gao P, Zhou J (2020) N doped carbon quantum dots modified defect-rich g-C3N4 for enhanced photocatalytic combined pollutions degradation and hydrogen evolution. Colloids Surf A 591:124552
642. Wang W, Zeng Z, Zeng G, Zhang C, Xiao R, Zhou C, Huang D (2019) Sulfur doped carbon quantum dots loaded hollow tubular g-C3N4 as novel photocatalyst for destruction of *Escherichia coli* and tetracycline degradation under visible light. Chem Eng J 378:122132
643. Zhang M, Lai C, Li B, Huang D, Zeng G, Xu P, Li M (2019) Rational design 2D/2D BiOBr/CDs/g-C3N4 Z-scheme heterojunction photocatalyst with carbon dots as solid-state electron mediators for enhanced visible and NIR photocatalytic activity: kinetics, intermediates, and mechanism insight. J Catal 369:469–481
644. Wang F, Chen P, Feng Y, Xie Z, Liu Y, Su Y, Liu G (2017) Facile synthesis of N-doped carbon dots/g-C3N4 photocatalyst with enhanced visible-light photocatalytic activity for the degradation of indomethacin. Appl Catal B 207:103–113

645. Shao DD, Yang WJ, Xiao HF, Wang ZY, Zhou C, Cao XL, Sun SP (2019) Self-cleaning nanofiltration membranes by coordinated regulation of carbon quantum dots and polydopamine. ACS Appl Mater Interfaces 12(1):580–590
646. Yuan A, Lei H, Xi F, Liu J, Qin L, Chen Z, Dong X (2019) Graphene quantum dots decorated graphitic carbon nitride nanorods for photocatalytic removal of antibiotics. J Colloid Interface Sci 548:56–65
647. Liang H, Tai X, Du Z, Yin Y (2020) Enhanced photocatalytic activity of ZnO sensitized by carbon quantum dots and application in phenol wastewater. Opt Mater 100:109674
648. Yousaf MU, Pervaiz E, Minallah S, Afzal MJ, Honghong L, Yang M (2019) Tin oxide quantum dots decorated graphitic carbon nitride for enhanced removal of organic components from water: green process. Results Phys 14:102455
649. Wang S, Li L, Zhu Z, Zhao M, Zhang L, Zhang N, Li G (2019) Remarkable improvement in photocatalytic performance for tannery wastewater processing via snS2 modified with N-doped carbon quantum dots: synthesis, characterization, and 4-nitrophenol-aided Cr (VI) photoreduction. Small 15(29):1804515
650. Yu J, Zhang J, Zeng T, Wang H, Sun Y, Chen L, Shi H (2019) Stable incorporation of MnOx quantum dots into N-doped hollow carbon: a synergistic peroxymonosulfate activator for enhanced removal of bisphenol A. Sep Purif Technol 213:264–275
651. Han W, Li D, Zhang M, Ximin H, Duan X, Liu S, Wang S (2020) Photocatalytic activation of peroxymonosulfate by surface-tailored carbon quantum dots. J Hazard Mater 20:122695
652. Xu L, Bai X, Guo L, Yang S, Jin P, Yang L (2019) Facial fabrication of carbon quantum dots (CDs)-modified N-TiO2-x nanocomposite for the efficient photoreduction of Cr (VI) under visible light. Chem Eng J 357:473–486
653. El-Shamy AG, Zayied HSS (2020) New polyvinyl alcohol/carbon quantum dots (PVA/CQDs) nanocomposite films: structural, optical and catalysis properties. Synth Met 259:116218
654. Seng RX, Tan LL, Lee WC, Ong WJ, Chai SP (2020) Nitrogen-doped carbon quantum dots-decorated 2D graphitic carbon nitride as a promising photocatalyst for environmental remediation: a study on the importance of hybridization approach. J Environ Manage 255:109936
655. Riaz R, Ali M, Sahito IA, Arbab AA, Maiyalagan T, Anjum AS, Jeong SH (2019) Self-assembled nitrogen-doped graphene quantum dots (N-GQDs) over graphene sheets for superb electrophotocatalytic activity. Appl Surf Sci 480:1035–1046
656. Sharma S, Mehta SK, Ibhadon AO, Kansal SK (2019) Fabrication of novel carbon quantum dots modified bismuth oxide (α-Bi2O3/C-dots): material properties and catalytic applications. J Colloid Interface Sci 533:227–237
657. Koe WS, Chong WC, Pang YL, Koo CH, Ebrahim M, Mohammad AW (2020) Novel nitrogen and sulphur co-doped carbon quantum dots/titanium oxide photocatalytic membrane for in-situ degradation and removal of pharmaceutical compound. J Water Process Eng 33:101068
658. Zhao C, Liao Z, Liu W, Liu F, Ye J, Liang J, Li Y (2020) Carbon quantum dots modified tubular g-C3N4 with enhanced photocatalytic activity for carbamazepine elimination: mechanisms, degradation pathway and DFT calculation. J Hazard Mater 381:120957
659. Das GS, Shim JP, Bhatnagar A, Tripathi KM, Kim T (2019) Biomass-derived carbon quantum dots for visible-light-induced photocatalysis and label-free detection of fe (iii) and ascorbic acid. Sci Rep 9(1):1–9
660. Mohanta D, Ahmaruzzaman M (2020) Biogenic synthesis of SnO2 quantum dots encapsulated carbon nanoflakes: an efficient integrated photocatalytic adsorbent for the removal of bisphenol A from aqueous solution. J Alloy Compd 828:154093
661. Parthibavarman M, Sathishkumar S, Jayashree M, BoopathiRaja R (2019) Microwave assisted synthesis of pure and Ag doped SnO 2 quantum dots as novel platform for high photocatalytic activity performance. J Cluster Sci 30(2):351–363
662. Chu L, Duo F, Zhang M, Wu Z, Sun Y, Wang C, Sun J (2020) Doping induced enhanced photocatalytic performance of SnO2: Bi3+ quantum dots toward organic pollutants. Colloids Surf A 589:124416
663. Babu B, Koutavarapu R, Shim J, Yoo K (2020) SnO2 quantum dots decorated NiFe2O4 nanoplates: 0D/2D heterojunction for enhanced visible-light-driven photocatalysis. Mater Sci Semicond Process 107:104834

664. Zhang Y, Zhao Y, Xu Z, Su H, Bian X, Zhang S, Li L (2020) Carbon quantum dots implanted CdS nanosheets: efficient visible-light-driven photocatalytic reduction of Cr (VI) under saline conditions. Appl Catal B 262:118306
665. Bathula B, Koutavarapu R, Shim J, Yoo K (2020) Facile one-pot synthesis of gold/tin oxide quantum dots for visible light catalytic degradation of methylene blue: optimization of plasmonic effect. J Alloy Compd 812:152081
666. Hasija V, Sudhaik A, Raizada P, Hosseini-Bandegharaei A, Singh P (2019) Carbon quantum dots supported AgI/ZnO/phosphorus doped graphitic carbon nitride as Z-scheme photocatalyst for efficient photodegradation of 2, 4-dinitrophenol. J Environ Chem Eng 7(4):103272
667. Huang W, Wang S, Zhou Q, Liu X, Chen X, Yang K, Li D (2019) Constructing novel ternary composites of carbon quantum dots/Bi2MoO6/graphitic nanofibers with tunable band structure and boosted photocatalytic activity. Sep Purif Technol 217:195–205
668. Yang J, Liang Y, Li K, Yang G, Yin S (2019) One-step low-temperature synthesis of 0D CeO2 quantum dots/2D BiOX (X= Cl, Br) nanoplates heterojunctions for highly boosting photo-oxidation and reduction ability. Appl Catal B 250:17–30
669. Duan Z, Deng L, Shi Z, Zhang H, Zeng H, Crittenden J (2019) In situ growth of Ag-SnO2 quantum dots on silver phosphate for photocatalytic degradation of carbamazepine: performance, mechanism and intermediates toxicity assessment. J Colloid Interface Sci 534:270–278
670. Ahmadi Z, Ramezani H, Azizi SN, Chaichi MJ (2020) Synthesis of zeolite NaY supported Mn-doped ZnS quantum dots and investigation of their photodegradation ability towards organic dyes. Environ Sci Pollut Res 20:1–11
671. Jlassi K, Eid K, Sliem MH, Abdullah AM, Chehimi MM, Krupa I (2020) Rational synthesis, characterization, and application of environmentally friendly (polymer–carbon dot) hybrid composite film for fast and efficient UV-assisted Cd 2+ removal from water. Environ Sci Eur 32(1):1–13
672. Pan D, Jiao J, Li Z, Guo Y, Feng C, Liu Y, Wu M (2015) Efficient separation of electron–hole pairs in graphene quantum dots by TiO2 heterojunctions for dye degradation. ACS Sustain Chem Eng 3(10):2405–2413
673. Wang L, Li Y, Li S, Wang Y, Kong W, Xue W, Li C (2017) Synthesis, characterization and photocatalytic activity of graphene quantum dots-Ag solar driven photocatalyst. J Mater Sci Mater Electron 28(23):17570–17577
674. Bu X, Yang S, Bu Y, He P, Yang Y, Wang G, Yang J (2018) Highly active black TiO2/N-doped graphene quantum dots nanocomposites for sunlight driven photocatalytic sewage treatment. ChemistrySelect 3(1):201–206
675. Yan M, Zhu F, Gu W, Sun L, Shi W, Hua Y (2016) Construction of nitrogen-doped graphene quantum dots-BiVO 4/gC 3 N 4 Z-scheme photocatalyst and enhanced photocatalytic degradation of antibiotics under visible light. RSC Adv 6(66):61162–61174
676. Jiang XH, Wang LC, Yu F, Nie YC, Xing QJ, Liu X, Dai WL (2018) Photodegradation of organic pollutants coupled with simultaneous photocatalytic evolution of hydrogen using quantum-dot-modified g-C3N4 catalysts under visible-light irradiation. ACS Sustain Chem Eng 6(10):12695–12705
677. Guo Z, Wu H, Li M, Tang T, Wen J, Li X (2020) Phosphorus-doped graphene quantum dots loaded on TiO2 for enhanced photodegradation. Appl Surf Sci 20:146724
678. Dejpasand MT, Saievar-Iranizad E, Bayat A, Montaghemi A, Ardekani SR (2020) Tuning HOMO and LUMO of three region (UV, Vis and IR) photoluminescent nitrogen doped graphene quantum dots for photodegradation of methylene blue. Mater Res Bull 20:110886
679. Huang S, Li L, Zhu N, Lou Z, Liu W, Cheng J, Wang H (2020) Removal and recovery of chloride ions in concentrated leachate by Bi (III) containing oxides quantum dots/two-dimensional flakes. J Hazard Mater 382:121041
680. Chen Q, Chen L, Qi J, Tong Y, Lv Y, Xu C, Liu W (2019) Photocatalytic degradation of amoxicillin by carbon quantum dots modified K2Ti6O13 nanotubes: effect of light wavelength. Chin Chem Lett 30(6):1214–1218
681. Bhati A, Anand SR, Saini D, Sonkar SK (2019) Sunlight-induced photoreduction of Cr (VI) to Cr (III) in wastewater by nitrogen-phosphorus-doped carbon dots. NPJ Clean Water 2(1):1–9
682. Zhang J, Zhang X, Dong S, Zhou X, Dong S (2016) N-doped carbon quantum dots/TiO2 hybrid composites with enhanced visible light driven photocatalytic activity toward dye wastewater degradation and mechanism insight. J Photochem Photobiol A 325:104–110

683. Rajabi HR, Farsi M (2015) Effect of transition metal ion doping on the photocatalytic activity of ZnS quantum dots: synthesis, characterization, and application for dye decolorization. J Mol Catal A Chem 399:53–61
684. Fakhri A, Azad M, Tahami S (2017) Degradation of toxin via ultraviolet and sunlight photocatalysis using ZnO quantum dots/CuO nanosheets composites: preparation and characterization studies. J Mater Sci Mater Electron 28(21):16397–16402
685. Liu L, Hui J, Su L, Lv J, Wu Y, Irvine JT (2014) Uniformly dispersed CdS/CdSe quantum dots co-sensitized TiO2 nanotube arrays with high photocatalytic property under visible light. Mater Lett 132:231–235
686. Harish S, Sabarinathan M, Kristy AP, Archana J, Navaneethan M, Ikeda H, Hayakawa Y (2017) ZnS quantum dots impregnated-mesoporous TiO 2 nanospheres for enhanced visible light induced photocatalytic application. RSC Adv 7(42):26446–26457
687. Baslak C, Arslan G, Kus M, Cengeloglu Y (2016) Removal of Rhodamine B from water by using CdTeSe quantum dot-cellulose membrane composites. RSC Adv 6(22):18549–18557
688. Gupta BK, Kedawat G, Agrawal Y, Kumar P, Dwivedi J, Dhawan SK (2015) A novel strategy to enhance ultraviolet light driven photocatalysis from graphene quantum dots infilled TiO 2 nanotube arrays. RSC Adv 5(14):10623–10631
689. Sajjadi S, Khataee A, Kamali M (2017) Sonocatalytic degradation of methylene blue by a novel graphene quantum dots anchored CdSe nanocatalyst. Ultrason Sonochem 39:676–685
690. Agarwal S, Sadeghi N, Tyagi I, Gupta VK, Fakhri A (2016) Adsorption of toxic carbamate pesticide oxamyl from liquid phase by newly synthesized and characterized graphene quantum dots nanomaterials. J Colloid Interface Sci 478:430–438
691. Khojasteh H, Salavati-Niasari M, Safajou H, Safardoust-Hojaghan H (2017) Facile reduction of graphene using urea in solid phase and surface modification by N-doped graphene quantum dots for adsorption of organic dyes. Diam Relat Mater 79:133–144
692. Sricharoen P, Limchoowong N, Areerob Y, Nuengmatcha P, Techawongstien S, Chanthai S (2017) Fe3O4/hydroxyapatite/graphene quantum dots as a novel nano-sorbent for preconcentration of copper residue in Thai food ingredients: optimization of ultrasound-assisted magnetic solid phase extraction. Ultrason Sonochem 37:83–93
693. Zhang M, Yao Q, Lu C, Li Z, Wang W (2014) Layered double hydroxide–carbon dot composite: high-performance adsorbent for removal of anionic organic dye. ACS Appl Mater Interfaces 6(22):20225–20233
694. Mahmoud ME, Fekry NA, Abdelfattah AM (2020) Removal of uranium (VI) from water by the action of microwave-rapid green synthesized carbon quantum dots from starch-water system and supported onto polymeric matrix. J Hazard Mater 20:122770
695. Pirhaji JZ, Moeinpour F, Dehabadi AM, Ardakani SAY (2020) Synthesis and characterization of halloysite/graphene quantum dots magnetic nanocomposite as a new adsorbent for Pb (II) removal from water. J Mol Liq 300:112345
696. Sarkar N, Sahoo G, Swain SK (2020) Graphene quantum dot decorated magnetic graphene oxide filled polyvinyl alcohol hybrid hydrogel for removal of dye pollutants. J Mol Liq 302:112591
697. Far HS, Hasanzadeh M, Nashtaei MS, Rabbani M, Haji A, Hadavi Moghadam B (2020) PPI-dendrimer-functionalized magnetic metal-organic framework (Fe3O4@ MOF@ PPI) with high adsorption capacity for sustainable wastewater treatment. ACS Appl Mater Interfaces 12(22):25294–25303
698. Guo F, Aryana S, Han Y, Jiao Y (2018) A review of the synthesis and applications of polymer–nanoclay composites. Appl Sci 8(9):1696
699. Mishra AK (ed) (2017) Sol-gel based nanoceramic materials: preparation, properties and applications. Springer, Johannesburg, pp 1–297
700. Perego C, Bagatin R, Tagliabue M, Vignola R (2013) Zeolites and related mesoporous materials for multi-talented environmental solutions. Microporous Mesoporous Mater 166:37–49
701. Sohail I, Bhatti IA, Ashar A, Sarim FM, Mohsin M, Naveed R, Nazir A (2020) Polyamidoamine (PAMAM) dendrimers synthesis, characterization and adsorptive removal of nickel ions from aqueous solution. J Market Res 9(1):498–506

702. Hayati B, Arami M, Maleki A, Pajootan E (2015) Thermodynamic properties of dye removal from colored textile wastewater by poly (propylene imine) dendrimer. Desalin Water Treat 56(1):97–106
703. Almasri DA, Rhadfi T, Atieh MA, McKay G, Ahzi S (2018) High performance hydroxyiron modified montmorillonite nanoclay adsorbent for arsenite removal. Chem Eng J 335:1–12
704. Nikkhah AA, Zilouei H, Asadinezhad A, Keshavarz A (2015) Removal of oil from water using polyurethane foam modified with nanoclay. Chem Eng J 262:278–285
705. Narwade VN, Khairnar RS, Kokol V (2017) In-situ synthesised hydroxyapatite-loaded films based on cellulose nanofibrils for phenol removal from wastewater. Cellulose 24(11):4911–4925
706. Önnby L, Giorgi C, Plieva FM, Mattiasson B (2010) Removal of heavy metals from water effluents using supermacroporous metal chelating cryogels. Biotechnol Prog 26(5):1295–1302
707. Khan A, Badshah S, Airoldi C (2011) Dithiocarbamated chitosan as a potent biopolymer for toxic cation remediation. Colloids Surf B 87(1):88–95
708. Repo E, Warchoł JK, Bhatnagar A, Mudhoo A, Sillanpää M (2013) Aminopolycarboxylic acid functionalized adsorbents for heavy metals removal from water. Water Res 47(14):4812–4832
709. Lafi R, Montasser I, Hafiane A (2019) Adsorption of Congo red dye from aqueous solutions by prepared activated carbon with oxygen-containing functional groups and its regeneration. Adsorp Sci Technol 37(1–2):160–181
710. Sekulic MT, Boskovic N, Slavkovic A, Garunovic J, Kolakovic S, Pap S (2019) Surface functionalised adsorbent for emerging pharmaceutical removal: adsorption performance and mechanisms. Process Saf Environ Prot 125:50–63
711. Kecili R, Hussain CM (2018) Mechanism of adsorption on nanomaterials. Nanomaterials in chromatography. Elsevier, New York, pp 89–115
712. Bushra R, Ahmed A, Shahadat M (2016) Mechanism of adsorption on nanomaterials. In: Advanced environmental analysis, pp 90–111
713. Singh H, Javadpour F (2016) Langmuir slip-Langmuir sorption permeability model of shale. Fuel 164:28–37
714. Balarak D, Mostafapour FK, Azarpira H, Joghataei A (2017) Langmuir, Freundlich, Temkin and Dubinin–radushkevich isotherms studies of equilibrium sorption of ampicilin unto montmorillonite nanoparticles. J Pharm Res Int 20:1–9
715. Araújo CS, Almeida IL, Rezende HC, Marcionilio SM, Léon JJ, de Matos TN (2018) Elucidation of mechanism involved in adsorption of Pb (II) onto lobeira fruit (*Solanum lycocarpum*) using Langmuir, Freundlich and Temkin isotherms. Microchem J 137:348–354
716. Agarwal AK, Kadu MS, Pandhurnekar CP, Muthreja IL (2016) Brunauer–Emmett–Teller (BET), Langmuir and Freundlich isotherm studies for the adsorption of nickel ions onto coal fly ash. Asian J Water Environ Pollut 13(2):49–53
717. Vilela PB, Matias CA, Dalalibera A, Becegato VA, Paulino AT (2019) Polyacrylic acid-based and chitosan-based hydrogels for adsorption of cadmium: equilibrium isotherm, kinetic and thermodynamic studies. J Environ Chem Eng 7(5):103327
718. Zhuge Z, Liu X, Chen T, Gong Y, Li C, Niu L, Yamauchi Y (2021) Highly efficient photocatalytic degradation of different hazardous contaminants by CaIn2S4-Ti3C2Tx Schottky heterojunction: an experimental and mechanism study. Chem Eng J 421:127838
719. Wang Z, Jiang L, Wang K, Li Y, Zhang G (2021) Novel AgI/BiSbO4 heterojunction for efficient photocatalytic degradation of organic pollutants under visible light: interfacial electron transfer pathway, DFT calculation and degradation mechanism study. J Hazard Mater 410:124948
720. Li S, Shan S, Chen S, Hanbing L, Li Z, Liang Y, Li J (2021) Photocatalytic degradation of hazardous organic pollutants in water by Fe-MOFs and their composites: a review. J Environ Chem Eng 20:105967
721. Singh S, Khare N (2017) Coupling of piezoelectric, semiconducting and photoexcitation properties in NaNbO3 nanostructures for controlling electrical transport: realizing an efficient piezo-photoanode and piezo-photocatalyst. Nano Energy 38:335–341
722. Zhu B, Xia P, Li Y, Ho W, Yu J (2017) Fabrication and photocatalytic activity enhanced mechanism of direct Z-scheme g-C3N4/Ag2WO4 photocatalyst. Appl Surf Sci 391:175–183

## Authors and Affiliations

**Shizhong Zhang[1] · Sumeet Malik[1,2] · Nisar Ali[1] · Adnan Khan[2] · Mohammad Bilal[3] · Kashif Rasool[4]**

[1] Key Laboratory for Palygorskite Science and Applied Technology of Jiangsu Province, National and Local Joint Engineering Research Center for Mineral Salt Deep Utilization, Huaiyin Institute of Technology, Huai'an 223003, China

[2] Institute of Chemical Sciences, University of Peshawar, Khyber Pakhtunkhwa 25120, Pakistan

[3] School of Life Science and Food Engineering, Huaiyin Institute of Technology, Huai'an 223003, China

[4] Qatar Environment and Energy Research Institute, Hamad Bin Khalifa University (HBKU), Qatar Foundation, P.O. Box 5824, Doha, Qatar